ELECTRO-THERMAL DESIGN AND OPTIMIZATION OF HIGH-SPECIFIC-POWER
SLOTLESS PM MACHINE FOR AIRCRAFT APPLICATIONS

BY

XUAN YI

DISSERTATION

Submitted in partial fulfillment of the requirements
for the degree of Doctor of Philosophy in Electrical and Computer Engineering
in the Graduate College of the
University of Illinois at Urbana-Champaign, 2020

Urbana, Illinois

Doctoral Committee:

Associate Professor Kiruba S. Haran, Chair
Professor Philip T. Krein
Professor Andrew Alleyne
Assistant Professor Arijit Banerjee

ABSTRACT

A 1 MW high-frequency air-core permanent-magnet (PM) motor, with power density over 13 kW/kg (8 hp/lb) and efficiency over 96%, is proposed for NASA hybrid-electric aircraft application. In order to maximize power density of the proposed motor topology, a large-scale multi-physics optimization, which is not favorable for current electrical machine software, is needed to obtain the best design candidates, which is not favorable for current electrical machine software. Therefore, developing electromagnetic (EM) and thermal analytical methods with computational efficiency and satisfactory accuracy is a key enabling factor for future multi-physics optimization of motor power density.

This dissertation summarizes the efforts of developing an electro-thermal analysis and optimization scheme of the proposed motor for aircraft applications. Component hardware tests including windage loss, fan performance, full-scale stator temperature and litz-wire were conducted to validate the proposed prediction methods and provide calibrations in the motor design analysis. Furthermore, slotless litz wire winding geometry and strand size are optimized with the developed electro-thermal modeling including transposition effects. After gaining confidence in the developed electro-thermal models, an optimization design toolbox is built for the hybrid-electric engine systems study. The first application study is in partnership with Rolls Royce's Electrically Variable Engine Project to study thermal management system integration effects on motor sizing. The second study is in collaboration with Raytheon Technologies to study motor transient performance with phase change materials integration, which can be tailored to a hybrid-electric engine mission profile.

To all my loved ones

ACKNOWLEDGMENTS

First of all, I would like to express my deep gratitude to my adviser, Prof. Kiruba S. Haran, who accepted me to join Illinois and helped me thrive here. He is the coolest boss who leads many exciting technical projects, such as the electric airplane (which is my favorite), and gives graduate students full patience, encouragement, and support. His depth of knowledge, practical mindset, and insightful guidance have inspired and motivated me to become a successful engineer. I must also thank my doctoral committee members, Professors Krein, Alleyne, and Banerjee, for their valuable time and feedback.

In addition, I would like to thank my colleagues and friends in the Power and Energy Systems and Power Optimization of Electro-Thermal Systems research groups. All the inspirational talks, collaborative relationships, and numerous nights in the lab motivate and help me move forward in this challenging journey.

Finally, I would like to express my great gratitude to the Power Optimization of Electro-Thermal Systems Research Center the Grainger Center for Electric Machinery and Electromechanics (CEME), and the National Aeronautics and Space Administration (NASA) for their financial support.

TABLE OF CONTENTS

LIST OF TABLES

LIST OF FIGURES

x

CHAPTER 1

INTRODUCTION

1.1 Motivation

High-performance electric drives are an important emerging technology within the aerospace industry, specifically in the push toward hybrid electric, all electric, and distributed propulsion aircraft architectures. One way to significantly reduce the weight of electric drives with emerging power electronics and cooling technologies is by pushing the fundamental frequency of synchronous machines substantially higher than is currently done. This is analogous to the recent trend of increasing switching frequency to reduce the size and weight of the passive components in power converters. Applying the technique in the motor itself does introduce new challenges for the electro-mechanical architecture, thermal management, frequency-based losses etc. In order not to dilute potential benefits with strategies to mitigate these challenges, a truly multi-physics co-design approach is required. This dissertation aims to develop electro-thermal analysis, design and optimization schemes of a high-specific-power MW motor for aircraft applications.

1.2 MW High-Specific-Power Motor

A 1 MW high-speed high-frequency air-core permanent magnet motor design was introduced for hybrid-electric aircraft electrification [1]. It is intended to operate at over 13 kW/kg specific power and 96% efficiency. The motor key specifications are listed in Table 1.1. In order to achieve high specific power, there are main two design paths in parallel. The first design path is to adopt a novel motor topology to develop a lightweight machine. The proposed motor uses an outer-rotor high-frequency high-pole-count Halbach-array permanent magnet
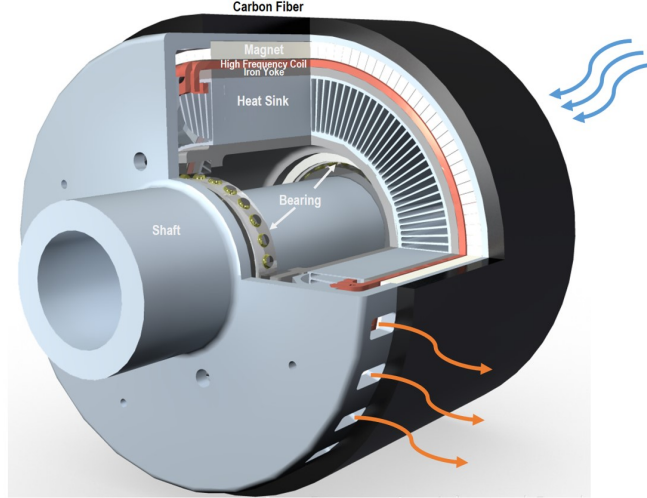
Figure 1.1: The Proposed Motor Design

Table 1.1: Motor Key Specs

Parameter	Value
Rated Power	1 MW
Rated Efficiency	96.40%
Rated Speed	15,000 rpm
Specific Power	13 kW/kg
Electrical Frequency	2,500 Hz
Copper Current Density	18.6 A/mm^2
Gap Flux Density	0.95 T
Insulation Class	H (180 °C)
Tip Speed	265 m/s
Cooling, forced air	20 m/s

topology, as shown in Figure 1.1. This motor concept can minimize the iron usage by eliminating the back yoke on the rotor and teeth region, and cut the stator back yoke depth with high pole count. Also, carbon fiber and other high-strength lightweight materials are adopted to ensure the integrity of the mechanical structure.

The second design path is to maximize the power with the given motor volume and topology. It is known that motor power is determined by magnetic loading, electric loading and speed according to the motor design governing equation. Then, the motor specific power can be optimized by maximizing the product of these three key design factors within feasible physical constraints.

Table 1.2: Summary of Current Density Range of Different Cooling Methods [2], [3]

Method	Description	Max J A/mm^2
forced air	forced air through radial/axial ducts by fan	5–12
indirect water	water pumped into cooling jacket around stator frame/yoke	10–15
indirect oil	oil or lubricant circulation for cooling on stator frame/yoke	10–15
liquid bathed	whole machine bathed in dielectric liquids such as mineral oils	up to 25
direct liquid	coolant in direct contact with conductors to take heat away	up to 30

The magnetic loading, also known as air gap flux density, is set at 0.95 T in the proposed motor. This value is constrained by the material properties, such as magnet flux saturation. The typical magnetic loading for non-cryogenic motor is around 1 T. Any number beyond that is difficult to realize.

The electric loading, also known as copper current density, is 18.6 A/mm^2. It is directly determined by the thermal design of the motor. Our motor electric loading is implemented by a self-pumped air cooling scheme where a centrifugal fan is mounted on the rotor. When the rotor is spinning, cooling air is pumped through the machine, which generates mechanical and electrical losses. As noted in Table 1.2, the typical forced-air-cooled machines have a current density range 5–12 A/mm^2. Our motor current density has around 50% more than the highest feasible value in the air-cooled method, as shown in Table 1.2. In fact, our current density exceeds the highest achieved by the direct-liquid-cooled method. The direct-liquid-cooling method still has a higher current density allowable value, since the thermal resistance between stator windings and coolant is minimized. The advancement in the thermal design makes our motor specific power surpass the current state-of-the-art.

The proposed motor rotating speed is maximized at the same time. The motor rotating speed is determined by the mechanical design. The rated rotating speed of the proposed motor is 15,000 rpm, which corresponds to a tip speed of 265 m/s (0.8 Mach number). The

highest motor tip speed on record is 270 m/s [4]. Our mechanical design is close to the best in class. The tip speed needs to be below the sound speed due to high air-friction losses and material stress constraints. The air-friction losses tend to grow cubically with the tip speed. The high tip speed in our case imposes challenges on the thermal management by creating high windage losses. In addition, the material stress is another challenge in mechanical design at high-tip-speed rotation. High-strength material, such as carbon fiber, is adopted to ensure magnet confinement and structural integrity.

In summary, the high specific power of the proposed motor is not only achieved by a novel topology but also by the advancements in thermal and mechanical design. Especially, the electric loading of the proposed motor surpasses the best-in-class. And two other design factors, tip speed and magnetic loading, are close to the best on record.

1.3   Dissertation Overview

This section summarizes the content of the dissertation highlighting the advances made in the electro-thermal modeling of high-frequency, slotless machines, and component-level validation to reduce design uncertainties and to calibrate the models.

- **Chapter 1: Introduction**

  A 1 MW high-speed permanent magnet motor with specific power over 13 kW/kg and efficiency over 96% is proposed for aircraft applications [1]. It employs a high-pole-count, high-frequency, slotless stator and Halbach-array rotor to reduce iron usage. The high specific power is achieved not only via the lightweight topology concept but also via significantly higher electrical loading than state-of-the-art machines while maintaining high magnetic loading and tip speed. The electric loading (related to the copper current density) of the proposed motor is 50% more than that of comparable air-cooled machines. A basic sizing study is presented in [1], but the electrical, thermal, and mechanical designs are decoupled. Since these three parameters are highly dependent on each other, the optimal design is not achieved at this point.

- **Chapter 2: Electro-Thermal Analytical Modeling**

  To more accurately capture the interaction between the main design parameters listed above, a high-fidelity and computationally efficient electro-thermal analytical model was developed for the proposed motor. With directly coupled EM model to predict performance and losses, and thermal model to predict temperature, along with an assessment of mechanical constraints, one step towards a true multi-physics optimization is taken. This work has been presented in [5] and [6] and is detailed here. Although the FEA simulations are capable of conducting multi-physics analysis, they take hours to run for one design point. However, using the proposed electro-thermal analytical models, thousands of design points can be evaluated within seconds while maintaining accuracy. The torque equation and generalized thermal equivalent circuit model of the proposed motor are presented and verified with FEA simulation results.

- **Chapter 3: Thermal Management Design and Validations**

  One of the biggest challenges in the proposed design is to predict windage loss and fan performance. The tip speeds of typical electrical machines are usually up to 0.5 Mach. However, our motor has a tip speed close to 0.8 Mach. An extremely small ratio between the gap thickness and the rotating radius further complicates windage loss predictions. The windage loss cannot be modeled accurately with analytical methods, but must be calibrated through component hardware tests. The fan performance was validated in a flow test and the windage loss was verified using the same setup. All the experimental results fall within the bounds of theoretical prediction and thus lower the baseline design risks. The 3-D steady-state thermal performance of the baseline design was analyzed and validated with full-size component tests. The thermal resistance and cooling channel heat transfer effects in the proposed thermal model were also validated. This work has been presented in [7] and [8].

- **Chapter 4: Litz Wire Effective Thermal Conductivity**

  Since achieving high electric loading at high frequency is a key enabling factor in maximizing motor specific power, understanding litz wire heat dissipation capability

is critical. Current practice is to treat the litz wire effective thermal conductivity as a 2-D composite problem as presented [9] and [10]. Recognizing that the effective thermal conductivity of the litz cable in the transverse direction is also impacted by the twist pitch, an analytical model including the transposition effects in potted litz wire winding was developed. The model has been verified with FEA simulation and validated with experimental results, showing good agreement. This work has been presented [11] and [12].

- **Chapter 5: Electro-Thermal Analysis and Optimization Design of Slotless Litz-Wire Winding**

  The eddy-current losses in the litz wire in high-frequency motor or transformer applications can be minimized with appropriate cable design, or traded off with cost. However, this may not be the best design approach for high-specific-power motors, since thermal effects should be included along with winding loss density. This chapter establishes a refined electro-thermal analytical model and optimization scheme for a high-frequency slotless litz-wire winding design. The induced-current loss and hotspot temperature models for slotless litz-wire windings are presented and discussed. The litz wire and slotless winding structure parameters such as bundle transposition angle, turn number and strand size are optimized. This work is presented in [13] and [14].

- **Chapter 6: Motor Design Optimization and Case Study**

  The motor optimization toolbox is implemented via the electro-thermal analytical models established in Chapter 2, and the loss models are validated in Chapter 3. The computationally efficient models enable the use of genetic algorithm motor optimization method with numerous cases. The proposed motor design optimization toolbox can be easily integrated into various electric propulsion system studies. One such effort for an integrated hybrid electric engine (Rolls Royce's Electrically Variable Engine) is presented in [15]. The motor sizing and performance of air, engine oil, and water cooling methods with thermal management system (TMS) inputs are studied under takeoff and cruise conditions.

- **Chapter 7: Motor Transient Performance Study of Phase Change Materials (PCM) Integration**

  This chapter describes another use case of the multi-physics model, this time including transient performance: motor peak-power-operation with PCM integration, continuing the hybrid-electric engine integration efforts made in Chapter 6. Two novel phase change material integration methods are proposed using the MW motor as an example. The usage of phase change materials can increase the motor 'thermal inertia' to limit temperature rise during short-term duty. The specific application of the MW motor with PCM integration is tailored to a hybrid-electric engine being developed by partners at Raytheon Technologies. It turns out that applying the proposed PCM integration techniques can cut the motor weight, which is sized at peak-power condition, by nearly 50%. This work has been presented in [16].

CHAPTER 2

ELECTRO-THERMAL ANALYTICAL MODELING

High specific power can be achieved by pushing rotational speed and using lightweight materials and iron-less topology. As rotational speed is increased and component volume is reduced in pursuit of higher specific power, thermal and mechanical designs become more important and can even dominate machine design. Furthermore, one of the key design factors for achieving high specific power is maximizing electric loading under high rotating speed and high-frequency conditions, because magnetic loading has less improvement space due to conventional magnetic materials. Complicated multi-physics correlations make the 1 MW high-specific-power motor design more challenging than before.

Many PM machine optimization discussions focus on deriving high-fidelity electromagnetic analytical models with little or no thermal and mechanical analysis [17], [18], [19], [20], [21]. These models cannot be directly applied to high-specific-power PM machine designs without considering thermal and mechanical aspects. One feasible solution of developing high-specific-power machine optimization is coupling electromagnetic, thermal and mechanical finite-element-analysis (FEA) simulations [22], [23], [20]. Although finite-element methods can provide high-fidelity numerical results, such methods are barely adaptable for large-scale design optimization due to high computational time and inflexible geometry changes.

Meanwhile, most PM machine optimization studies are using inner-rotor topology while few works address outer-rotor topology. An outer-rotor PM machine torque density is optimized by using the finite element method to optimize torque and efficiency performance with analytical mechanical constraints in [22]. However, no thermal analysis is considered. A high-fidelity EM optimization model is established, but no thermal and mechanical models are involved in [19]. According to the past literature, no existing multi-physics outer-rotor PM machine optimization procedure can be used for large-scale optimization. This chapter

Table 2.1: Primary Design Machine Metrics

Rotor Outer Radius	R_o	0.1588	m
Magnet Outer Radius	R_m	0.1508	m
Rotor Inner Radius	R_r	0.1383	m
Winding Outer Radius	R_w	0.1373	m
Stator Yoke Outer Radius	R_{sy}	0.1318	m
Active Length	L	0.2295	m
Gap Thickness	δ	0.001	m
Magnet Remnant Flux	B_{rem}	1.15	T
Magnet Permeability	μ_r	1.04	
Rotating Speed	ω_m	15000	rpm
Pole Pair	p	10	
Slot Current Density	J_s	7.25	Arms/mm^2
Stacking Factor		97%	
Iron Yoke Saturation Flux	B_{sat_sy}	2.0	T

reports on development a computationally efficient machine design tool that is compatible with large-scale optimization.

2.1 Electromagnetic Analysis

Electromagnetic analysis is a primary step in machine design that determines primary machine performance. The finite-element method is broadly used by current machine design commercial software. However, such method does not provide geometry variation flexibility of this specific novel machine topology for electric aircraft application. If a large-scale optimization of machine performance needs to be carried out, it is rather tedious to modify geometry parameters, especially for complicated design. Another disadvantage of using FEM is that it is computationally time-consuming. It has to evaluate every node point value of the automatically generated mesh and involves a large matrix calculation with thousands to millions of entries. For a small number of design cases, total evaluation time is not excessive, maybe merely several seconds. But if the design cases accumulate, total evaluation time will increase linearly and end up at hours or days. To avoid heavy computations with FEM, an accurate analytical EM model derived from fundamental Maxwell's equations is employed in this work.

The EM analytical model arises from Maxwell's equations. In electrical machines, EM waveform frequency is fairly low and no displacement current occurs. It is usually treated as a magneto-static problem. And following are governing equations in the electrical machine EM analytical model:

$$\nabla \times \vec{H} = \vec{J} \tag{2.1}$$

$$\nabla \cdot \vec{B} = 0 \tag{2.2}$$

For non-magnet regions, the magnetic flux density and flux intensity relation can be written as

$$\vec{B} = \mu_o \mu_r \vec{H} \tag{2.3}$$

For magnet regions, there is extra magnetic flux density contributed by permanent magnet material, since permanent magnet material possesses remanent flux and does not require a current source to produce magnetic flux. Therefore, magnetic flux density and flux intensity relation with permanent magnet effects yields

$$\vec{B} = \mu_o \mu_r \vec{H} + \mu_o \vec{M} \tag{2.4}$$

The magnetization distribution $\vec{M}$ varies sinusoidally along the rotor angle θ and is given by

$$\vec{M} = M \cos(p\theta)\hat{r} + M \sin(p\theta)\hat{\theta} \tag{2.5}$$

where M is defined as B_{rem}/μ_o.

Since this is an open-circuit magnetic flux analysis, the current density in the winding region is zero. That means the rotation part of magnetic flux intensity vector $\vec{H}$ is zero and only the gradient part exists. Therefore, a magnetic scalar potential (Φ_M) can be employed here:

$$\vec{H} = -\nabla \Phi_M \tag{2.6}$$

And tangential and rotational components of magnetic fields can be obtained from scalar magnetic potential as

$$\vec{H_r} = \frac{\partial \Phi_M}{\partial r} \tag{2.7}$$

10

$$\vec{H}_\theta = -\frac{1}{r}\frac{\partial \Phi_M}{\partial \theta} \qquad (2.8)$$

The machine magnetic field is predicted based on the following assumptions: (1) The Halbach array is assumed to form a perfect sinusoidal magnetic waveform in the air gap. (2) The back yoke permeability in the stator is regarded as infinite to simplify the problem. (3) Harmonics in magnetic waves are ignored over here since they do not contribute to the average torque and their amplitude is negligible compared with the fundamental. (4) The current is assumed as a perfect sinusoidal source due to the high-frequency multi-level inverter developed by [24].

The radial and tangential magnetic field analytical solution in the slotless winding region is derived as [25]:

$$B_r(r,\theta) = \frac{4B_{rem}}{D_0}\frac{p}{1-p}(1+\mu_r)\left[1-\left(\frac{R_r}{R_m}\right)^{p-1}\right]$$
$$\left[1+\left(\frac{R_{sy}}{r}\right)^{2p}\right]\left(\frac{r}{R_r}\right)^{p-1}cos(p\theta) \quad (2.9)$$

$$B_\theta(r,\theta) = -\frac{4B_{rem}}{D_0}\frac{p}{1-p}(1+\mu_r)\left[1-\left(\frac{R_r}{R_m}\right)^{p-1}\right]$$
$$\left[1+\left(\frac{R_{sy}}{r}\right)^{2p}\right]\left(\frac{r}{R_r}\right)^{p-1}sin(p\theta) \quad (2.10)$$

where

$$D_0 = 2(1-\mu_r)\left[(1-\mu_r)\left(\frac{R_r}{R_m}\right)^{2p}+(1+\mu_r)\left(\frac{R_{sy}}{R_m}\right)^{2p}\right]$$
$$-2(1+\mu_r)\left[(1+\mu_r)+(1-\mu_r)\left(\frac{R_{sy}}{R_m}\right)^{2p}\right] \quad (2.11)$$

All the results of the established EM model strongly agree with the FEA results of the proposed motor shown in Figure 2.1. Given the primary design metrics listed in Table 2.1, the open-circuit magnetic fields of analytical solution exactly match the FEA with no more
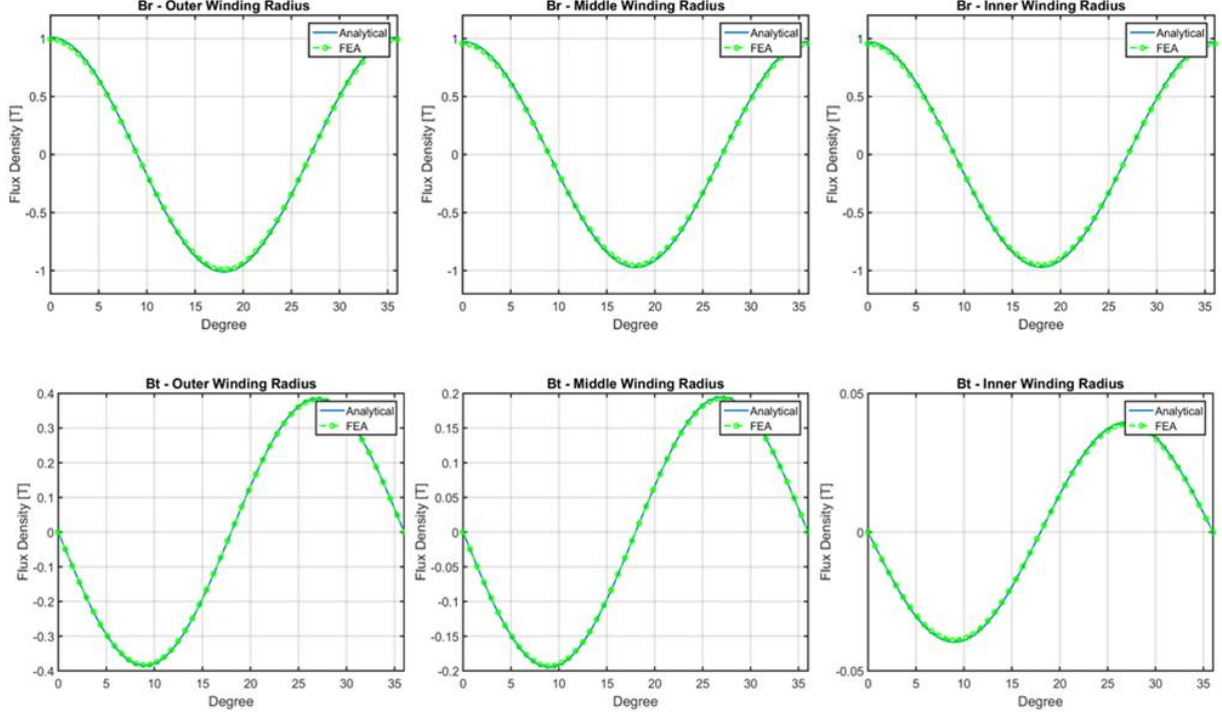
Figure 2.1: Comparisons between the EM Analytical and FEA Results of Radial and Tangential Flux Density in the Winding Region

than 2.7% error, which is verified at the winding outer, middle, and inner radius respectively. Only the fundamental waveforms are compared in this case since the flux density produced by the Halbach array is the closely sinusoidal waveform shown in Table 2.2. By the Lorentz force law, the average torque in the proposed motor can be obtained as:

$$
T_e = \frac{4\pi B_{rem} J_{s\_pk} L}{D_0} \frac{p}{1-p}(1+\mu_r) \left[1 - \left(\frac{R_r}{R_m} \right)^{p-1} \right]
$$
$$
\left[\frac{1}{p+2} \frac{R_w^{p+2} - R_{sy}^{p+2}}{R_r^{p-1}} + \frac{1}{2-p} \frac{R_{sy}^{2p}}{R_r^{p-1}} \left(R_w^{-p+2} - R_{sy}^{-p+2} \right) \right] \quad (2.12)
$$

The average torque of the primary design in Table 2.1 is estimated as 636.6 Nm by the developed analytical solution, which has around 3.1% error compared with the FEA result. The errors in the magnetic flux density estimation propagate to the torque prediction, so the torque estimation errors could result from the assumptions made before.

Since iron is one of heaviest materials used in electrical machines, quantifying iron yoke volume/thickness is important to evaluating machine overall weight correlated with magnetic

Table 2.2: Odd Harmonics of Radial Flux Density at Outer Winding Radius

Harmonic Number	Normalized Amplitude
1	99.50%
3	0.03%
5	0.03%
7	0.02%
9	0.02%
11	0.08%
13	0.36%
15	0.08%

loading. Minimum stator yoke thickness (d_{sy}) can be derived from the flux distribution analytical solution. The according equation can be derived as

$$d_{sy} = \frac{R_{sy}}{p} \frac{B_{r\_sy}}{B_{sat\_sy}} \tag{2.13}$$

where B_{r_sy} is radial flux density at $r = R_{sy}$ evaluated in Equation (2.9), and B_{sat_sy} is stator yoke saturation flux density.

2.2   Steady-State Thermal Analysis

High rotating speed creates strong forced convection effects at the outer rotor and gap surfaces. The heat transfer coefficient in the gap can be obtained by [26]. In addition, most of the cooling air flows through the cooling channels attached underneath the stator yoke. The forced convection coefficient associated with the cooling channels can be estimated by [27], [28]. The winding has the highest risk of overheating due to its poor radial thermal conductivity, high loss density and obstacles to access cooling flow directly. For efficient computation, it is sufficient to model the stator 2-D thermal equivalent circuit to detect the hotspot temperature. The 2-D thermal equivalent circuit of the stator is presented in Figure 2.2. The total number of nodes assigned is $3 + N_w + N_{sy}$, including N_w winding region nodes and N_{iron} iron region nodes. The node index is denoted as i in the whole thermal equivalent circuit analysis. The temperature potential node index is characterized
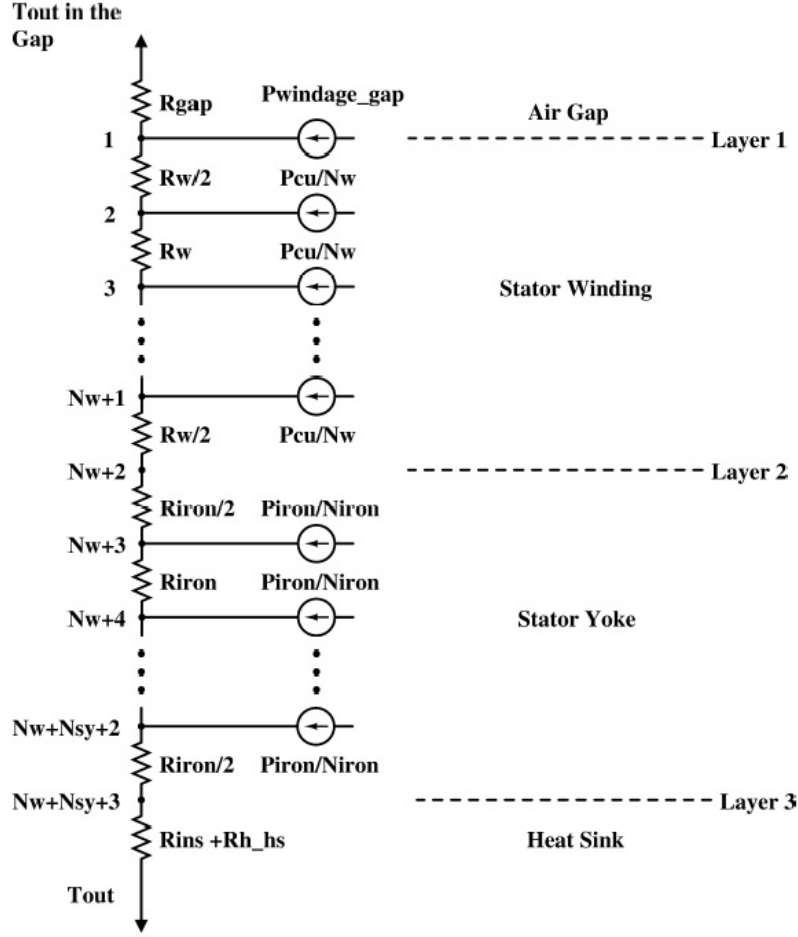
Figure 2.2: 2-D Steady-State Thermal Equivalent Circuit in Stator

as $i_w = \{2, ..., (1 + N_w)\}$ for the winding region, $i_{iron} = \{(3 + N_w), ..., (N_{sy} + N_w + 2)\}$ for the stator yoke region, and $i_{layer} = \{1, (N_w + 2), (N_w + N_{sy} + 3)\}$ for the interface layers. Then, thermal admittance matrix G entries can be specified as follows:

$$G_{i,i} = \frac{1}{R_i} + \frac{1}{R_{i+1}}, \quad G_{i,(i+1)} = G_{(i+1),i} = -\frac{1}{R_{i+1}} \tag{2.14}$$

The thermal resistance at the interface between the air gap and stator winding is:

$$R_1 = R_{gap} = \frac{1}{h_{gap} A_{gap}} \tag{2.15}$$

14

Table 2.3: Stator Temperature Prediction Comparison with FEA

Temperature	FEA	Analytical	Error
T1	140	147.07	5.05%
T2	138.5	147.14	6.22%
T3	132.4	144.36	9.07%
T4	126.6	138.67	9.52%
T5	119	130	9.27%
T6	117.1	128.33	9.64%

where h_{gap} is the gap heat transfer coefficient and A_{gap} is the stator outer surface area. The thermal resistances in the winding and iron region yield:

$$R_{winding} = ln(\frac{R_w - d_w \cdot \frac{i-2}{N_w}}{R_w - d_w \cdot \frac{i-1}{N_w}})/(2\pi k_{winding}) \tag{2.16}$$

$$R_{iron} = ln(\frac{R_{sy} - d_{sy} \cdot \frac{i-3-N_w}{N_{iron}}}{R_{sy} - d_{sy} \cdot \frac{i-2-N_w}{N_{sy}}})/(2\pi k_{iron}) \tag{2.17}$$

where d_w is the winding slot depth, $k_{winding}$ is the winding equivalent radial thermal conductivity, d_{sy} is the stator yoke depth, and k_{iron} is the iron yoke radial thermal conductivity. Thermal resistance in the heat sink region is

$$R_{N_w+N_{sy}+4} = R_{ins} + R_{hs} = \frac{t_{ins}}{A_{ins}k_{ins}} + \frac{1}{h_{hs}A_{hs}} \tag{2.18}$$

where t_{ins} is the insulator thickness, A_{ins} is the insulator layer surface area, h_{hs} is the heat sink average heat transfer coefficient, and A_{hs} is the heat sink total effective cooling area.

The heat sources injected into the thermal equivalent circuit nodes can be predicted. After constructing the admittance matrix of the thermal equivalent circuit, the temperature potentials at the defined nodes can be calculated by the network theory:

$$G \cdot T = P \tag{2.19}$$

The stator temperature prediction of the thermal equivalent circuit is consistent with the FEA result. The hotspot temperature prediction error is 5.05% shown in Table 2.3, when
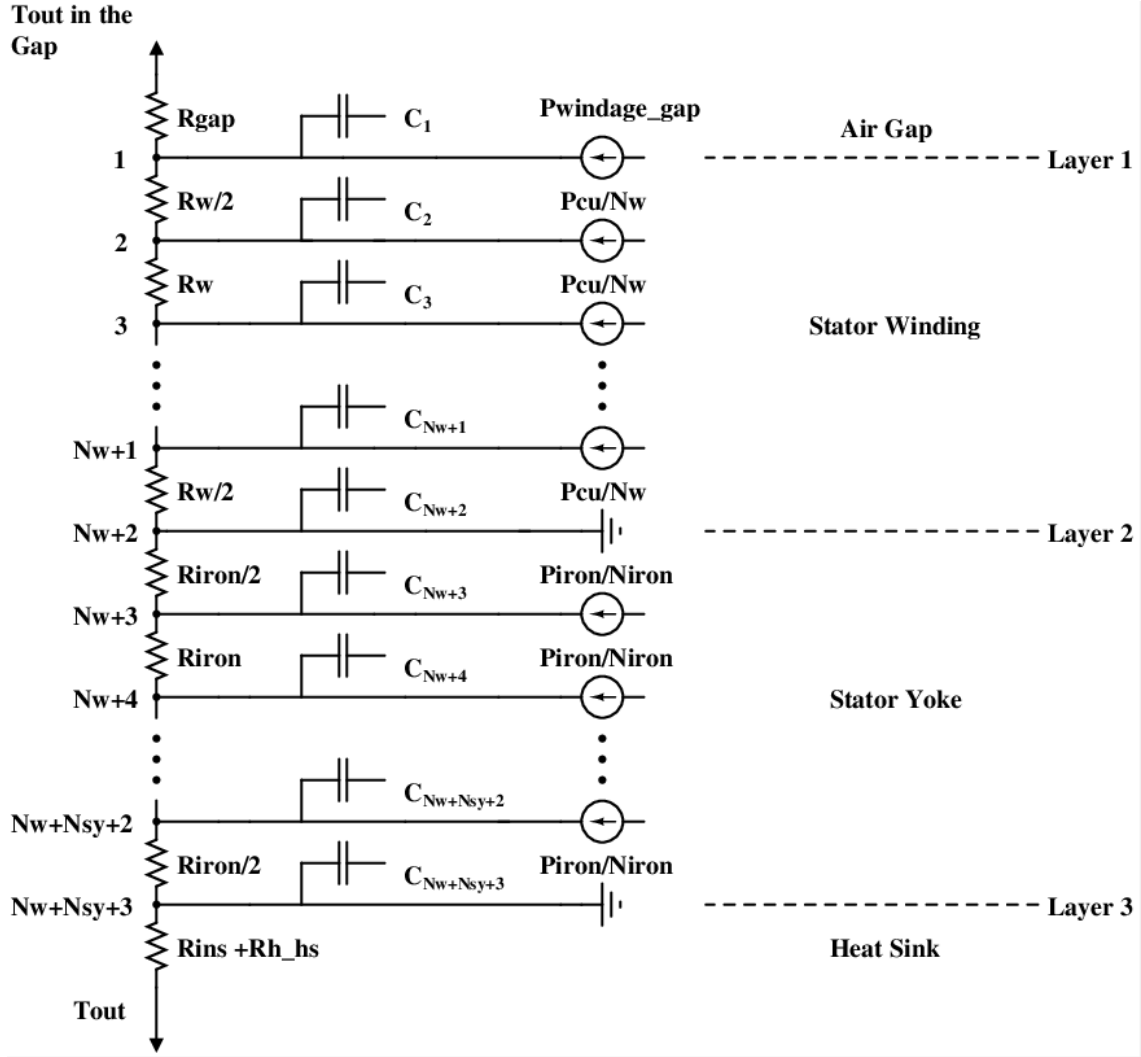
Figure 2.3: 2-D Transient Thermal Equivalent Circuit in Stator

three winding nodes, and one iron node are selected in the developed thermal equivalent circuit. Due to the different sizes of lumped components, the temperature prediction accuracy varies at different nodes. The thermal analysis accuracy can be improved by increasing the decomposing number in the high temperature variation components.

2.3 Transient Thermal Analysis

The motor transient thermal performance could be important in motor design. In transportation applications, peak power operation for short time is needed in the way of boosting

16

electric loading. The transient thermal analysis is similar to the steady-state thermal analysis. The transient thermal equivalent circuit uses the same circuit network with the heat capacitance inserted at each component node shown in Figure 2.3. The temperature at each node needs to be evaluated at each time step. The governing transient thermal equivalent circuit formulation is given as:

$$C\frac{dT}{dt} + G \cdot T = P \tag{2.20}$$

where C is the capacitance matrix, G is the admittance matrix of the transient thermal circuit (the same as in the steady-state thermal equivalent circuit), and P is the heat loss vector.

Since (2.20) is a differential equation, the Euler method can be applied to evaluate temperature change at each time step. Such a method could depend on the time step size. A small time step can guarantee the Euler method convergence and accuracy. Also, it is assumed that the matrix C and the vector P are constant for now. If the matrix C and the vector P are time-dependent, other advanced numerical methods can better evaluate the motor thermal transient performance. The evaluation equation for each time step can be derived as:

$$C_t\frac{T_{t+1} - T_t}{dt} + G_t \cdot T_t = P_t \tag{2.21}$$

where the subscript t means the previous (current) step matrix information, the subscript $t + 1$ means the matrix at the current (future) step. The unknown matrix over here is the matrix with the subscript $t + 1$. And its corresponding evaluation equation can become:

$$T_{t+1} = C_t^{-1} \cdot dt(P_t - G_t \cdot T_t) + T_t \tag{2.22}$$

where dt is the time step size. The capacitance matrix is a $3 + N_w + N_{sy}$ by $3 + N_w + N_{sy}$ matrix with capacitance value inserted into the diagonal line. Each node capacitance value can be inserted into the corresponding index entry on the diagonal axis.

2.4 Mechanical Constraint

Since the inside-out motor operates at high speed, the rotor radial expansion will be the main performance and reliability concerns. The right retaining ring thickness needs to be determined to ensure magnets can be confined and rotor expansion is tolerable at high tip speed operation. This section details one analytical method to predict rotor expansion and size retaining ring with various tip speed and magnet volume according to [29].

The centrifugal force of rotating magnet arrays is

$$
\begin{aligned}
F_c &= \int_{R_m-D_m}^{R_m} 2\pi r L \rho_m \frac{(\omega_m r)^2}{r} dr \\
&= \frac{2\pi}{3} \rho_m L \omega^2 \left(R_m^3 - (R_m - D_m)^3 \right)
\end{aligned}
\tag{2.23}
$$

where D_m is magnet depth, ρ_m is magnet density, and ω_m is rotating speed. The hoop stress of retaining ring is due to the centrifugal force generated by rotating magnet arrays. The hoop force at inner retaining ring radius yields:

$$
F_h = \frac{1}{2} \int_0^\pi sin\theta \frac{\partial F_c}{\partial \theta} d\theta
\tag{2.24}
$$

With the hoop force of retaining ring, the radial expansion can be calculated according to the average hoop stress and Hooke's law. The retaining ring radial expansion ($\triangle r$) formula becomes

$$
\triangle r = \frac{F_h}{d_{rr}L} \frac{R_m}{E}
\tag{2.25}
$$

To simplify the retaining ring sizing process, the radial expansion is fixed as 0.387 mm. And the carbon fiber composite material, IM-7/PEEK, provides 376 GPa. After reformulating the previous equations, the retaining ring sizing equation yields

$$
d_{rr} = \frac{1}{3} \frac{\omega_m^2}{E} \frac{R_m}{\triangle r} (R_m^3 - (R_m - D_m)^3)
\tag{2.26}
$$

Rotor dynamics is not analyzed in this design optimization procedure because it heavily relies on the motor structure design and bearing selection. These two factors are difficult to

determine at the primary sizing optimization stage. And it is not necessary to evaluate rotor dynamics performance during the sizing process. Further design decisions can be made with a more rigorous mechanical analysis in commercial softwares.

CHAPTER 3

THERMAL MANAGEMENT DESIGN AND VALIDATION

In the high-specific-power motor design for aerospace applications, thermal management is the key enabling factor. The conventional motor topologies tend to be lower-speed machines ($<$ 1 kHz) with tooth windings and direct-conductor cooling since lower electrical frequency does not pose the challenges of managing iron losses. Siemens developed a 250 kW Halbach-array SPM machine with direct cooled conductors for planes with four seats [30]. For higher-speed motors in the high-specific-power applications, indirect cooling and end-winding spray coolings are preferred. Honeywell designed and tested a 540 kW wound-field synchronous motor with both engine oil cooling and end-winding spray for hybrid electric aircraft application [31]. The liquid cooling has the advantages of allowing higher current density and direct coolant control. But it reduces effective copper volume in the machine and adds extra weight and complexities to the overall motor.

By comparison, our proposed motor adopts aggressive air cooling while retaining the high current density enabled by conventional liquid cooling, as mentioned above. In addition, high tip speed and high frequency add more stresses and challenges in this MW high-specific-power motor design. All of these challenges are tackled through delicate analysis and hardware validations in Chapters 3 to 5, from the smallest component, litz wire, to the full-scale rotor and stator validations.

3.1   Thermal Management Overview

Understanding the machine heat and cooling paths is crucial to the cooling design. The air cooling method of the proposed machine is implemented by a centrifugal fan mounted on the rotor. When the rotor is spinning, cooling air is pumped through the machine, which

generates mechanical and electrical losses. The mechanical losses are air-friction and bearing
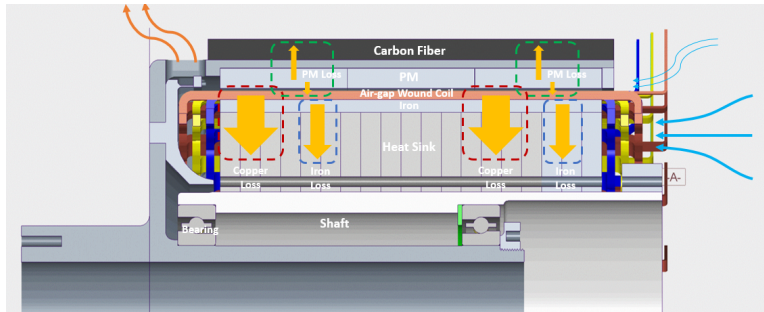
Figure 3.1: Heat Flow Path and Cooling Passages Illustration

losses. The former occurs at highly rotating surfaces and is blown into the ambient air. The latter is conducted through the stator to the heat sink and from there to the outside air. Electrical losses are generated at active components, including the magnet, winding and yoke. Most of the electrical losses are transferred into the heat sink; the remainder escape into the air gap. When the centrifugal fan pumps cooling air through the heat sink and the air gap, that air is heated by the machine losses and expelled out the exit holes in the titanium shell, as shown in Figure 3.1.

3.2 Windage Loss Prediction and Validation

3.2.1 Windage Loss

Quantifying friction and windage losses is difficult. Since a self-pumped air cooling scheme is picked and rotating speed is high (up to 15,000 rpm), fluid dynamics could become unpredictable and full of uncertainties. At present, there is little published work on rotating cylinder or concentric rotating cylinders rotating at such high tip speed (close to 0.8 Mach number) in the air. Developed fluid dynamics theories might not be able to cover the turbulent flow problems in this exact situation. In addition, the gap thickness in the proposed motor is extremely small compared with the rotating radius. Then, a large shear stress gradient is caused within the extreme small gap at the high-rotating condition. Both experiments and fluid dynamic modeling have difficulty measuring and predicting the flow behavior for

such a case.

Although there is no empirical correlation that covers the Reynolds number and gap-over-rotor-radius ratio of the proposed motor operation, selected empirical correlations are still assumed to be valid. Two motor components generate windage loss. One is the outer surface of the rotating rotor, at which windage loss can be estimated by [32], [33]. The other is the gap between the concentric cylinders while the outer cylinder is rotating, at which windage loss can be predicted by [32], [34], [35]. Disk windage loss could become non-negligible in this case. All these windage losses result from turbulent flow during high-speed rotor spinning.

3.2.2   Gap Windage Loss

Reynolds number in the gap of concentric cylinders is defined as

$$Re = \frac{\omega R \delta}{\nu} \tag{3.1}$$

where ω is rotating speed, R is rotating surface radius, δ is gap thickness, and ν is flow dynamic viscous coefficient. The associated friction coefficient is obtained by [32], [35] :

$$C_{cm} = \left(\frac{1}{-0.8572 + 1.25 ln(Re\sqrt{C_{cm}})} \right)^2 \tag{3.2}$$

$$C_{cm} = 0.065(\delta/R)^{0.3} Re^{-0.2} \tag{3.3}$$

With the friction coefficient, the gap windage loss is

$$P_{gap} = \frac{1}{2}\pi \rho \omega^3 R^4 L C_{cm} \tag{3.4}$$

Both correlations are used to define the upper and lower prediction range boundaries of gap windage loss.
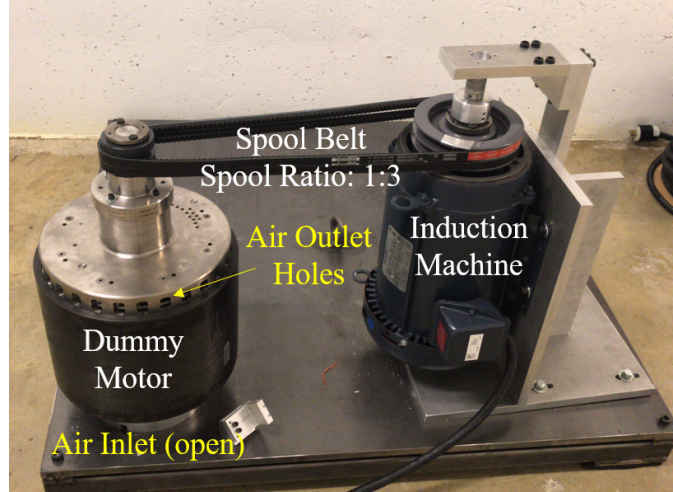
(a) Hardware Setup
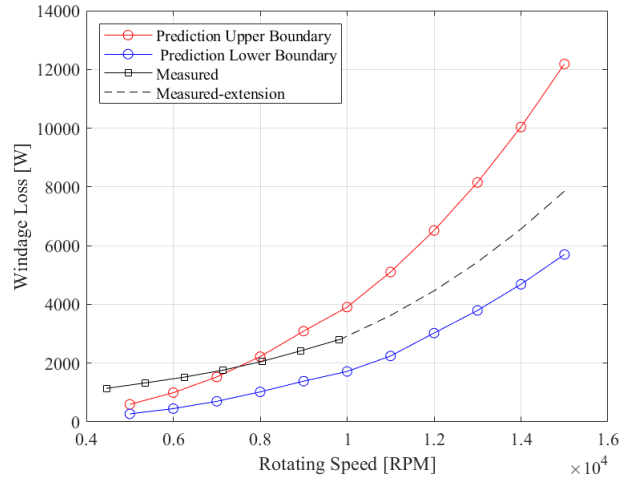
(b) Experimental Results

Figure 3.2: Windage Loss Validation Test

3.2.3 Outer Rotor Windage Loss

Reynolds number of a rotating cylinder in the ambient fluid (air in our case) is defined as

$$Re = \frac{\omega R_o^2}{\nu} \tag{3.5}$$

where ω is rotating speed, R_o is rotating surface radius (outer rotor radius), and ν is flow dynamic viscous coefficient.

Since there are few papers studying the friction loss correlation of rotating cylinder in free

23

air, some gap windage loss correlations are used with an assumption that the gap thickness is equal to the rotating cylinder radius. While [32] has the gap windage loss prediction correlation, it is also used for the outer rotor windage loss prediction by applying Equation (3.3). The second empirical correlation to predict outer rotor windage loss is given by [33]. The friction correlation of [33] is:

$$C_{mc} = \left(\frac{1}{0.8572 + 1.25ln(Re\sqrt{C_{mc}})} \right) \tag{3.6}$$

Then, the outer rotor windage loss becomes:

$$P_{outer\_rotor} = \pi C_{mc} \rho R_o^2 \omega^3 L \tag{3.7}$$

Similarly, two correlations are used to identify the prediction upper and lower boundaries of outer rotor windage loss. The total windage loss of the proposed outer-rotor motor should include both gap and outer rotor windage loss.

3.2.4   Validation Results

The dummy motor with no active components, magnet, winding and yoke, is used for mechanical validation at the initial development. Figure 3.2a shows the hardware test setup. Rotation of the dummy motor is driven by the induction motor using pulleys connected through two belts, as shown in Figure 3.2a. The pulley ratio between the dummy motor and the induction motor is 1:3. Thus, the rotating speed of the dummy motor is three times that of the induction motor. In this way, the test speed range of the dummy motor can be expanded, since the induction motor can only spin up to 3600 rpm. So the test span of the dummy motor is up to 9800 rpm, which is around 66% of the rated speed.

The designed centrifugal fan works correctly when rotating counterclockwise from the shaft end. If the dummy motor spins in the opposite fan direction, the loss consumed by the dummy motor spinning can be regarded as the total windage loss caused by the rotating rotor. Figure 3.2b presents the prediction and experiment results. The experimental curve falls within the prediction range, including the cubic project portion of the experimental

curve. Approximately 3.5 kW windage loss is measured at 9800 rpm. According to the cubic projection, 8 kW windage loss is then expected at the rated rotating speed. The measured windage loss could be overestimated since only the induction motor electrical power was measured. Both belt friction loss and a small amount of fan pumping power are also included in the windage loss measurement.

3.3 Fan Design Validation

A fan must be either axial or centrifugal. An axial fan provides only limited pressure rise because it cannot change with the radius. Thus, a centrifugal fan was chosen; it can overcome the pressure drop of cooling air through the heat sink and can be integrated into the cantilevered machine shape by varying radius and blade angle from leading to the trailing edge.

The fan design comprises several steps. First, a thermal circuit and ANSYS model were used to determine the necessary air speed through the heat sink—20 m/s. Then, computational fluid dynamics (CFD) was employed to find the pressure drop through the heat sink due to the air flow—0.6 psi.
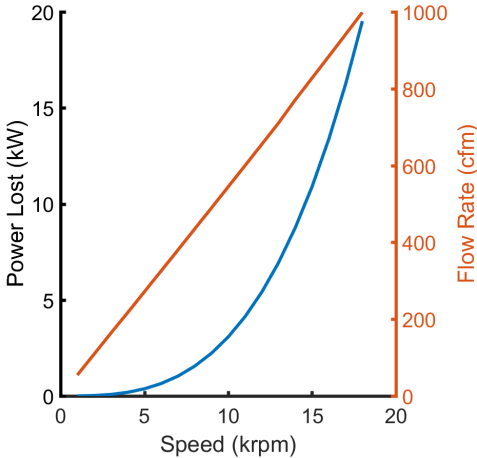
Figure 3.3: Power Lost (Blue) and Flow Rate (Orange) Predicted by 1-D Code

Next the fan blades must be designed to meet the cooling-flow target found in the thermal analysis and pressure drop predicted in the CFD. This design is done iteratively using a

(a) Rotor Section View Showing Fan and Exit Holes

(b) Manufactured Fan
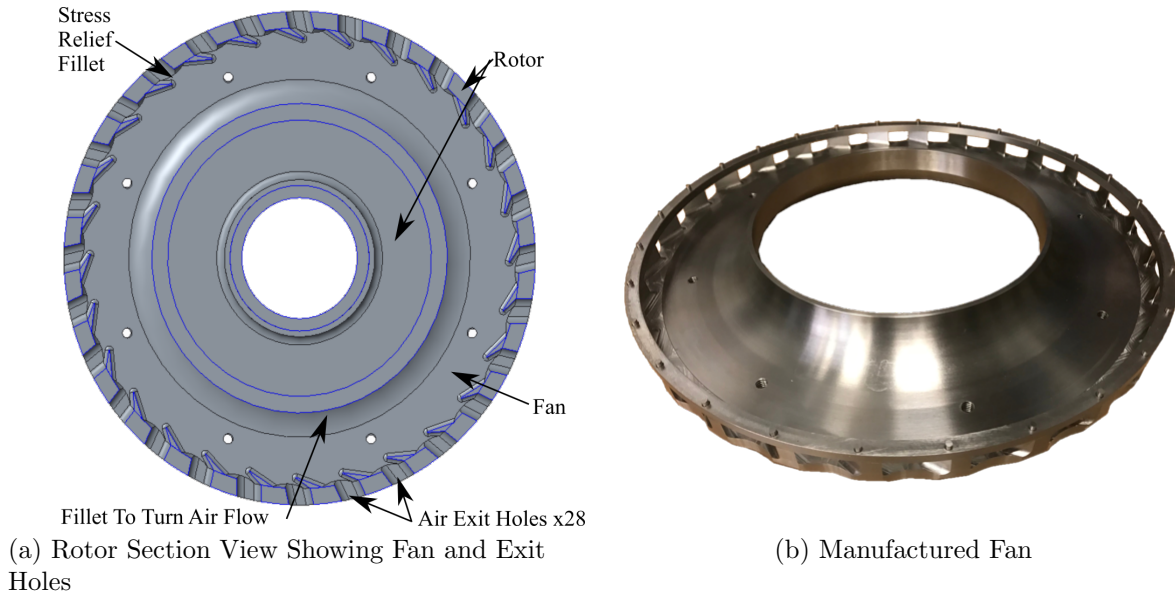
Figure 3.4: Centrifugal Fan Design

one-dimensional (1-D) model [36]. The fan is over-designed to account for pressure drops such as those in the end-winding regions not included in the CFD model. The flow rate calculated by our 1-D code is plotted in Figure 3.3.

For a certain rotational speed, there is an angle of incidence which optimally overcomes the built-up pressure to create air flow. This angle is 75 degrees from tangent and defines the leading-edge angle of the centrifugal fan blades. Because of the pressure rise required by the rotor and the diffusion factor of aerodynamic loading limits, the blade number and trailing edge were chosen to be 28 and 58 degrees, respectively. The final fan design is displayed in Figures 3.4a and 3.4b. Figure 3.4a gives a section view of the rotor with its fan and air exit holes. One fillet type (singular) is used to aid in turning the air flow from axial to radial. The other type (multiple) between fins around the rotor is used to relieve stress concentration at the fan blade rotor interface.

3.3.1   Flow Sensor Calibration

The pressure sensor used in the test is a Pitot tube. The total pressure is measured by placing the Pitot tube opposite the axial cooling flow direction at target locations. If it is pointing perpendicular to the axial flow speed, the result is static pressure at that point.
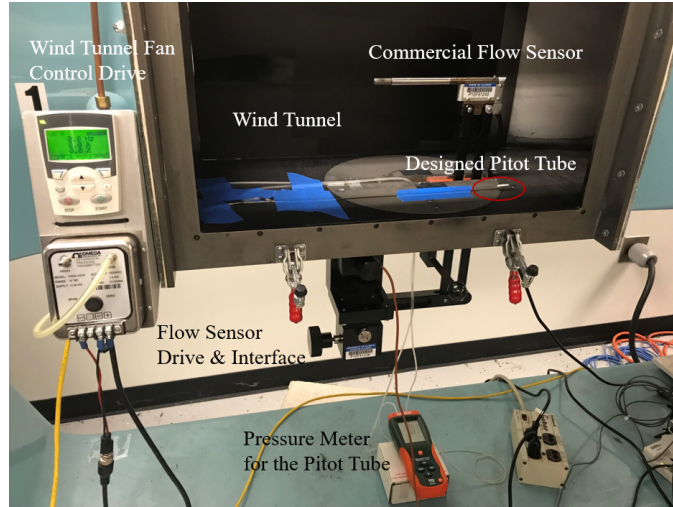
(a) Flow Test Illustration
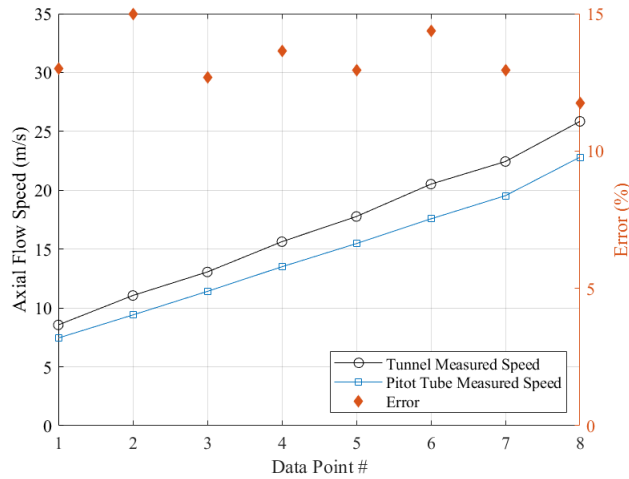
(b) Calibration Measurement

Figure 3.5: Pitot Tube Calibration Test

The difference between total pressure and static pressure at a measured point is the dynamic pressure due to axial air flow. Given dynamic pressure, the axial flow speed can be obtained by the Bernoulli equation:

$$v_{axial} = \sqrt{2(P_{total} - P_{static})/\rho} \tag{3.8}$$

Although commercial hotwire and Pitot tube can measure flow axial flow speed more accurately, commercial hotwire is too big to fit in the motor cooling channels. The dimensions of a cooling channel crossection area are 3–6 mm by 40 mm. The normal hotwire and Pitot tube have at least 5 mm of diameter. A customized Pitot tube was manufactured to

27
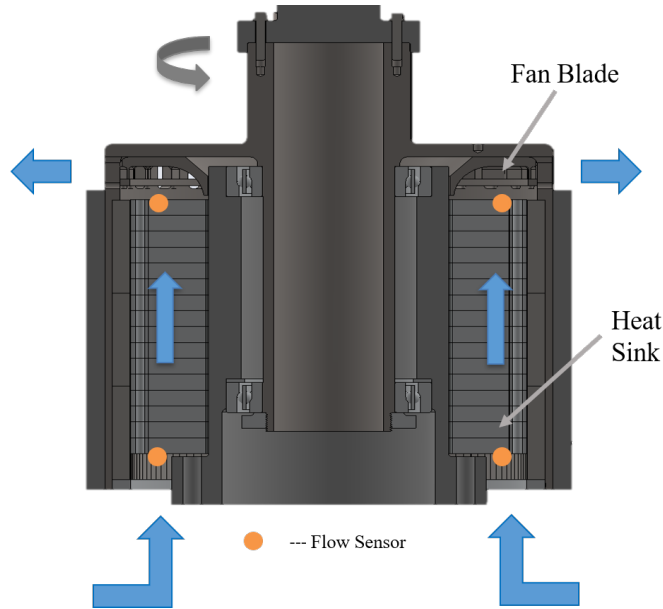
Figure 3.6: Coolant Flow Directions and Sensor Locations in Fan Performance Validation Test

minimize blocking flow effects while enabling measurement of air axial flow speed. Although the customized Pitot tube is designed to have the minimum dimensions (1.5 mm by 5 mm), its small size cannot allow the measured flow to develop fully. That means the customized Pitot tube has inherent measurement errors due to deficit space. A calibration test is desired to validate its performance. The corresponding Pitot tube calibration test was conducted in a well-designed wind tunnel to verify its accuracy, as presented in Figure 3.5a. It turns out the customized Pitot tube speed measurement has good consistency with the accurate speed measurement in the wind tunnel. The average error is around 15% according to Figure 3.5b.

3.3.2   Fan Performance Experiment

The same setup for the windage loss test is used to validate fan performance. But the dummy motor rotation needs to be counterclockwise to pump flow sufficiently. Cooling air is pumped from the motor bottom and expelled at the top outlet holes by the integrated centrifugal fan. The flow path within the dummy motor is detailed in Figure 3.6. The axial flow speed and pressure drop within the heat sink are verified at several rotating speeds. Two sets of pressure sensors are mounted at 0 and 180 degrees, along the tangential axis,
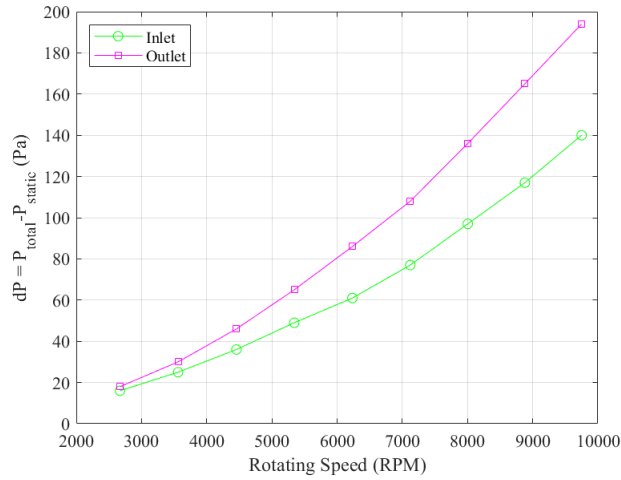
(a) Calibration Measurement
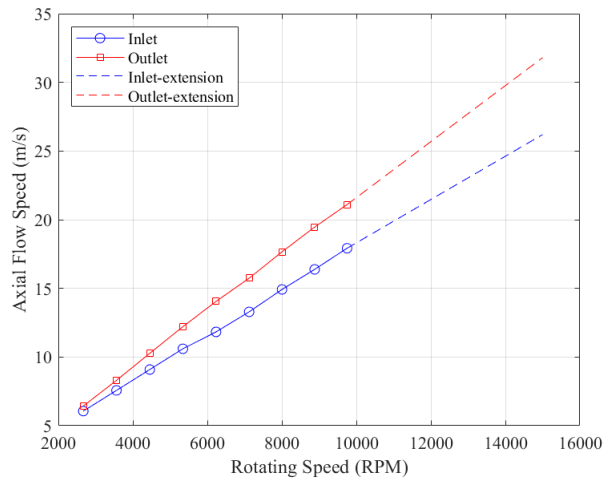
(b) Flow Speed

Figure 3.7: Fan Performance Validation Test

illustrated in Figure 3.5b.

The flow test verified the inlet and outlet axial flow pressure difference ($dP = P_{total} - P_{static}$) and speed within a medium speed range of the proposed motor. Figure 3.7a shows the dP measurements at the inlet and outlet Pitot tube sensor locations. The outlet measurement tends to have higher pressure difference compared with the inlet measurement. It is consistent with the centrifugal fan characteristics of having higher flow speed close to the fan blades. Figure 3.7b presents inlet and outlet axial flow speed in a rotating speed range from 3000 to 9800 rpm. Both curves follow a linear correlation. With the current measurement

Table 3.1: Component Material Thermal Conductivity

Component	Material	Perpendicular(W/mK)	Parallel(W/mK)
Retaining Ring	Carbon Fiber (IM-7/PEEK)	0.253	6.5
Rotor Inconel Shell	Inconel Alloy	15.9	15.9
Permanent Magnet	NdFeB	6.75	6.16
Insulator	Epoxy	1	1
Winding	Copper, Resin and Air	0.47	177.8
Stator Yoke	Iron	67	67
Thermal Fins	Aluminum	206	206
Ground Layer	Aluminum	206	206

result and linear relation projection, the axial flow speed at the rated speed 15,000 rpm can reach 25–35 m/s. According to the previous thermal analysis results, 20 m/s axial flow speed is sufficient for cooling the proposed motor under Class H insulation temperature limit. The flow test results seem promising and indicate that our target mass flow rate can be achieved.

3.4 Motor Thermal Simulation Modeling

3.4.1 Steady-State Thermal Analysis

Given the loss estimations and mass-flow rate specified by the fan design, the machine steady-state temperature profile can be generated. A detailed thermal modeling in the proposed machine is discussed in this section.
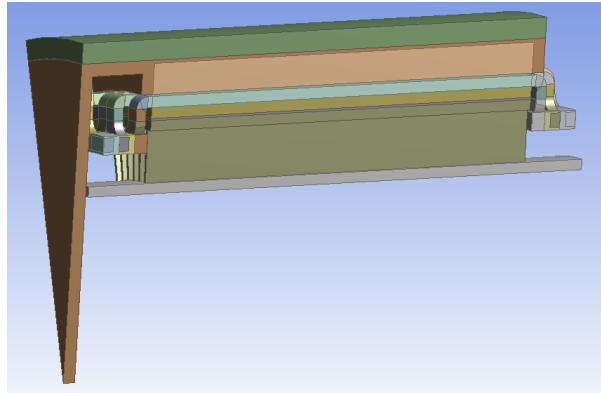
Figure 3.8: Machine Geometry of One Pole

For saving computational time, machine temperature is predicted by thermal steady-state

Table 3.2: Loss Breakdown Summary

Copper Loss (DC)	6.7	kW
Copper Loss (AC)	1.7	kW
Iron Loss	2.1	kW
Magnet Loss	0.5	kW
Windage Loss	$5 - 12$	kW
Bearing Loss	0.2	kW

conduction analysis with estimated heat transfer boundary conditions. The exact machine geometry in Figure 3.8 is modeled in ANSYS for accurate thermal prediction. In order to shorten computational time, only one pole slice of the machine is used in thermal steady-state analysis by the symmetry principle. The rotor solid part is decoupled from the stator solid part.

Boundary conditions are estimated with empirical correlations provided in the literature. It is assumed that estimated heat transfer coefficients are average values in time and spatial domains. Rotor outer surface experiences strong convection effects due to its high-speed rotation. It is regarded as a rotating cylinder in quiescent air and its heat transfer coefficient is estimated in [37], [38], [39]. Heat transfer in the gap of concentric rotating cylinders is given in [40], [41], [42]. Rotor rotating ending is similar to a rotating disk. Its associated convection effects is predicted by [43], [44]. Convection cooling also occurs at the end-region, especially the end-winding. End-winding region heat transfer is similar to the flow through flat plane and is estimated by [45]. Estimation of cooling channels heat transfer can be treated as a problem of inner flow in a hydraulic pipe [28].

The target axial flow speed is set as 20 m/s for the initial machine design. The following flow test verifies whether target axial flow speed can be reached within cooling ducts. Inlet temperature is assumed as 40 °C. The component material thermal conductivity is listed in Table 3.1. Materials such as carbon fiber and winding are mixture-type materials that have various thermal conductivities in different directions.

The temperature distribution results are collected from the ANSYS steady state thermal analysis simulator. With the heat loads in Table 3.2 and boundary conditions estimated, Figures 3.9 and 3.10 show the temperature contour of the stator and rotor.
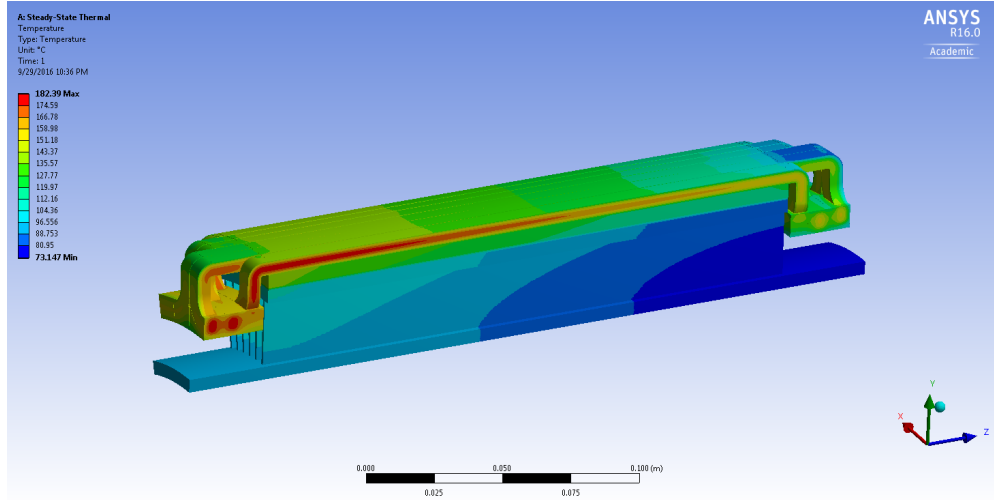
Figure 3.9: Stator Temperature Distribution with Outlet Temperature at 86 °C
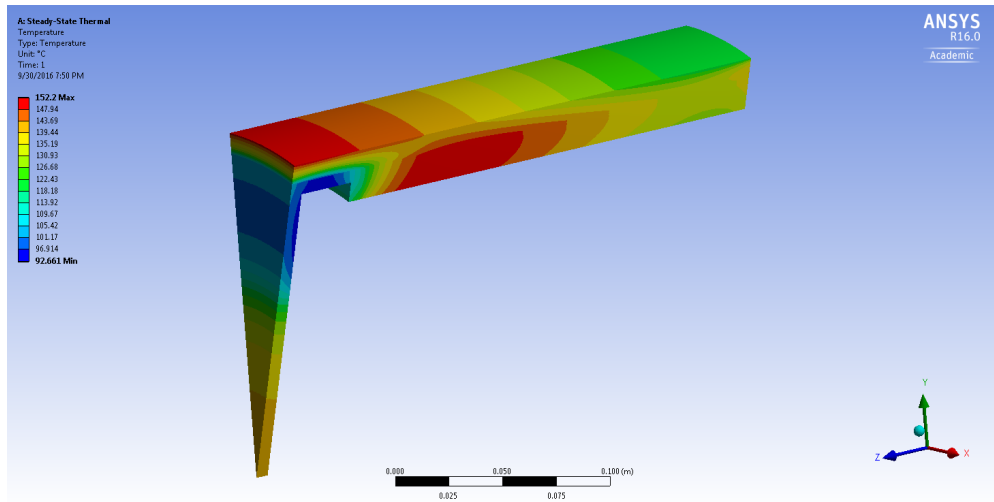
Figure 3.10: Rotor Temperature Distribution with Outlet Temperature at 86 °C

The machine hotspot temperature is 182 °C occurred at the outlet end-winding region because of temperature rise of the air flow mass and limited convection effects. The air flow mass is assumed to absorb all stator heat, including copper loss, iron loss and gap windage loss. And ambient temperature along the active region varies linearly from inlet to outlet air temperature. The rotor hotspot temperature is around 155 °C at the retaining ring and magnet. The magnet is heated up by viscosity of air in the gap of rotating concentric cylinders.
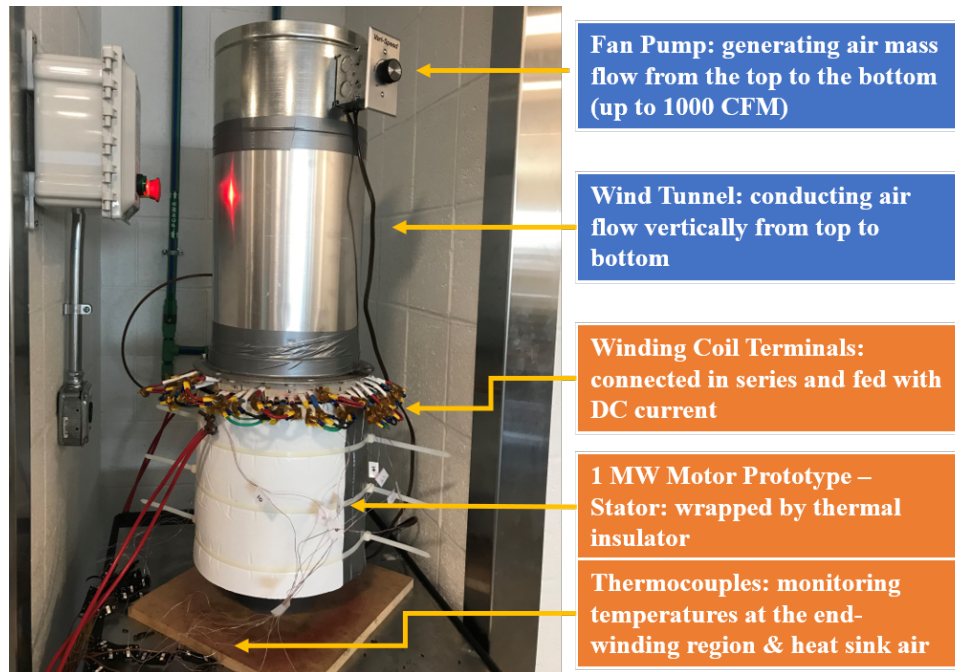
Figure 3.11: Stator Thermal Model Validation Setup
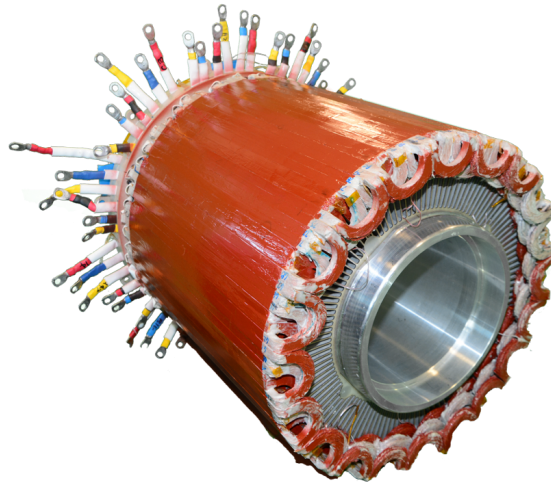
Figure 3.12: MW High-Specific-Power High-Frequency Motor - Stator with Sixty Sets of Form-Wound Windings Using AWG 38 Litz Wires

3.5 Stator Thermal Experiment

The stator thermal experiment is to validate the thermal resistance and cooling channel heat transfer effects with accurately controlled heat source and cooling flow rate. It is necessary to verify stator thermal performance before the MW full-scale motor test. This stator thermal

calibration process can lower overheating risks and uncertainties in the motor final test.

3.5.1   Hardware Setup Description

The stator thermal validation test consists of the MW stator prototype, pumping fan, wind tunnel, dc power supply and thermal data acquisition instrument. The hardware setup is shown in Figure 3.11. The stator is mounted vertically on a plastic holder. There is a 1.5-foot tube between the pumping fan and the stator. It behaves as a wind tunnel to conduct the fan cooling flow from the top air to the bottom of the stator. The pumping fan is a TerraBloom 10" Inline Duct Fan with a maximum flow rate up of 1065 CFM.

The stator has 30 sets of form-wound windings with 60 terminals in total, as presented in Figure 3.12. The winding-terminal side has a shaft mounting plate used for the horizontal attachment to a solid wall in the full-scale test. The cooling air flows into the winding-terminal side first, and then through the heat sink before exiting at the stator free-end side. AWG 10 wire and screw-type connectors are used to connect all 30 sets of windings in series. The metal connectors were wrapped with Teflon insulation in case of short-circuit or ground fault. During the stator development, rigorous partial discharge and hi-pot tests were conducted on all winding sets and the stator prototype to ensure no insulation breakdown. The stator windings are connected in series with a separate 500 W 70A dc power supply. Due to the power supply rating limit, the maximum current is 50 A, which is approximately half of the rated current 93 Arms. In the thermal validation test, only the stator windings have the heat load. To ensure all the heat flux flows radially towards the heat sink, there is a thermal insulator wrapped around the stator, as shown in Figure 3.11.

There are 16 thermocouples mounted on the stator separated into two groups. One group is targeted for winding. There are 12 thermocouples inserted at the phase-A,B,C end-winding regions. It is unrealistic to mount thermocouples at the active region of the stator, since there is no free space for the thermocouple wires and partial discharge could occur between the thermocouple metal pin and form-wound windings. Thus, the end-winding is the accessible location for thermocouple installation. The winding-region thermocouples pin is insulated with Teflon to avoid winding insulation failure. Strong epoxy resin is applied to mount
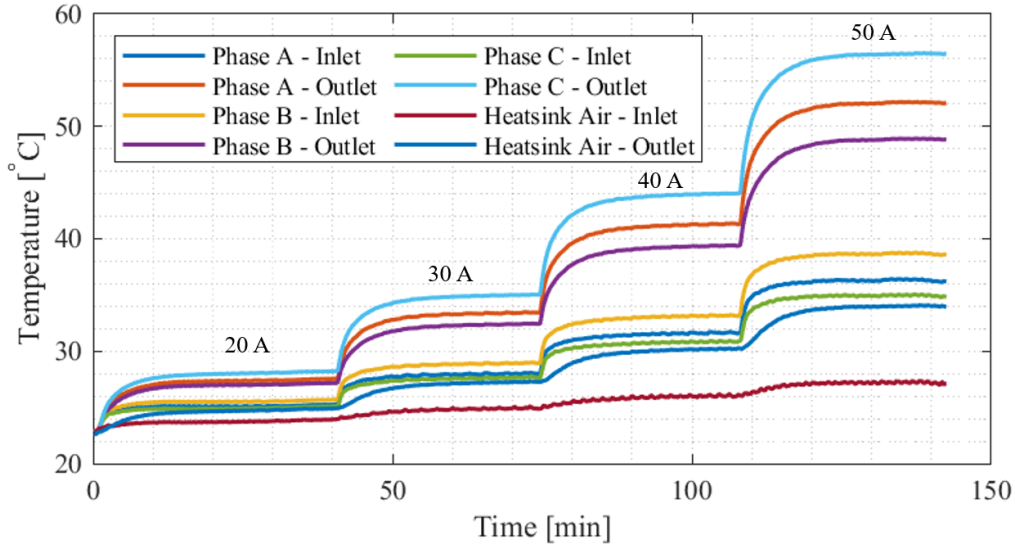
Figure 3.13: Real-Time Temperature Profile of the Stator Prototype

thermocouples to the windings. The other group is to measure the air temperature within the heat sink. In this group, thermocouples are not insulated. The thermocouple pin is floating in the air to measure the cooling air flow temperature within the heat sink. No contact exists between the thermocouple pin and the heat sink surface. All of the thermocouples are distributed uniformly along the stator tangential direction and axial direction (both at the cooling air inlet and outlet region). Redundant thermocouples are required for unexpected broken cases and to cross check thermal measurements.

3.5.2 Validation Results

The stator thermal test was taken when the coolant flow reached the maximum capability of the pumping fan. The measured axial flow speed near the outlet opening ending is around 5.8 m/s. Another indirect way to measure the flow speed within the heat sink to back-calculate the mass flow rate according to the air temperature rise across the heat sink and the total stator loss. The stator loss was measured at the DC power supply output voltage and current. And the air temperature rise across the heat sink was measured through the pre-installed thermal couples.
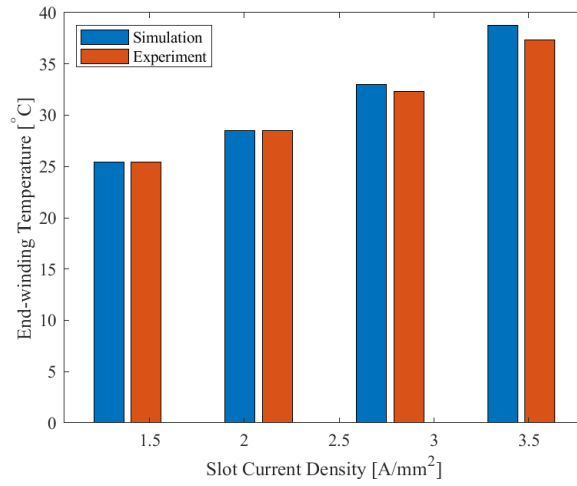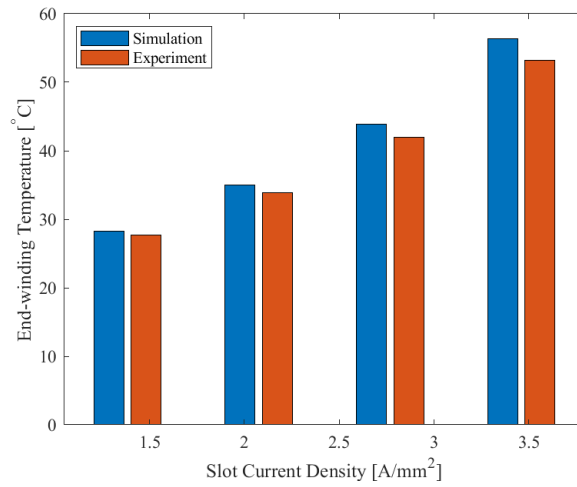
Figure 3.14: Prediction and Experimental Temperature Comparison at (a) Inlet and (b) Outlet

The DC power supply varies the input current through each coil on the stator from 20 to 50 A. The temperature profile is plotted in Figure 3.13. Each current measurement takes around 30–40 minutes to allow the temperature to fully reach steady state. There are temperature differences among phase A,B,C form-wound windings due to various ending axial lengths. Since there is no cooling effect on the stator outer surface, ending-winding regions have less cooling effect compared with motor rotation. The temperature difference among phases could be enlarged in this case.

Table 3.3: Comparisons of Analytical, Simulation, and Experimental Results

Axial Flow Speed = 6.1 m/s					
Current	Experiment	Analytical		Simulation	
[A]	Temp [°C]	Temp [°C]	Error %	Temp [°C]	Error %
20	27.71	27.8	0.33%	28.30	2.14%
30	33.82	33.9	0.23%	35.03	3.58%
40	41.98	41.45	1.26%	43.87	4.50%
50	53.16	52.34	1.54%	56.33	5.97%
Axial Flow Speed = 5.2 m/s					
Current	Experiment	Analytical		Simulation	
[A]	Temp [°C]	Temp [°C]	Error %	Temp [°C]	Error %
20	29.03	29.20	0.60%	29.27	0.85%
30	35.70	35.70	0.01%	36.25	1.52%
40	44.85	44.38	1.04%	46.06	2.69%
50	56.91	55.75	2.03%	58.87	3.46%
Axial Flow Speed = 3.8 m/s					
Current	Experiment	Analytical		Simulation	
[A]	Temp [°C]	Temp [°C]	Error %	Temp [°C]	Error %
20	27.86	28.13	0.97%	28.33	1.67%
30	35.12	35.20	0.23%	35.54	1.21%
40	45.47	45.10	0.82%	46.08	1.33%
50	59.38	58.50	1.48%	61.71	3.93%

Figures 3.14a and 3.14b present the comparisons between the simulation and experimental temperatures of the stator up to 50% of rated slot current density (7 A/mm^2). Note that the temperatures of the simulation and experiments are the average values of thermocouples at phase A,B,C. Both inlet and outlet predictions have good agreement with experimental results. The result demonstrates that the simulation model captures the stator thermal resistance and heat transfer at the heat sink.

Table 3.3 summarizes the experimental, analytical, and simulation data with various currents and axial flow speeds. The current here is the measured value of the dc power supply. Higher current creates larger temperature gradient across the stator leading to lower thermocouple errors. Both analytical and simulation results agree well with experimental results. Note that simulation predicts higher temperature because the boundary condition prediction

of the end-winding region is conservative. The flow speed varies from 3.8 m/s to 6.1 m/s. The flow speed is measured at the air flow exit location outside the cooling channels. It is also cross-checked with the calculation value based on the total winding loss and the air flow temperature rise across the heat sink. The different air flow speeds cause variations in outlet air temperate and convection boundary coefficients at the heat sink.

CHAPTER 4

LITZ WIRE EFFECTIVE THERMAL CONDUCTIVITY

The thermal design of stator windings controls electric loading and impacts torque/power density of electrical machines allowing lower emissions in electrification of vehicles and airplanes [46], [47]. Litz wire is selected for the windings since it reduces eddy-current loss with its small conductor size and transposition arrangement [48], [49]. However, because various insulation layers (of strands, bundles and turns) and potting materials are required to eliminate voltage breakdown, the windings become complex composite, making prediction of their effective thermal conductivity challenging.

Most winding-equivalent-thermal-conductivity analytical studies focus on strands and bundles in a parallel arrangement. A detailed 2-D time-consuming finite-element analysis (FEA) can be conducted for accurate prediction [47], [50], [51]. For fast estimation, homogenization techniques are applied to regroup copper, insulation and resin areas [52], [53], [54]. A more rigorous analytical approach uses the multi-scales method to account for wire shape and distribution spacing effect [55]. The parallel arrangement prediction method cannot be used for litz wire directly, because it neglects the heat dissipation benefits of the transposition arrangement in litz wire. Few papers consider transposition effects in litz wire. Litz wire equivalent thermal conductivity by assuming strands and bundles in parallel is studied [53]. A thermal equivalent circuit of litz wire is presented, considering transposed effects without an analytical solution for the presented thermal equivalent circuit [56]. To the best of the authors' knowledge, there is no published literature quantifying transposition effects on litz wire thermal conductivity.

This chapter takes up two challenges: developing an analytical model to predict the equivalent thermal conductivity of form-wound windings with litz wire including transposition effects, and comparing transposed and parallel arrangement effects on litz wire heat dissipa-

| (a) Staggered Winding | (b) Selected Rectangular Transposed Litz Wire | (c) Strands and Bundles within Litz Wire(Credit: NASA Glenn Research Center) |

Figure 4.1: Form-Wound Winding and AWG 38 Litz Wire

tion. The proposed analytical model has advantages of less computational time and excellent accuracy compared to the FEA method. Six samples of two different litz wire types validate the accuracy. The transposed and parallel arrangement comparison study indicates that the litz wire transposition has enhanced heat dissipation of 10% to 30%. This advantage could play a critical role in high-power-density, and high-efficiency electrical machine design. Therefore, the transposition effects of litz wire heat dissipation performance should be studied in more detail.

4.1 Transposed Litz Wire Geometry and Materials

Two types of rectangular litz wire are selected. The strand size and wire arrangements are designed and given by New England Company to minimize induced current loss while maintaining high fill factor and electric loading. Epoxy resin is employed to firmly bundle litz wires in specifically designed slot geometries shown in Figure 4.1a. The first is an AWG 38 litz wire used in a high-frequency, high-specific MW-level slotless machine [9]. It consists of 660 AWG 38 strands separated into 15 bundles as shown in Figure 4.1b. This maintains a rectangular shape of 6.2 mm by 1.6 mm with a bundle transposition angle ($\theta = 28.5°$). Each strand surface is brushed with heavy polyimide coating. Forty-four strands form a bundle wrapped with polyimide insulation, which limits the allowable maximum temperature in the machine. The associated configurations and thermal conductivity properties are presented

in Table 4.1. The second type of litz wire is AWG 30. It consists of seven bundles with seven AWG 30 strands in each bundle, as listed in Table 4.2. In this type, there is only heavy-duty strand insulation. The AWG 30 litz wire also maintains a rectangular shape of 3.1 mm by 1.6 mm with a bundle transposition angle ($\theta = 16.9°$). Both types are studied in detail. Analytical, simulated, and experimental results will be presented and discussed in Sections 4.3 and 4.4. Section 4.2 uses the AWG 38 litz wire as an example to show the calculation process.

Table 4.1: AWG 38 Liz Wire Configuration and Winding Material Thermal Properties [57]

	Type	Thickness(mm)	Max Temp(°C)	Thermal Cond.(W/mK)
Strand	Polyimide	0.013	240	0.1
Bundle	Nomex	0.127	220	0.1
Resin	Duraco 128		260	1.7

Table 4.2: AWG 30 Liz Wire Configuration and Winding Material Thermal Properties [57]

	Type	Thickness(mm)	Max Temp(°C)	Thermal Cond.(W/mK)
Strand	Polyimide	0.025	240	0.1
Resin	Duraco 128		260	1.7

4.2 Equivalent Thermal Conductivity Analytical Modeling

The section focuses on finding equivalent thermal conductivity across the rectangular litz wire cured with epoxy resin, as shown in Figure 4.1a. A homogenization technique within the bundles is applied first. Then the potted litz wire effective thermal conductivity is evaluated with an analytical model including transposition effects. Both general and simplified models are derived.

4.2.1 Homogenization within Bundles

A homogenization technique is applied within bundles to find their effective thermal conductivity, since each bundle of the selected litz wire contains numerous small strands, strand /bundle insulation, and resin shown in Figure 4.1c. It is necessary to find the strand effective thermal conductivity before the bundle equivalent thermal conductivity evaluation. Since the pitch length of the strand transposition arrangement is usually at least 10 times larger than the bundle diameter and the related spatial variations are not large, homogenization techniques can be applied to find the strand and bundle effective thermal conductivity assuming strand parallel arrangement. In the selected litz wires, strands have a circular shape coated with a heavy-duty insulation layer. For the calculation simplification under the cartesian coordinate, the circle is treated as a square and the corresponding strand effective thermal conductivity evaluation equations are given as:

$$k_{s,II} = (r_s + t_s) \cdot \left(\frac{r_s}{k_{cu}} + \frac{t_s}{k_{ins}} \right)^{-1} \tag{4.1}$$

$$k_{strand,r} = \frac{2k_{ins}t_s + k_{s,II}}{2(t_s + r_s)} \tag{4.2}$$

where r_s and t_s are the strand radius and insulation thickness, k_{cu} and k_{ins} are the copper and insulation thermal conductivity.

The next step is to evaluate the bundle effective thermal conductivity. According to [54], the bundle equivalent thermal conductivity along the radial (transverse) direction can be evaluated by

$$k_{bundle,r} = k_{res} \frac{(1 + ff)k_{strand,r} + (1 - ff)k_{res}}{(1 - ff)k_{strand,r} + (1 + ff)k_{res}} \tag{4.3}$$

where k_{res} and $k_{strand,r}$ are thermal conductivity of the filled resin and strand along the radial (transverse) direction, ff is the fill factor of conductor within bundles. If bundle has a bundle insulation layer, Equation (4.3) needs to be fed into Equations (4.1) and (4.2) to get correction including the bundle insulation thermal effects.

4.2.2 Homogenization within Litz Wire Considering Transposition Effects

The selected litz wire consists of two layers of bundles. These two layers of bundles are transposed to form a rectangular wire shape with a transposition angle of θ, 23.78 degrees. The detailed geometry model is presented in Figure 4.2. There are two heat flow paths of each bundle included in the proposed analytical model, as shown in Figure 4.3. One is along the radial (transverse) bundle direction. The other one is the axial (parallel) bundle direction. Both paths extract the heat out of litz wire.
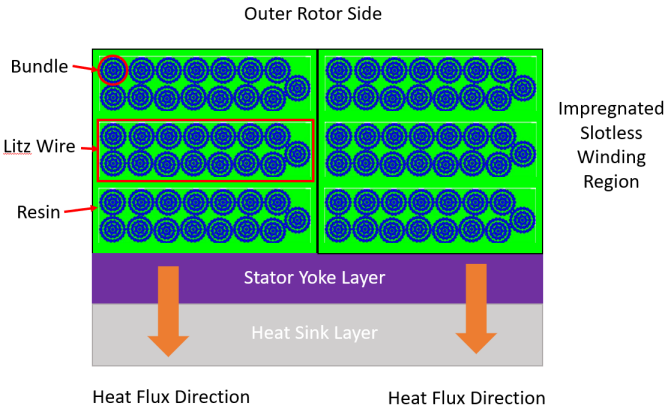
Figure 4.2: Stator Structure Illustration with Impregnated Slotless Windings of AWG 38 Litz Wire
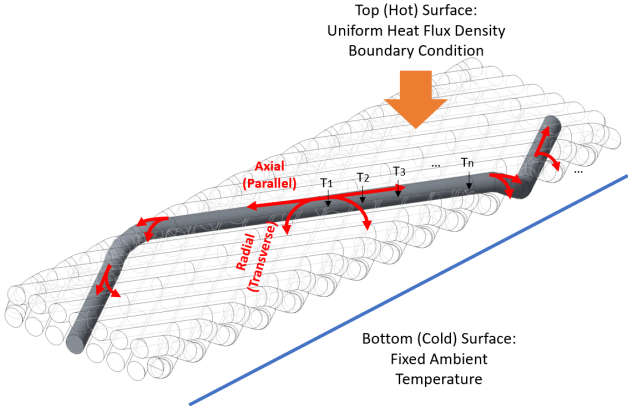
Figure 4.3: One-Pitch Litz Wire - Single Bundle with Heat Path Flow Arrows in Radial and Axial Directions
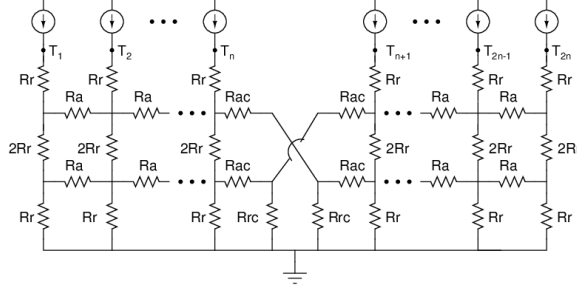
Figure 4.4: General Thermal Equivalent Circuit of the Selected Bundle within Half Pitch
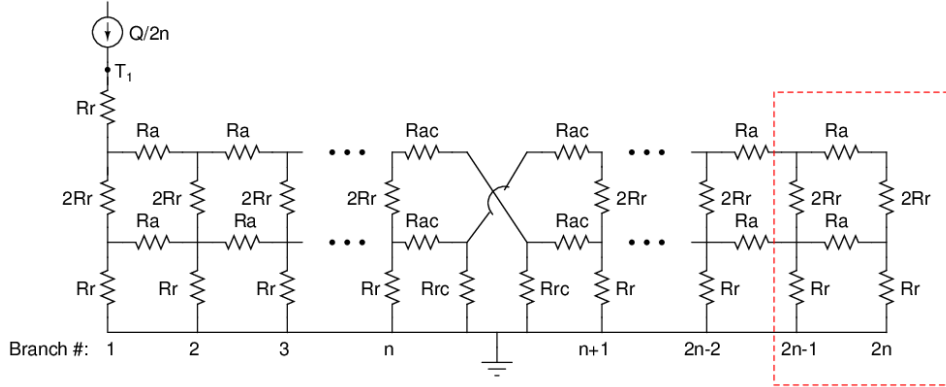
Figure 4.5: General Thermal Equivalent Circuit Seen at the Node Point T_1

Generalized Model

The proposed analytical model focuses on two symmetrical bundles within a potted litz wire. These two bundles are decomposed into small lumped components, including both radial and axial thermal resistances. And these two bundles are interleaved with each other to form a meshed lumped equivalent circuit, as shown in Figure 4.4. Heat source is modeled as current source and injected on the bundle top surface. The temperature gradient across the litz wire can be solved by the proposed thermal lumped equivalent circuit. The temperature rises of each node T_1–T_2n are not the same, although uniform heat flux is applied on the bundle top surface. This is due to non-uniform thermal conductivity.

The modeled litz wire section is decomposed into four and $2n$ layers along the radial and axial directions, respectively. R_{ac} and R_{rc} are the lumped thermal resistance of the curved part. The radial and axial thermal resistances in the equivalent circuit of Figures 4.4 and

44

4.5 are derived as:

$$R_r = \frac{n \cdot H}{W(L \sec\theta - 2H \csc\theta)} \frac{k_f}{k_{b,r}} \frac{(1+ff)k_{b,r} + (1-ff)k_f}{(1-ff)k_{b,r} + (1+ff)k_f} \tag{4.4}$$

$$R_a = \frac{L \sec\theta - 2H \csc\theta}{n \cdot W H k_{b,a} \cdot ff} \tag{4.5}$$

$$R_{rc} = \frac{\cos\theta}{W} \frac{k_f}{k_{b,r}} \frac{(1+ff)k_{b,r} + (1-ff)k_f}{(1-ff)k_{b,r} + (1+ff)k_f} \tag{4.6}$$

$$R_{ac} = \frac{\csc\theta}{W k_{b,a} \cdot ff} + R_a \tag{4.7}$$

where ff is the bundle fill factor, L, H, W are the litz wire half-pitch rectangular dimensions, $k_{b,r}$ and $k_{b,a}$ are the radial and axial bundle equivalent thermal conductivities, and θ is the bundle transposed angle.

The proposed lumped mesh circuit model can be solved via an iterative method. The solution target is to find the equivalent resistance associated with each current source by eliminating mesh intersection nodes. Such an elimination process starts from the edge of the circuit and propagates toward the source-associated branch.

Suppose T_1 is the unknown, as shown in Figure 4.5. Only the heat source at branch #1 is active, and other heat sources are open according to an superposition principle. The circuit simplification starts from the branch $2n$ and $2n-1$. There are two Y-delta transformations of branch #2n. A similar transformation process can be applied to each branch iteratively.
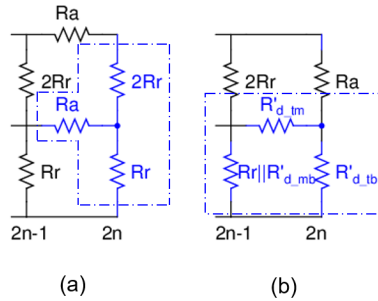
Figure 4.6: The First Circuit Transformation within Branch #2n-1 and #2n

The first step of the transformation is illustrated in Figure 4.6. Basically, the intersection point highlighted with blue is the elimination target. The associated resistances are given

as:

$$R_t = 2R_r, \quad R_m = R_a, \quad R_b = R_r; \tag{4.8}$$

$$R'_{d\_tm} = \frac{R_t R_m + R_m R_b + R_t R_b}{R_b} \tag{4.9}$$

$$R'_{d\_mb} = \frac{R_t R_m + R_m R_b + R_t R_b}{R_t} \tag{4.10}$$

$$R'_{d\_tb} = \frac{R_t R_m + R_m R_b + R_t R_b}{R_m} \tag{4.11}$$

where t denotes top, m denotes middle, and b denotes bottom.
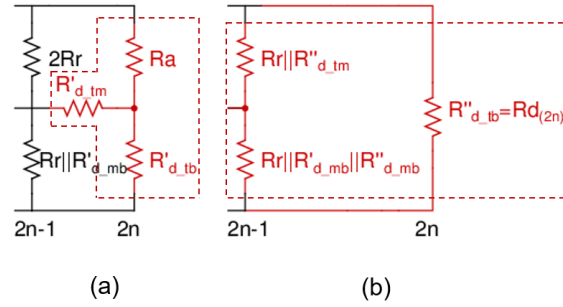
Figure 4.7: The Second Circuit Transformation within Branch #2n-1 and #2n

Then, the second step is to remove the highlighted red intersection point in Figure 4.7. The first transformation results need to be grouped into the branch $2n - 1$ and changed as Figure 4.7b. The associated resistances of the second transformation can be obtained as:

$$R''_{d\_tm} = \frac{R_a R'_{d\_tm} + R_a R'_{d\_tb} + R'_{d\_tm} R'_{d\_tb}}{R'_{d\_tb}} \tag{4.12}$$

$$R''_{d\_mb} = \frac{R_a R'_{d\_tm} + R_a R'_{d\_tb} + R'_{d\_tm} R'_{d\_tb}}{R_a} \tag{4.13}$$

$$R''_{d\_tb} = \frac{R_a R'_{d\_tm} + R_a R'_{d\_tb} + R'_{d\_tm} R'_{d\_tb}}{R'_{d\_tm}} \tag{4.14}$$

$$R_{d(2n)} = R''_{d\_tb} \tag{4.15}$$

After the above two Y-delta transformations, the branch n has one resistor $R_{d(2n)}$ in parallel with other branches, as shown in Figure 4.8d. And the branch $2n - 1$ results into the same circuit structure, as shown in Figure 4.6a. The exact calculation process can be
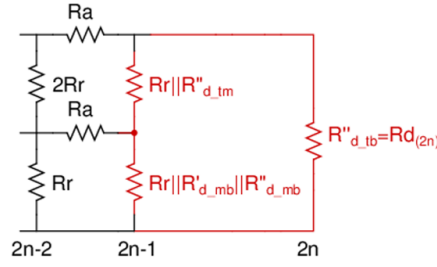
Figure 4.8: The Final Transformation of Branch #2n-1 and #2n

conducted through the branch $\#2n - 2$ and $\#2n - 1$ with Equations (4.7)-(4.14). The only change in this process is to update R_t, R_m, and R_b with the updated resistor values given as:

$$R_t = R_r || R''_{d\_tm}, \quad R_m = R_a, \quad R_b = R_r || R'_{d\_mb} || R''_{d\_mb};$$ (4.16)

An iterative method can be used to calculate equivalent resistor in each branch following the above transformation procedure. After transforming all of the branches from $2n$ to 1, there will be only one equivalent resistance associated with each branch. That means there are $2n$ parallel resistors resulting from the mesh intersection elimination process. Then, the total equivalent resistance and temperature of the current source #1 become

$$R_{eq,1} = R_r + R_{d(1)}^{(1)} || R_{d(2)} || \cdots || R_{d(2n)} \quad T_1 = R_{eq,1} \cdot Q/2n$$ (4.17)

The equivalent thermal resistance at branch #2 can be solved by similar principles. And most of the lumped resistances in (4.7) can be reused except $R_{d(2)}^{(2)}$, which needs to be evaluated separately. The total equivalent resistance and temperature of the current source #2 become

$$R_{eq,2} = R_r + R_{d(2n)} || R_{d(2)}^{(2)} || R_{d(3)} || \cdots || R_{d(2n)} \quad T_2 = R_{eq,2} \cdot Q/2n$$ (4.18)

The general equivalent thermal resistance and temperature seen from the heat source of

47

branch i become

$$R_{eq,i} = R_r + R_{d(2n)}||R_{d(2n-1)}||\cdots||R_{d(2n-i+1)}||R_{d(i)}^{(i)}||R_{d(i+1)}||\cdots||R_{d(2n)}T_i = R_{eq,i} \cdot Q/2n \tag{4.19}$$

With the equivalent thermal resistance and temperature at each heat source, the average equivalent thermal resistance and temperature of the winding block surface are

$$R_{eq,avg} = R_r + \frac{1}{n}\sum_{i=1}^{n} R_{eq,i} \quad T_{avg} = R_{eq,avg}Q/2n \tag{4.20}$$

The overall average equivalent thermal conductivity can be evaluated with average temperature rise, litz wire block dimensions, and heat flux.
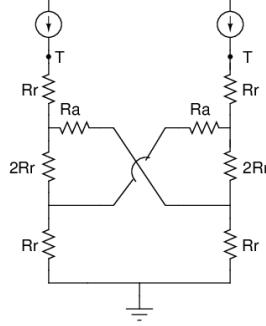
Figure 4.9: Simplified Thermal Equivalent Circuit of the Selected Bundle

Simplified Model

For a quick prediction of equivalent thermal conductivity, its associated thermal equivalent circuit can be simplified as $n = 1$. Also, the curvature portion is assumed not to conduct heat radially. Therefore, the corresponding lumped thermal resistance circuit is displayed in Figure 4.9. Only two element thermal resistances need to be evaluated here, R_a and R_r:

$$Ra = 2\left(\frac{L\sec\theta - 2H\csc\theta}{n \cdot WHk_{b,a} \cdot ff} + \frac{\csc\theta}{Wk_{b,a} \cdot ff}\right) \tag{4.21}$$

$$Rr = \frac{n \cdot H}{W(L\sec\theta - 2H\csc\theta)}\frac{k_f}{k_{b,r}}\frac{(1+ff)k_{b,r} + (1-ff)k_f}{(1-ff)k_{b,r} + (1+ff)k_f} \tag{4.22}$$

48

By applying a superposition principle and a circuit simplification technique, the total thermal equivalent resistance associated with one heat source is simplified as

$$R_{tot} = 2R_r \cdot \frac{(10R_r^2 + 11R_r R_a + 2R_a^2)}{2R_r^2 + 8R_r R_a + R_a^2} \tag{4.23}$$

And the equivalent thermal conductivity of the potted litz wire with transposition arrangement can be obtained from total resistance:

$$k_e = \frac{H}{W(L \sec \theta - 2H \csc \theta) R_{tot}} \tag{4.24}$$

This simplified model combined with bundle homogenization equations can be easily implemented in MATLAB and Excel.
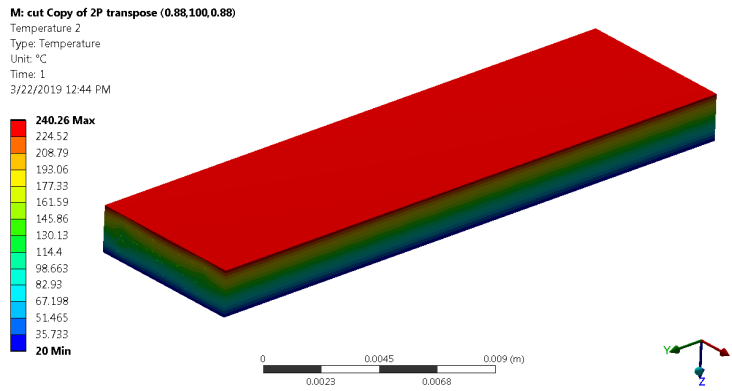
(a) Resin Block
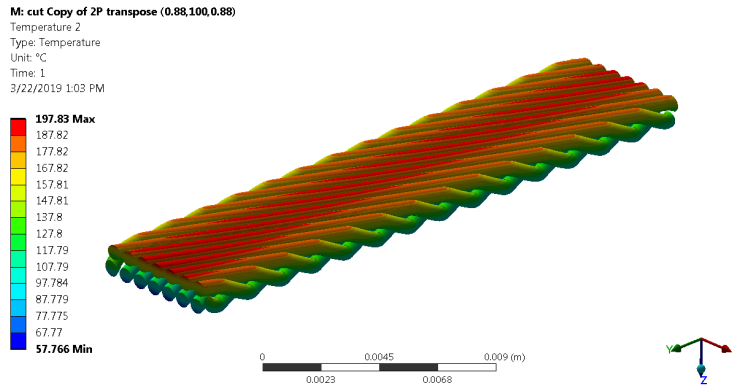
(b) Litz Wire

Figure 4.10: Simulation Results for the Transposed Arrangement ($k_{bundle,r} = 0.88$ W/mK, $k_{bundle,a} = 100$ W/mK, $k_{resin} = 0.8$ W/mK)

49

(a) Resin Block

(b) Litz Wire
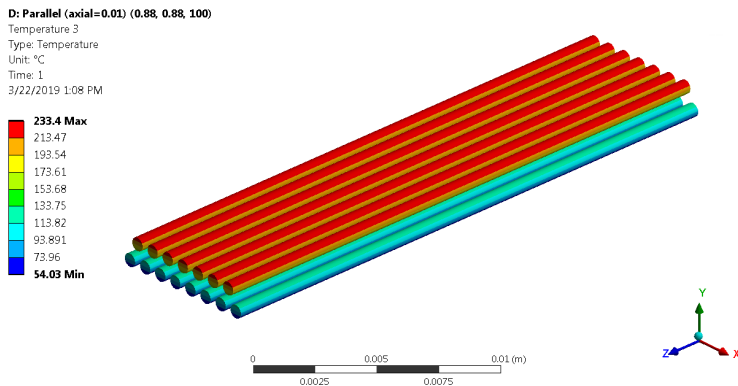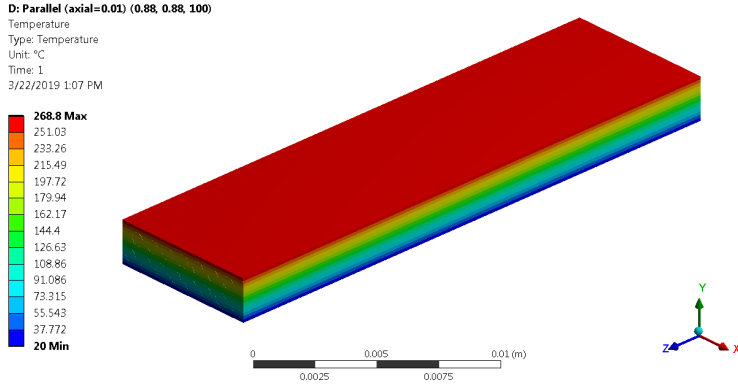
Figure 4.11: Simulation Results for the Parallel Arrangement ($k_{bundle,r} = 0.88$ W/mK, $k_{bundle,a} = 100$ W/mK, $k_{resin} = 0.8$ W/mK,)

4.3 Simulation Verification

This section presents two simulation studies. The first one uses detailed 3-D FEA models to compare the transposed and parallel effects on the litz wire heat dissipation performance. The second verifies the proposed analytical model with the FEA simulations. Both radial and axial bundle thermal conductivity are varied over a large range to confirm the proposed analytical model prediction accuracy.

4.3.1 Transposed vs. Parallel Arrangement

The 3-D models for the one-pitch AWG 38 litz wires with both transposed and parallel arrangements are simulated with steady-state thermal analysis in ANSYS. The bundles
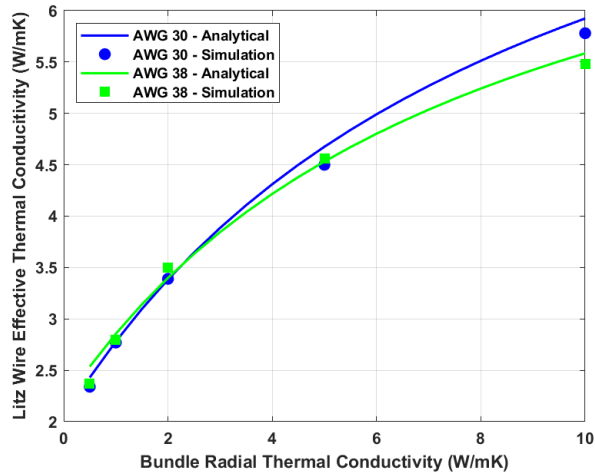
(a) Radial (Transverse)
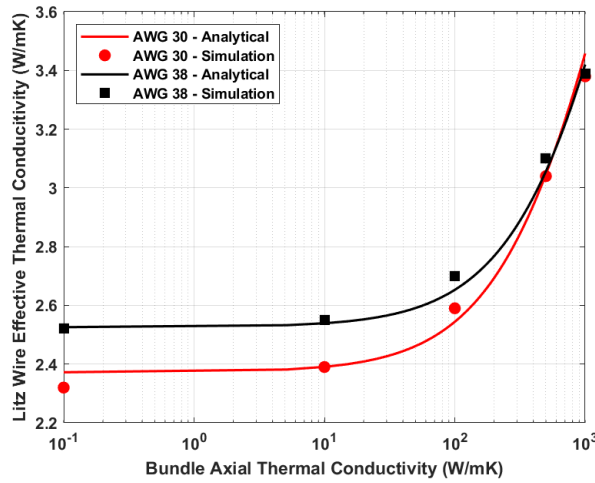
(b) Axial (Parallel)

Figure 4.12: Analytical Model Validation with Varying Bundle Thermal Conductivity

within the resin block are assigned radial and axial thermal properties and local coordinates. The bottom boundary condition of the resin block is a constant temperature of 20 °C. The upper boundary has a 50 W heat load applied. Other boundary surfaces are assigned perfect insulation. Both transposition and parallel simulations have the same boundary conditions. The resin and litz wire radial and axial bundle thermal conductivity are assigned specific values close to the real case in Section 4.1. The effective thermal conductivity of the modeled

block can be calculated via:

$$k_{block} = \phi_Q \frac{h}{Avg(T_{hot} - T_{amb})} = \frac{Q}{l \cdot w} \frac{h}{Avg(T_{hot} - T_{cold})} \tag{4.25}$$

where ϕ_Q is the average heat flux density across the modeled block, Q is the heat load imposed on the block model, l, w, and h are the dimensions of the block model, $Avg(T_{hot})$ is the average temperature of the hot surface, and T_{cold} is the cold surface temperature fixed at 20 °C.

Figures 4.10 and 4.11 are the temperature distribution contours of the transposed and parallel litz wires, respectively. It is interesting to notice that the temperature rise in the transposed case is lower than in the parallel case, although both bundles have high thermal conductivity (100 W/mK) on the axial (parallel) direction. According to the temperature distribution of the potted wire blocks in Figures 4.10a and 4.11a, the hotspot temperature is around 10.5% lower in the transposition than the parallel. The maximum temperature of the transposition wire is 15.5% lower than in the parallel, as shown in Figures 4.10b and 4.11b. According to (4.25), the effective thermal conductivity of the litz wire block with transposition arrangement is 1.31 W/mK, which is around 15.9 % higher than the thermal conductivity of the parallel arrangement one, as shown in Figures 4.10 and 4.11. Thus, the heat dissipation benefits of using transposition arrangement should be accounted for in a litz wire equivalent thermal conductivity evaluation.

4.3.2 Theory and Simulation Prediction Comparison

The effective thermal conductivity of the transposed AWG 38 and 30 litz wires is evaluated using the equations in Section 4.2. The prediction results are compared with detailed 3-D FEA simulations. The boundary conditions, litz wire geometry, and material properties are the same in both the theoretical and simulation setups, except for the resin thermal conductivity changing from 0.88 W/mK to 4 W/mK in this section. The theoretical and simulation prediction results are compared by varying both the radial and axial bundle thermal conductivity in a wide range to capture the transposition effects on litz wire heat

dissipation capability.

Although the heat flux boundary condition is uniform, the temperature distribution across the litz wire is not. Copper and insulation distributions are inconsistent along the x,y,z directions in the transposed wire. Figure 4.12a presents both theoretical and simulation results while varying the radial (transverse) bundle thermal conductivity from 0.5 to 10 W/mK. The axial (parallel) thermal conductivity is fixed at 100 W/mK. Figure 4.12b shows the effective thermal conductivity of various axial bundle thermal conductivity values while keeping the radial bundle thermal conductivity at 0.8 W/mK. The variation of the axial bundle thermal conductivity is large, ranging from 0.1 to 1000 W/mK. Although the selected verification ranges of the bundle radial and axial thermal conductivity are outside of the feasible physical ranges, a larger verification range can better test the robustness of the proposed analytical model prediction accuracy. Both Figures 4.12a and 4.12b show that the theoretical results have good agreement with the simulation results in the large variations of radial and axial thermal properties. The prediction error using the proposed analytical method is ±6%.

Figures 4.12a and 4.12b also indicate paths to improve litz wire effective thermal conductivity. The first way is to adopt the transposed arrangement in the litz wire, because the extra heat dissipation path along with the axial (parallel) bundle direction of the litz wire can directly assist thermal management of the stator windings in a high-power-density electrical machine. In addition, the axial bundle thermal conductivity is usually 100 times greater than the radial bundle thermal conductivity, since wire heat does not penetrate through the many insulation layers along the bundle axial direction. Figure 4.12b indicates that the transposition arrangement can increase litz wire equivalent thermal conductivity from 10% to 30%, compared with the parallel arrangement where the axial bundle thermal conductivity is close to zero. When the axial bundle thermal conductivity is close to zero, the extra heat dissipation path along the bundle axial direction no longer works, which is exactly the same as in the parallel arrangement condition. The second way is to minimize insulation usage or to use high-thermal-conductivity insulation along the radial bundle direction where most of the winding heat flux flows. There is a trade-off between the stator winding insulation usage and heat dissipation capability.
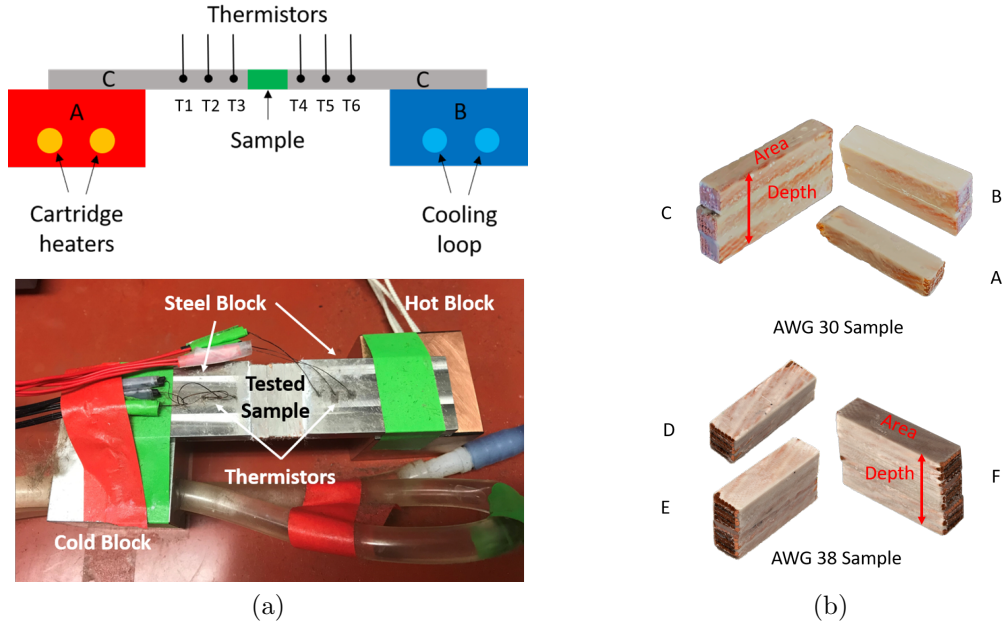
Figure 4.13: Litz Wire Thermal Conductivity Measurement Hardware Setup and Six Test Samples

It takes only 1-2 seconds to use the analytical model for predicting effective thermal conductivity in the MATLAB programming environment. The simulation model requires at least half an hour to complete the meshing and computational process. If the CAD model development is included, the simulation model requires days to months. Overall, the proposed analytical model, especially the simplified model, has advantages for modifying wire geometry and adequate accuracy while saving computation time.

4.4 Experimental Validation

This section presents an effective thermal conductivity measurement method and shows consistency between the predicted and the hardware validation results. Six samples of AWG 38 and 30 litz wires in Figure 4.13b are tested. The selected wire configurations, dimensions and properties are discussed in Section 4.1.

4.4.1 Hardware Setup

The equivalent thermal conductivity measurement setup was initially designed for measuring thermal switch properties [58]. It consists of cold and hot copper blocks, steel interface blocks, and a tested sample. The hot copper block is supplied with a consistent heat source generated by a dc power supply. The cold copper block is cooled by chilled water set at 0-10 °C. The two steel interface blocks are manufactured with the same dimensions and each is drilled with three thermistor holes. The sample litz wire block is inserted between the two steel blocks and covered with thermal paste to minimize the thermal contact resistance. Temperatures are measured with thermistors T1–T6 rather than with thermocouples, because thermistors give the more stable and accurate temperature measurements. The thermistor used in this setup is an LSMC series type with a diameter of 0.2″ and accuracy of ±0.2 °C. Small thermistors help reduce the temperature profile distortion in the steel blocks. Gaps of 5 mm separate T1–T3 and T4–T6, as shown in Figure 4.13a. Insulation foam wrapped around the setup minimizes the heat flux leaking from the thermal conduction process.

Six litz wire samples A–F of Fig. 4.13b are tested, and their dimensions are specified in Table 4.3. All the samples have the same length of 25 mm with an ±0.5 mm error, which are larger than and close to the pitch lengths of AWG 30 (20.4 mm) and 38 (26 mm) respectively. The impregnated winding material samples are manufactured in the same way as the potted slotless windings, as detailed in [9]. A sufficient amount of epoxy resin is applied among the gaps of stacked samples, and then clamps are used to group the stacked samples together during the curing process which takes at least 24 hours. Since the same winding manufacturing procedures are carried out here, the contact resistance between the stacked samples can be ignored. Also, some efforts are made to minimize the contact resistance between the tested sample and the steel blocks. Careful surface sanding and cleaning with acetone in an ultrasonic bath ensure the smooth contact surfaces of the tested samples. The following section will discuss how to process the measurement data and eliminate the contact resistance effects to obtain the sample effective thermal conductivity.
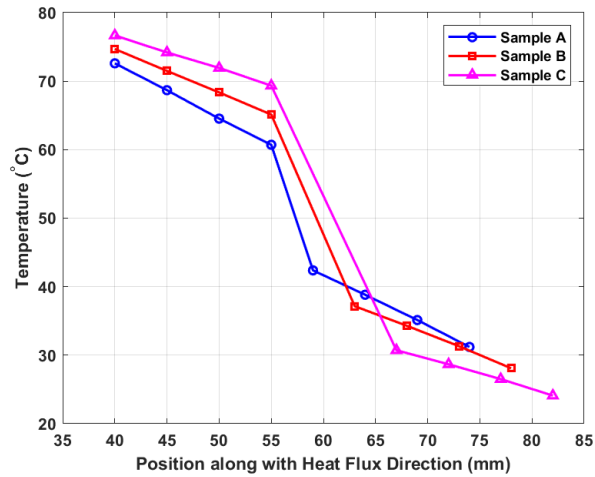
(a) AWG 30
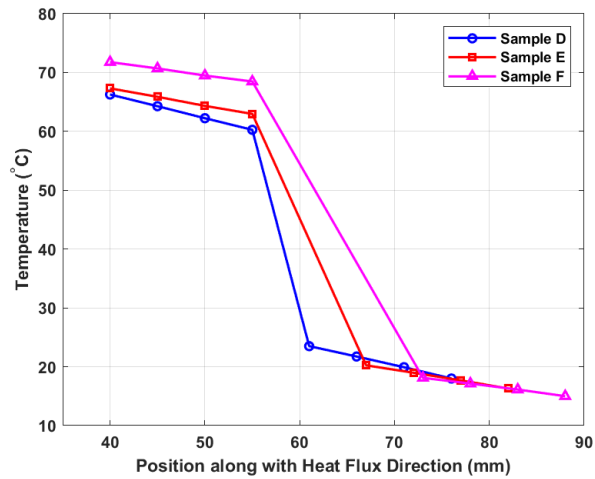
(b) AWG 38

Figure 4.14: Temperature Distribution across the Hot Plate, Sample, and Cold Plate

4.4.2 Experimental Data Analysis and Discussion

Six temperature measurements located at T1–T6 shown in Figure 4.13a are used to find the heat flux and temperature gradient across the tested sample in order to characterize the sample equivalent thermal conductivity. The inlet heat flux on the hot steel block needs to be evaluated first via a second-order upwind method. A similar principle can be applied to calculate the outlet heat flux on the cold steel plate. The formulation for measuring the

input and output heat flux (Q_{in} and Q_{out}) flowing through the sample is:

$$Q_{in} = \frac{k_{ss}lw}{2h} \cdot (3T_1 - 4T_2 + T_3) \tag{4.26}$$

$$Q_{out} = \frac{k_{ss}lw}{2h} \cdot (3T_4 - 4T_5 + T_6) \tag{4.27}$$

where k_{ss} is the steel block thermal conductivity, l and w are the dimensions of the sample block cross section, and h is the 5 mm gaps among T1–T6. Given the input and output heat flux through the sample, the hot and cold side temperatures of the tested sample can be then obtained by:

$$T_{hot} = T_3 - \frac{Q_{in}h}{k_{ss}lw} \tag{4.28}$$

$$T_{cold} = T_4 + \frac{Q_{out}h}{k_{ss}lw} \tag{4.29}$$

More than two samples with various thickness are needed to compute sample and contact resistance. It is assumed that each sample has the same contact resistance. The temperature difference across the tested sample (dT) is defined as:

$$dT = T_{hot} - T_{cold} \tag{4.30}$$

And the sample and contact resistance are given as:

$$R_{sample} = \frac{2dT}{Q_{in} + Q_{out}} - 2R_{contact} \tag{4.31}$$

Table 4.3: Experimental Data of the Six Samples

#	AWG	θ [deg]	Depth [mm]	Area [mm^2]	Qin [W]	Qout [W]	dT [°C]
A	30	16.9	3.97	5.28x25	1.53	1.43	18.33
B	30	16.9	7.85	5.3x24.8	1.29	1.15	27.97
C	30	16.9	12.17	5.2x23.5	1.03	0.92	38.62
D	38	28.5	5.6	6.8x25.5	1.08	0.97	36.77
E	38	28.5	11.45	6.8x25.5	0.75	0.69	42.73
F	38	28.5	17.3	6.8x25.6	0.55	0.54	50.37

Table 4.4: Validation Comparison of the Six Samples

#	AWG	Rsample [K/W]	Rcontact [K/W]	Kexp [W/mK]	Kanal [W/mK]	Error	Ksim [W/mK]	Error
A	30	11.66						
B	30	22.18	0.38	2.6	2.44	6.56%	2.51	3.5%
C	30	38.54						
D	38	28.83						
E	38	51.92	3.54	1.2	1.29	6.98%	1.34	11.2%
F	38	85.45						

Temperature measurements are collected at steady state where the temperature difference stays within 0.1 °C. The temperature distributions of the six tested samples are plotted in Figures 4.14a and 4.14b. According to the measured temperatures, the inlet, outlet heat flux and sample thermal resistance can be evaluated by using Equations (4.25)-(4.29). The related results are summarized in Tables 4.3 and 4.4. For all the sample tests, the associated heat flux and temperature gradient are maximized with the heating power set at 10–15 W. The inlet and outlet heat flux measured vary by $\pm 9\%$. The sample thermal conductivity analytical values have $\pm 7\%$ error compared to the average experimental results.

CHAPTER 5

ELECTRO-THERMAL ANALYSIS AND OPTIMIZATION DESIGN OF SLOTLESS LITZ-WIRE WINDING

A high-frequency slotless surface permanent magnet machine is often selected as high-power-density/high-specific-power motor topology to enable transportation electrification. Slotless topology eliminates the teeth yoke usage in conventional motor design to reduce motor weight and iron loss, and includes more copper volume to carry higher electric loading, as shown in Fig. 5.1. The high-frequency concept with thinner back yoke also contributes to more lightweight motor design, but incurs eddy-current-loss challenges, which can be resolved by using litz-wire windings.

<div align="center">(a)   (b)</div>
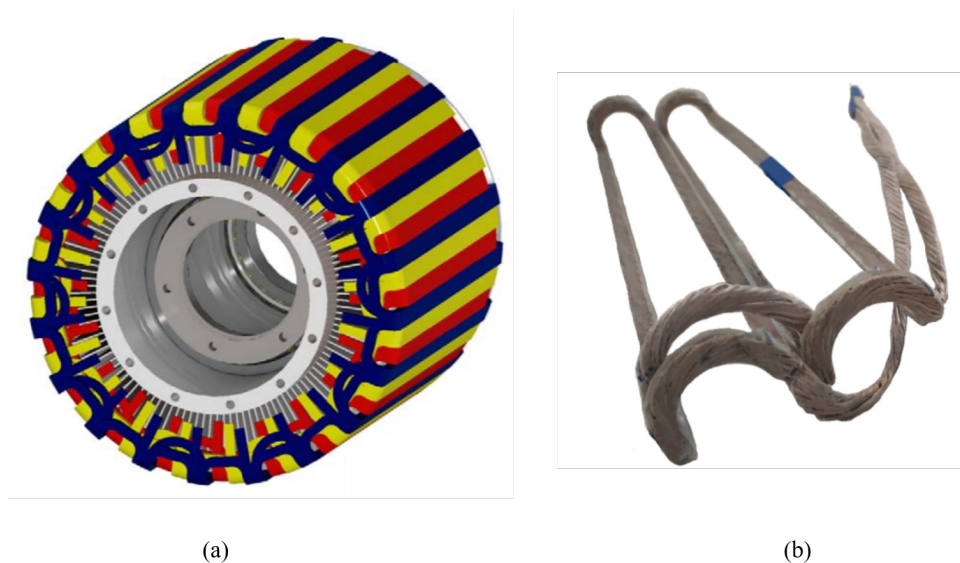
Figure 5.1: (a) MW High-Frequency Motor - Stator (b) Form-Wound Slotless Winding

Litz wire has been widely used in high-frequency magnetic components, such as trans-formers and inductors. A large amount of induced current loss can be generated at high frequency, especially in the air-core magnetic devices where high-flux-density magnetic field passes through conductors directly. With small conductor size, insulation layers, and trans-

position arrangements, litz wire is an effective solution to reduce induced current and lower eddy current losses. Therefore, litz wire is selected for high-frequency slotless windings.

Many efforts have been made to evaluate and minimize the ac losses of litz wire and slotless windings. Intensive research is conducted on the high-frequency transformers. The detailed ac loss analytical models of litz wire are shown in [59], [60], [61]. An optimal selection scheme of strand size on the basis of cost and loss is presented in [62]. For the form-wound winding study, [63] studies the proximity losses of litz-wire windings in high-speed brushless permanent magnet motors. [64] presents an AC resistance model of litz-wire windings in high-power generators. However, optimizing only the ac losses of slotless litz-wire windings is insufficient in high-specific-power/high-power-density high-frequency motor design.

Winding heat dissipation capability is also critical in determining motor specific power and should be included in the litz-wire winding design process, which most published works neglect. The trade-off among strand size, winding losses, and thermal conductivity of litz wire windings needs to be further investigated to improve motor torque density. Another interesting litz wire design factor, transposition angle, is usually neglected while it determines litz wire ac losses and equivalent thermal conductivity. In order to further advance motor torque density, electro-thermal design optimization of slotless litz-wire winding plays an important role.

This chapter develops an analytical electro-thermal model and optimization scheme of slotless litz-wire windings for high-frequency high-specific-power motors. The detailed winding losses including eddy-current and conduction losses, and thermal performance prediction models are proposed. The optimal strand size, transposition angle, and turn number in slotless litz-wire windings are found and discussed in this chapter.

5.1   Litz Wire and Slotless Winding Characterization

5.1.1   Form-wound Slotless Winding

Form-wound windings have electrical, thermal and mechanical benefits in high-speed motor applications. Using litz wire has been shown to reduce induced-current loss. The stator
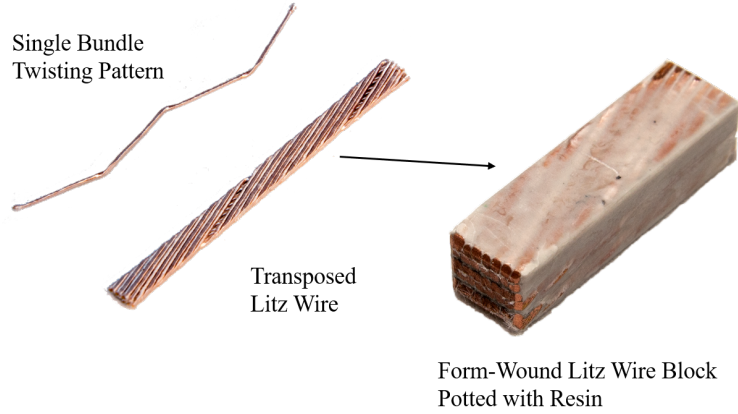
Figure 5.2: (a) Transposed Litz Wire (b) Potted Slotless Winding Block - Litz Wire Cross Section View

Table 5.1: Litz Wire Specifications of AWG 30–40 for a Rectangular Shape of 0.122" by 0.063"

AWG	Ds (mm)	Fill Factor	Ns	Nb	ns
30	0.255	0.501	98	14	7
31	0.227	0.513	126	18	7
32	0.202	0.507	156	12	13
33	0.18	0.5	195	15	13
34	0.16	0.501	247	19	13
35	0.143	0.489	302	15	20
36	0.127	0.486	380	19	20
37	0.113	0.486	480	15	32
38	0.101	0.489	616	14	44
39	0.09	0.476	748	17	44
40	0.08	0.474	936	12	78

Ns: total strand number
Nb: total bundle number
ns: strand number per bundle

winding of a MW high-frequency high-specific-power PM motor is selected for study and optimization in this chapter, since it has high current density and operates under the high-frequency magnetic field.

5.1.2 Litz Wire

The selected litz wire types include a strand range of AWG 30 to 40 and are provided by New England Wire Technologies. They have a rectangular shape of $0.122''$ by $0.063''$ and a fill factor range of 0.474 to 0.513 listed in Table 5.1. The previous electrical, thermal, and manufacturing design and validation results of the MW motor form-wound windings have been presented in [9], [10], [65]. The associated electrical and thermal physical properties are also included in the previous studies. Each litz wire consists of several bundles and each bundle consists of several strands with a consistent twisting pattern. As indicated in Figure 5.2, bundles also have a consistent transposition arrangement with a transposition angle of θ. The strand transposition effects are negligible since the strand transposition angle is extremely small, less than 2 degrees. However, the bundle transposition arrangement causes litz wire strands to have large spatial variations. The corresponding electrical and thermal effects of the bundle transposition angle will be discussed and optimized in the following sections.

5.2 AC and DC Loss Analysis

5.2.1 AC Loss Characterization

Minimizing ac losses is one of the challenges in high-frequency slotless winding design. It is necessary to review the ac losses of slotless litz-wire windings before analysis.

The ac losses of slotless windings are generated by the combination of conductor alternating current and rotating magnetic fields produced by rotor. The ac losses include the conductor skin-effect loss, the proximity loss induced by the alternating current of other nearby conductors and the external magnetic flux. The circulating current losses due to unbalanced voltage potential of parallel conductors can be ignored, since litz wire is well designed with transposition arrangement to average induced current effects. Figure 5.3 summarizes the skin and proximity effects by conductor alternating current and external magnetic field in both strand and bundle levels.
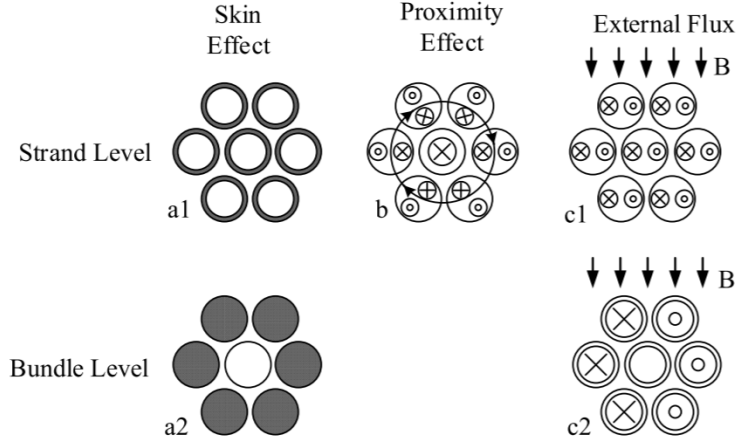
Figure 5.3: Types of AC Losses and Current Distributions in the Conductors of Armature Windings (a) Skin Effect Loses in Strand Level (b) Skin Effect Losses in Bundle Level (c) Eddy Current Losses in Strand Level (d) Eddy Current Losses in Bundle Level [59]

In bundle level, ac losses are usually much smaller than ac losses at the strand level, due to bundle transposition arrangement, bundle size, and higher resistivity. Skin effects within bundles are neglected in this chapter, because bundle diameter is 2–5 times strand diameter. However, proximity effects of external flux should be taken into account in slotless winding evaluation.

In strand level, skin effect and proximity effect losses of conductor alternating current can be ignored because of strand transposition arrangement and moderate operating electrical frequency range. The strand diameter is usually selected as less than twice the penetration depth to effectively suppress skin effect losses. Similar to the situation at the bundle level, the external field proximity effect loss needs to be further evaluated.

5.2.2   AC Loss Analysis

According to the previous discussion of ac loss mechanism, the litz wire ac losses are mainly caused by external flux proximity effects. Eddy current losses induced by the rotating air-gap magnetic flux are evaluated at both strand and bundle level. Many papers have presented analytical and simulation prediction methods of winding ac losses. Although simulation methods tend to use finite-element analysis to accurately calculate flux distribution and

conductor eddy current, it is not favored for slotless winding optimization procedure because of its time-consuming and complex prediction procedure. Thus, an analytical method is chosen to predict litz-wire ac losses to facilitate slotless winding design optimization.

Suppose the air gap magnetic flux is a perfect sinusoidal waveform. The strand eddy current loss is determined by the excitation frequency, peak magnetic flux magnitude, strand size and bundle transposition angle. It is given as [66]:

$$P_{se} = \frac{\pi\omega^2 B_{g\_pk}^2 d_{sc}^4 N_{sc} l_w}{128\rho_{cu}} \left(1 + csc(\theta_w)\right) \tag{5.1}$$

where ω is excitation electrical frequency, B_{g_pk} is the average peak magnetic flux density within the winding region, d_{sc} is strand diameter, N_{sc} is total strand number within the calculated winding area, l_w is winding coil axial length, rho_{cu} is copper resistivity coupled with thermal impacts, and θ_w is bundle transposition angle of litz-wire windings.

An analytical solution of $\overline{B_{pk}^2}$ in the winding region is required for ac loss prediction of various winding designs. Regarding the peak magnetic flux square, both radial and tangential components of the air gap magnetic flux need to be accounted for, and are given as:

$$B_{g\_pk}^2(r,\theta) = B_r^2(r,\theta) + B_t^2(r,\theta) \tag{5.2}$$

According to the analytical solution of magnetic field within winding region in [66], $\overline{B_{pk}^2}$ for the ac loss of slotless windings can be derived as

$$\overline{B_{g\_pk}^2} = \sum_{i=1}^{\infty} \frac{2a_i(1+\mu_r)^2}{R_w^2 - R_{sy}^2} \left\{ \frac{4B_{rem}}{D_0} \frac{p}{1-p} \left[1 - \left(\frac{R_r}{R_m}\right)^{p-1} \right] \right\}^2$$
$$\left\{ \frac{R_w^{2p} - R_{sy}^{4p} R_w^{2p}}{2p R_r^{2p-2}} + \frac{2R_{sy}^{2p}(ln(R_w/R_{sy}))}{R_r^{2p-2}} \right\} \tag{5.3}$$

The key component $\overline{B_{pk}^2}$ in ac loss prediction is verified with FEA result assuming i=1. AWG 38 litz wire with 0.244″ (width) by 0.215″ (height) is selected for this motor design. The slot area is fixed at depth 0.215″, which is composed of 3 turns. Analytical prediction of $\overline{B_{pk}^2}$ is 0.998 T^2, which has an error of roughly 2.5% compared with the FEM result of 0.973

T^2. It indicates that the developed equation has a good agreement with the FEM method.

To better predict the total $B^2_{g\text{-}pk}$, the harmonic component effects also need to be accounted for. The a_i is the ith harmonic percentage according to the FFT analysis of the magnetic waveforms in the gap. Figure 5.4 shows the magnetic waveform at outer winding radius. It is not a perfect sinusoidal waveform, but has 13th harmonic ripples since there are six pieces forming as a Halbach array in each pole. Figure 5.5 summarizes the harmonic distribution. While the fundamental component dominates as 99.5%, the 13th harmonic has 3.63% which causes 21% more induced-current loss than does the fundamental component. With the FFT profile in Figure 5.5, the extra harmonic induced-current losses can then be calculated.
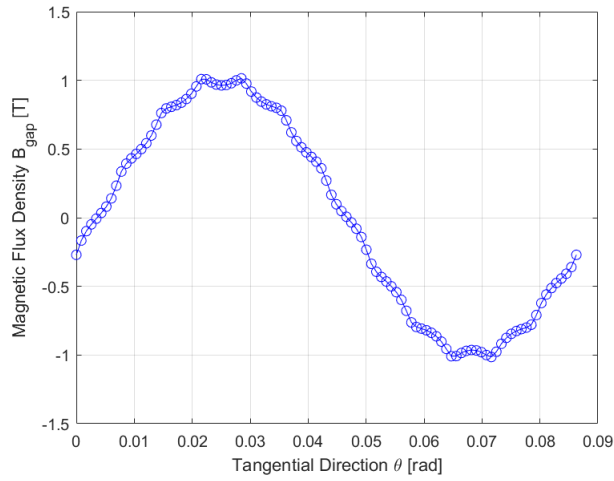
Figure 5.4: Magnetic Flux Density Distribution at Outer Winding Radius along Tangential Direction

Similar principles can be applied to predict bundle eddy current loss by external magnetic field. The evaluation formula of bundle eddy current loss is given as [66]:

$$P_{be} = \frac{p_w^2 \omega^2 B^2_{g\text{-}pk} d_b^2 N_b l_w}{32 \rho_{ss}} \left(1 + csc(\theta_w)\right) \tag{5.4}$$

where p_w is winding pitch length, d_b is bundle diameter, N_b is bundle number within the winding cross section area, and ρ_{ss} is bundle resistivity. The bundle eddy current loss tends to be much smaller than the strand eddy current loss, since bundle composite resistivity is much higher than copper resistivity. In some cases, bundle eddy current loss can be ignored.
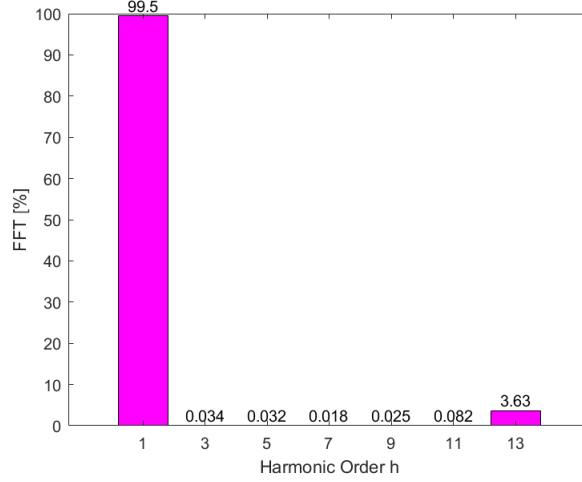
Figure 5.5: FFT Analysis Results of Gap Flux Waveform

Given the above eddy current prediction formulas at strand and bundle level, the total ac losses of slotless litz-wire windings can be obtained as:

$$P_{ac} = P_{se} + P_{be} \tag{5.5}$$

5.2.3 DC Loss Analysis

The copper conduction loss is the dc loss of slotless litz-wire windings. The winding dc loss can be determined by the copper current density and the total copper volume (including transposition angle effects). The copper resistivity property should include thermal effects. The litz wire copper conduction loss, P_{dc}, can be evaluated by:

$$P_{dc} = J_{cu}^2 \rho_{cu} N_{sc} \pi r_{sc}^2 l_w \left(1 + csc(\theta_w)\right) \tag{5.6}$$

5.3 Thermal Analysis

5.3.1 Litz Wire Equivalent Thermal Conductivity

The litz wire is a complicated composite, consisting of conductor, insulation layers and potting material. Using FEA to predict litz wire thermal performance is a time-consuming and

complicated process. However, analytical methods are computationally efficient and flexible enough to be coupled with the established litz wire electrical model. The litz wire equivalent thermal conductivity including transposition effects has been thoroughly investigated in Chapter 4. This chapter details an analytical model to calculate litz wire equivalent thermal conductivity. This analytical model has been validated both in detailed FEA simulations and hardware tests. It can be easily integrated into the slotless litz-wire winding optimization design process.

5.3.2 Litz Wire Temperature Performance

Given litz wire equivalent thermal conductivity, the temperature rise across the slotless litz-wire winding block can be calculated. The heat flux is assumed to flow through conductors and insulation layers towards the winding bottom surface. The winding heat is generated uniformly on the winding cross section area. In order to find the temperature difference across the winding block, a general thermal equivalent circuit is developed, as shown in Figure 5.6.
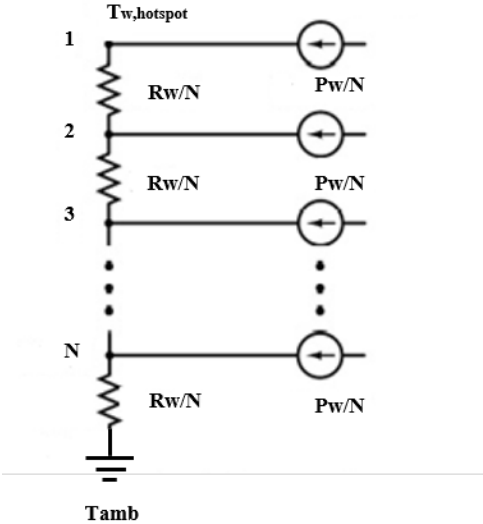

Figure 5.6: General Thermal Equivalent Circuit of Slotless Winding

Suppose winding block and loss are uniformly divided into N pieces and distributed across

the whole winding block.

$$P_{w,i} = P_w/N \tag{5.7}$$

where $P_w = P_{ac} + P_{dc}$ winding loss consists of total dc and ac losses of the confined winding conductors.

$$R_{w,i} = R_w/N \tag{5.8}$$

where Rw is winding corresponding thermal resistance.

By applying circuit superposition principles, the winding hotspot potential equals to the sum of the temperature potential at each node point i. In order to find the winding temperature rise dT_w, each node temperature potential needs to be evaluated first. The corresponding evaluation formula can be obtained as:

$$T_{w,i} = P_{w,i} \sum_{j=1}^{i} R_{w,i} = \frac{i}{N^2} \tag{5.9}$$

Then we can derive the winding hotspot temperature potential with the sum of all the node temperature potentials, given as:

$$T_{w,hotspot} = \sum_{i=1}^{N} T_{w,i} + T_{amb} \tag{5.10}$$

$$dT_w = T_{w,hotspot} - T_{amb} \tag{5.11}$$

As the division number goes to infinity, the formula converges to a concise solution. The winding temperature rise calculation formula can be obtained with a lumped winding heat loss and thermal resistance, given as:

$$dT_w = \lim_{N \to \infty} \sum_{i=1}^{N} T_{w,i} = \frac{P_w R_w}{2} \tag{5.12}$$

Suppose the winding loss is dominant on the stator. The iron loss and gap heat transfer effects can be neglected. That means the winding heat load behaves as a current source in series with the winding, yoke and heat sink thermal resistance. One quick estimation of the

stator hotspot temperature can be derived as:

$$T_{hotspot} = P_w \cdot (\frac{1}{2}R_w + R_y + R_{hs}) + T_{out} \qquad (5.13)$$

where R_y is the stator yoke lumped thermal resistance, R_{hs} is the heat sink lumped thermal resistance, and T_{out} is the outlet air coolant temperature. The air coolant temperature at the outlet can be predicted with the following equation:

$$T_{out} = \frac{P_w}{C_{air}V_{air}\rho_{air}} + T_{amb} \qquad (5.14)$$

where C_{air} is air heat capacity, V_{air} is air volume rate, ρ_{air} is air density, and T_{amb} is ambient temperature that is usually assigned as 40 °C.

Both winding temperature rise and stator hotspot temperature prediction methods are presented and discussed. The tools developed in this section will facilitate slotless litz-wire winding design and optimization with coupled electro-thermal analysis.

5.4   Electro-Thermal Optimization Design of Slotless Winding

This section focuses optimizing transposition angle and strand size at the litz-wire level, and turn number at the form-wound winding level. The established electro-thermal analytical model in the previous sections is applied in the winding optimization scheme. The winding optimization picks a square litz wire as an example with dimensions, fill factor, and gauge size listed in Table 5.1.

5.4.1   Strand and Transposition Angle (θ) Optimization

The relationship among strand size, bundle transposition angle, and litz wire AC loss is plotted in Figure 5.7a. Although the fill factors of the AWG size wires are within 50% of each other, total induced-current loss varies quadratically with strand size while assuming motor magnetic loading and litz wire dimensions remain the same. As bundle transposition angle increases from 0 to 40 degrees, AC loss value rises slowly below 20 degrees and faster

69
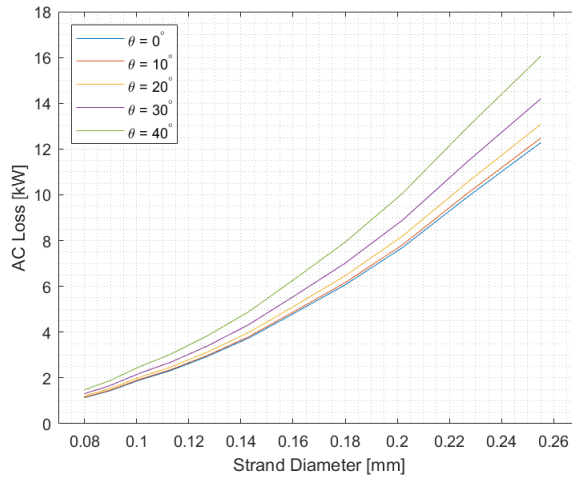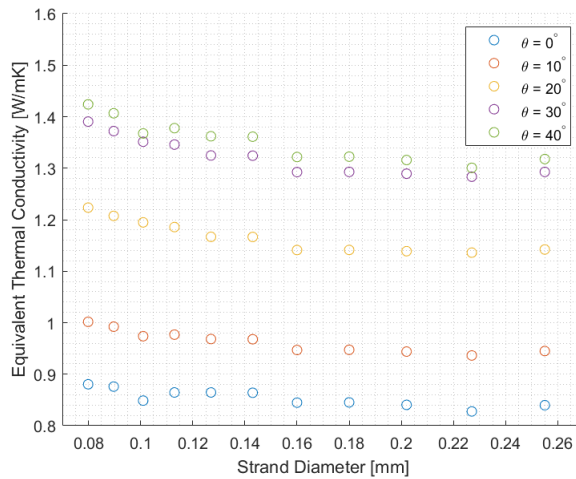
(a) AC Loss

(b) Wire Thermal Conductivity

Figure 5.7: AC Loss and Equivalent Thermal Conductivity Predictions of AWG 30–40 with Various Bundle Transposition Angle

beyond 20 degrees. Figure 5.7b shows how litz wire equivalent thermal conductivity changes with different bundle transposition angles. It is observed that strand size does not affect litz wire thermal conductivity since the copper fill factors of the AWG wires are close. But transposition angle does improve litz wire heat conduction capability by providing an extra cooling path. As transposition angle varies from 10 to 30 degrees, litz wire thermal conductivity improves fast. When transposition angle rises more than 30 degrees, the heat dissipation enhancement benefit margin decays.

70
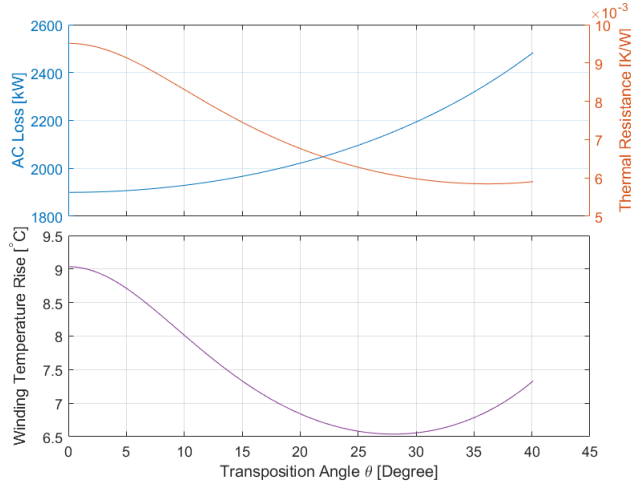
(a) AWG 38
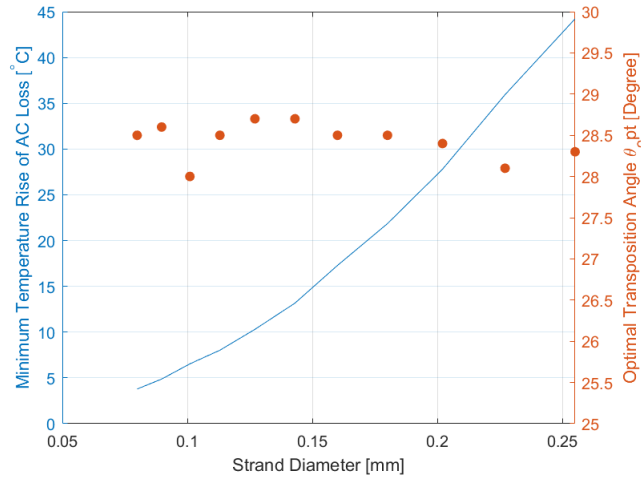
(b) Optimal Transportation Angle

Figure 5.8: Finding Optimal Transposition Angle of AWG 30–40 in Terms of Minimizing Winding Temperature Rise Generated by AC Loss

Figure 5.8a illustrates the trade-off between AC loss and winding thermal resistance of AWG 38 litz wire. The winding temperature rise, dT_w, is proportional to the product of $P_{ac}(\theta)$ and $R_w(\theta)$, and has minimum temperature rise at 28 degrees. The similar process of finding optimal transposition angle is applied to other AWG sizes. It turns out the strand size does not affect the optimal transposition angle. The optimal transposition angle falls between 28 and 29 degrees.
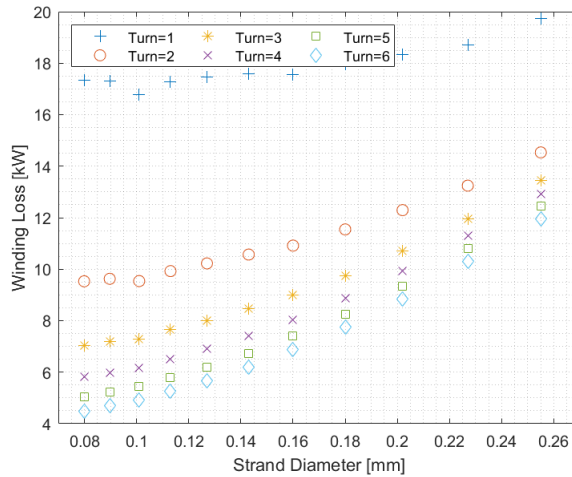
(a)
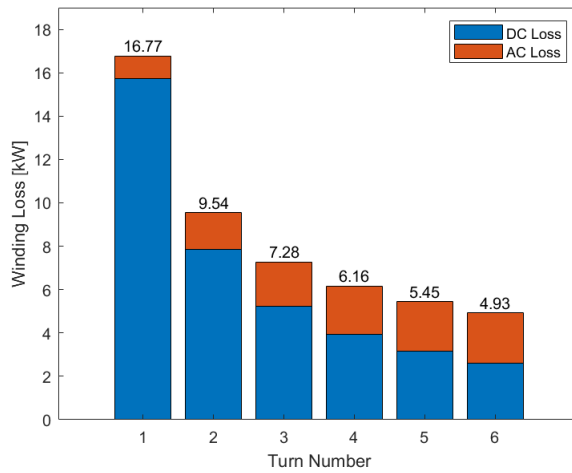
(b) AWG 38

Figure 5.9: (a) Winding Loss vs. Winding Turn Number and AWG Size (b) Winding Loss Distributions along Turn Number of AWG 38

5.4.2 Turn Number Optimization

This section uses the optimal transposition angle findings of Figures 5.8a and 5.8b. Assume the motor electric loading stays the same as in the MW motor. The only modifying parameter is the form-wound winding turn number, which affects the winding radial depth. The trade-offs between the total winding loss and stator hotspot temperature of each AWG size in the selected litz wires are studied in detail.

Figure 5.9a shows the winding loss correlation with gauge size and turn number. When
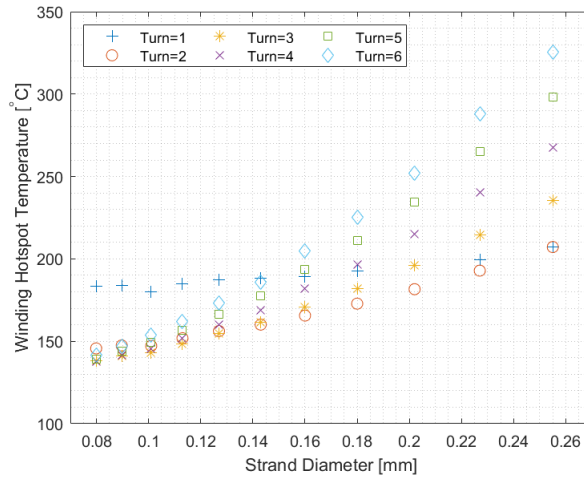
(a)
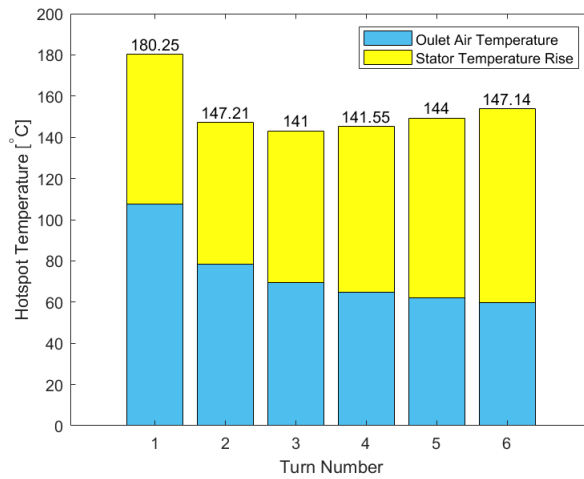
(b) AWG 38

Figure 5.10: (a) Finding Optimal Turn Number with Minimum Stator Hotspot Temperature (b) Temperature Distributions along Turn Number of AWG 38

turn number equals one, the winding loss does not vary with gauge size because the copper fill factor does not change and conduction loss dominates in this case. As the winding turn number increases, the conduction loss reduces proportionally with the inverse of turn number, but the AC loss rises with turn number. More details are plotted in Figures 5.9b with AWG 38 as an illustration example.

Figure 5.10a shows the stator hotspot temperature correlation with gauge size and turn number. When gauge size is smaller than AWG 35, the optimal turn number is 3, although

turn numbers 2 and 4 can achieve similar hotspot temperatures. As gauge size is larger than AWG 35, the optimal turn number is 2. According to Figure 5.9a, the lowest winding temperature rise is expected at turn=1. However, due to the large amount of total winding loss at turn=1, the outlet temperature of coolant takes over to reduce the advantages of the low winding temperature rise. More details are plotted in Figure 5.10b with AWG 38 as an illustration example.

CHAPTER 6

MOTOR DESIGN OPTIMIZATION AND CASE STUDY

6.1   Optimization Scheme

6.1.1   Objectives and Design Variables

Given the developed multi-physics model, we need to find the optimal machine design for maximizing machine specific power and efficiency. A MATLAB toolbox, GOSET, was developed based on an evolutionary genetic algorithm to perform complicated nonlinear machine design problems [67].
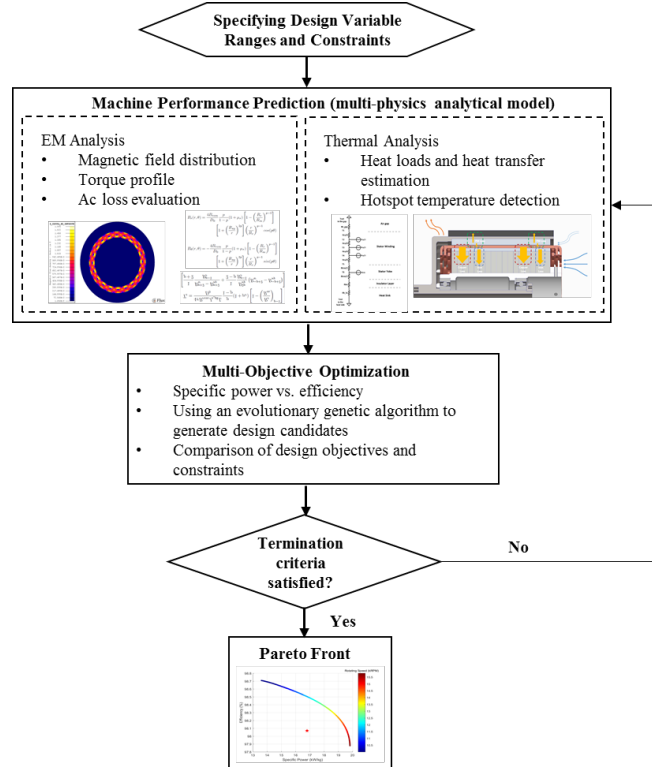
Figure 6.1: Multi-Objective Multi-Physics Optimization Process

The optimization process is illustrated in Figure 6.1. The electrical motor power can be expressed as the product of the gap volume, electrical loading, magnetic loading and motor speed. Magnetic loading depends on magnet and iron volume and is constrained by mechanical factors, such as tip speed and rotor dynamics. Electric loading relies on copper volume and is constrained by thermal factors, such as cooling scheme and material temperature limit. Overall, the design objective functions can be written as

$$\max_{x} \quad s.p.(x) = \frac{P_{out}(x)}{M(x)}$$
$$\eta(x) = \frac{P_{out}(x)}{P_{in}}$$

(6.1)

where P_{in} is a fixed input power (1 MW), $s.p.(x)$ is the specific power function, and $M(x)$ is the motor active mass function. In this optimization, the design vector is defined as

$$x = \{R_m, d_m, d_w, \omega_m, J_s\}$$

(6.2)

where the upper bounds and lower bounds are specified as

$$
\begin{aligned}
0.1 \leq R_m \leq 1 & \quad \text{(m)} \\
0.001 \leq d_m \leq 0.1 & \quad \text{(m)} \\
0.001 \leq d_w \leq 0.1 & \quad \text{(m)} \\
10 \leq \omega_m \leq 20 & \quad \text{(krpm)} \\
4 \leq J_s \leq 20 & \quad \text{(A/mm}^2)
\end{aligned}
$$

(6.3)

6.1.2 Constraints

The feasibility of a given candidate design is evaluated by the constraints defined below:

1. Retaining ring thickness (m)

$$d_{rr}(x) - 0.025 \leq 0$$

(6.4)

2. Rotating tip speed (m/s)

$$(d_{rr}(x) + R_m) \cdot \omega_m - 275 \le 0 \tag{6.5}$$

3. Stator inner radius (m)

$$0.06 - R_i(x) \le 0 \tag{6.6}$$

4. Thermal $(\degree C)$

$$T_{max}(x) - 180 \le 0 \tag{6.7}$$

5. Efficiency $(\%)$

$$96\% - \eta(x) \le 0 \tag{6.8}$$

6. Specific power (kW/kg)

$$13.6 - s.p.(x) \le 0 \tag{6.9}$$

All these constraints are nonlinear and defined according to physical principles, material properties and design requirement specifications.

6.2   1 MW NASA Motor Study

For a preliminary investigation, the optimization is allowed to operate in a design space range varied around the baseline. The baseline design metrics were derived from rigorous EM, mechanical, and thermal finite-element results. Manufacturing capabilities and safety factors were also taken into account. The Pareto-front was generated with a 1000-individual, and 10,000-generation optimization run. It shows the trade-off between specific power and efficiency in regard to machine sizing parameters (including pole number, magnetic loading, electric loading, stator volume and rotating speed).

(a) Pareto-front of Efficiency vs.Specific Power   (b) Specific Power vs. Speed
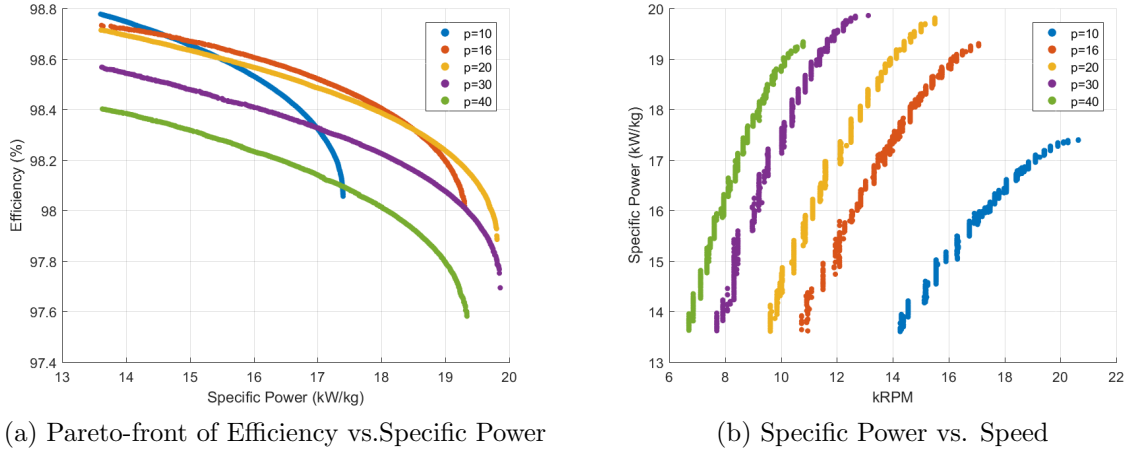
Figure 6.2: Pole Count Study

6.2.1 Optimal Pole Count Study

The Pareto-fronts of five pole-count numbers are compared in Figure 6.2. In Figure 6.2a, it is interesting to note that the maximum pole count number does not necessarily lead to the highest specific power design. For example, 20-pole and 16-pole Pareto-front designs both have better efficiency and specific power than 30-pole and 40-pole designs. And the Pareto-front starts shifting inwards after the optimal pole count (p=20). This indicates that the benefits of increasing pole count are canceled out, since high-pole-count designs tend to have more frequency-based electrical and mechanical loss, and requires more aggressive cooling power.

Additionally, Figure 6.2b shows that the maximum specific power occurs between pole number 20 and 30. The optimal rated speed of the different pole counts varies significantly. The high-pole-count designs result in lower optimal speed because of the thermal cost of handling higher losses. The low-pole-count designs result in higher optimal speed, due to weight and volume reduction at higher speeds. Overall, our primary design falls into the optimal pole number range. The following Pareto-front study will be based on the selected pole-count number (p=20).
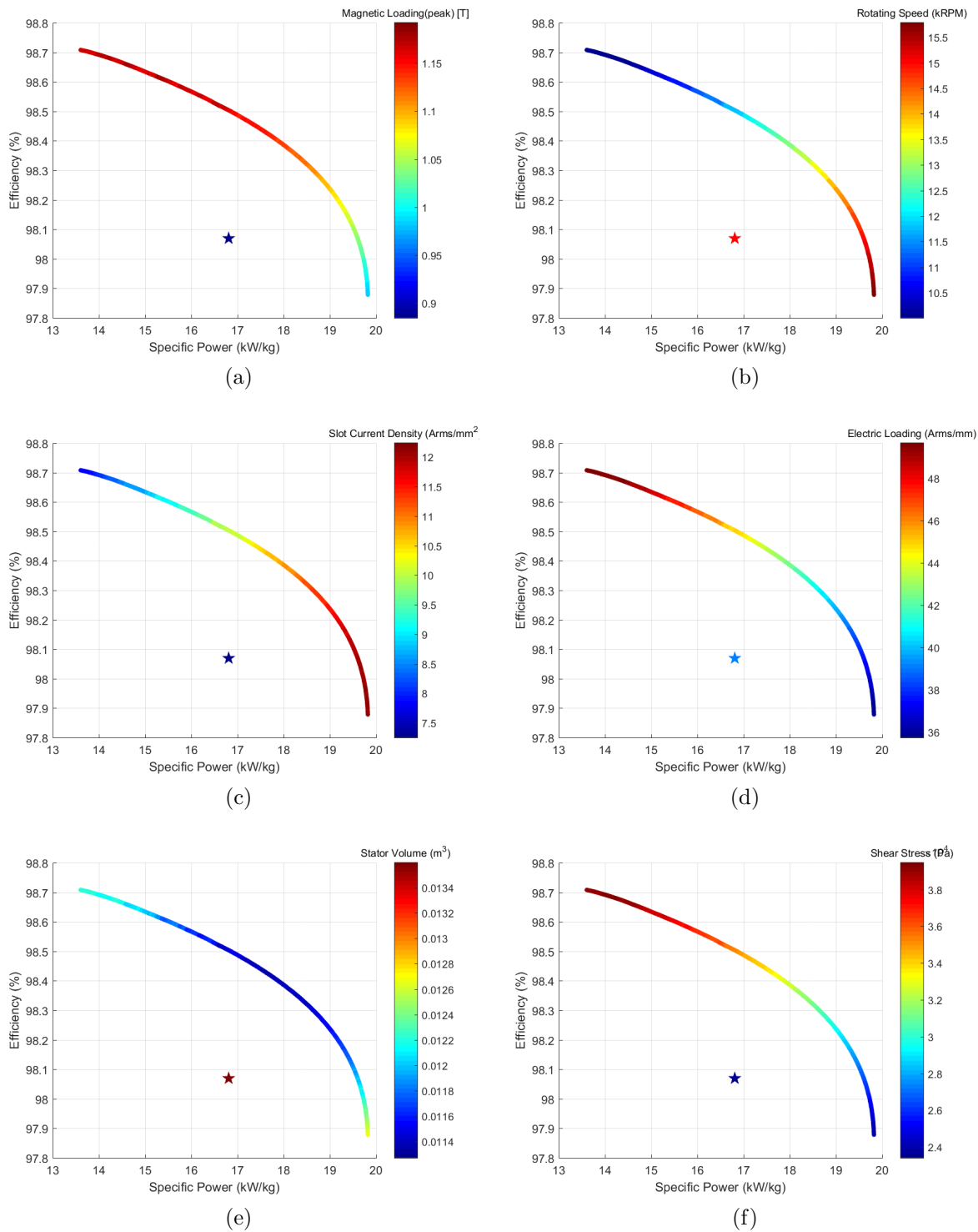
Figure 6.3: Pareto-front Study

6.2.2 Pareto-Front Study on Machine Primary Design Factors (p=20)

The designs in the Pareto-front set vary along with the rotating speed shown in Figure 6.3b. Higher-speed designs result in higher specific power but lower efficiency. Although increasing rotating speed is the first obvious option for increasing specific power, mechanical challenges limit the capabilities of magnetic loading and electric loading.

Figures 6.3a and 6.3c show magnetic and electric loading effects in determining specific power and efficiency. More magnetic loading and electric loading are required to reach the rated power specification for the lower-speed designs. Lower retaining-ring stress due to lower rotating speed allows a higher magnet volume to provide higher magnetic loading. And less frequency-associated loss gives room to sustain more dc-current loss and, thus, more electric loading. The shear stresses are higher than those of higher-speed designs as indicated in Figure 6.3f, because of higher magnetic and electric loading of lower-speed designs. However, a higher magnet and copper volume causes more machine weight and thus leads to lower specific power in lower-speed designs. It is difficult to maintain high magnetic and electric loading due to severe thermal and mechanical constraints in higher speed designs. While increasing magnetic and electric loading is an effective way to increase specific power, such a design strategy is only valid for lower-speed designs.

The slot current density and electric loading Pareto-fronts show opposite trends as indicated in Figure 6.3c and 6.3d. A lower slot current density leads to higher efficiency but to lower specific power. Nevertheless, lower electric loading results in lower efficiency but higher specific power, which might seem counter-intuitive. This can be attributed to the use of copper volume, current density and speed. At lower speed, a large copper volume is needed to supply adequate electric loading for the required rated power. Also, lower speed causes less mechanical loss, iron loss, and ac loss. This leaves more space to sustain more dc loss in the copper. That means more current and copper volume can be allowed at lower-speed designs.

Another interesting indication is from the Pareto-front of the stator volume in Figure 6.3e. It is reasonable to expect that higher speed leads to smaller stator volume designs with the same rated power specification. However, the plot in Figure 6.3e shows that the stator

volume does not decrease along with increasing speed, which actually reaches the minimum in the middle of the speed design range. This means the magnetic and electric loading reach saturation in high-speed designs due to lower efficiency and less structural integrity. Thus, high-speed designs must favor a large stator volume to compensate for the loss in magnetic and electric loading.

### 6.2.3 Machine Design Factors for Optimizing Specific Power (p=20)

This section presents the effects of other design factors, such as key component sizes, dimensions, speed, and losses, in high-specific power machine design. These effects can further explain the observations made in the Pareto-front section.

Although specific power increases along with rotating speed in Figure 6.4a, it seems that specific power reaches the maximum at 16,000 rpm. Any increase in speed beyond the optimal point will not improve specific power, since insufficient magnetic and electric loading can be provided at high rotating speed. The machine size must increase to reach higher power requirement.

The higher-speed designs result in high specific power but lower efficiency. Lower-speed designs lead to the opposite. Figures 6.4b and 6.4c indicate that lower-speed designs feature high copper and magnet volume, and thus can maintain high magnetic and electric loading. Even though a higher-speed design can achieve high specific power by reducing copper and magnet use, its magnetic and electric loading is also reduced. The best balance among speed, magnetic, and electric loading will achieve the maximum specific power design.

Figures 6.4d and 6.4e present the important dimensions in high-specific-power designs. It turns out that the baseline design falls into the optimal range in regard to aspect ratio and the outer-diameter dimension. Increasing the outer radius might not always improve specific power due to structural integrity and stability issues.

Figure 6.4f shows loss distributions along with specific power. The lower-speed designs have higher efficiency because of lower electrical frequency and higher copper volume to provide adequate current. However, when specific power increases, its associated speed increases and produces more losses, especially frequency-based. According to the heat load
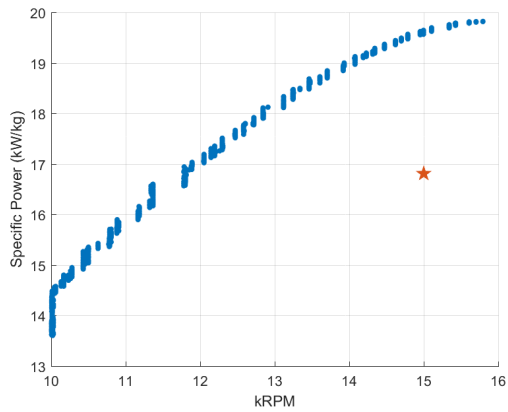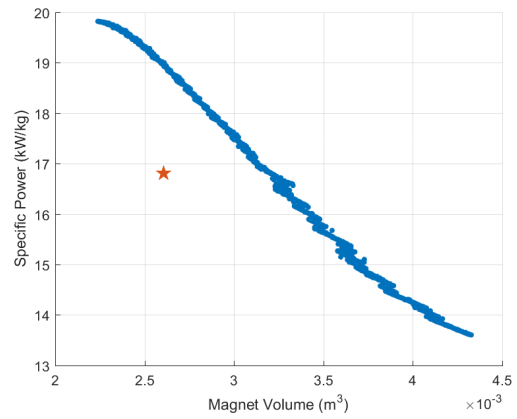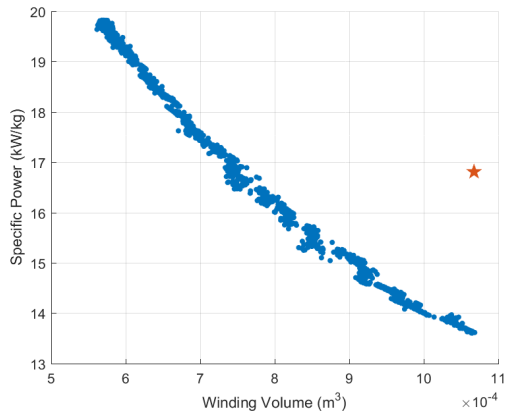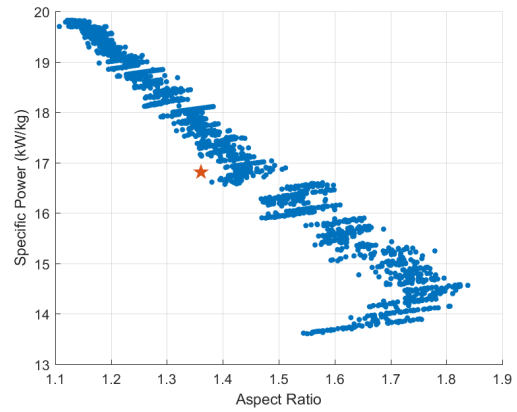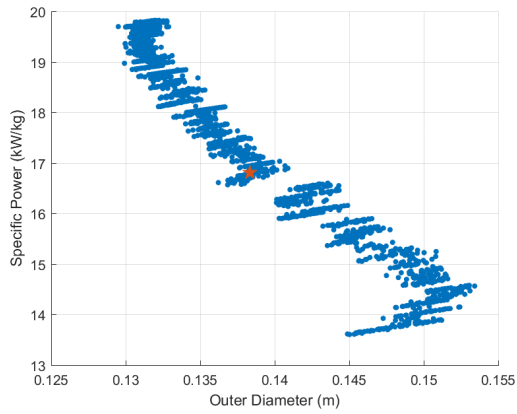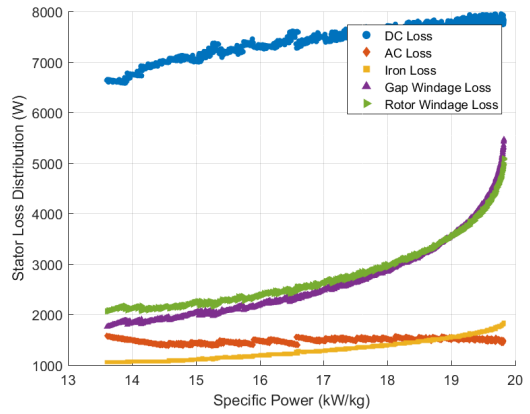
Figure 6.4: Specific Power vs. Other Factors
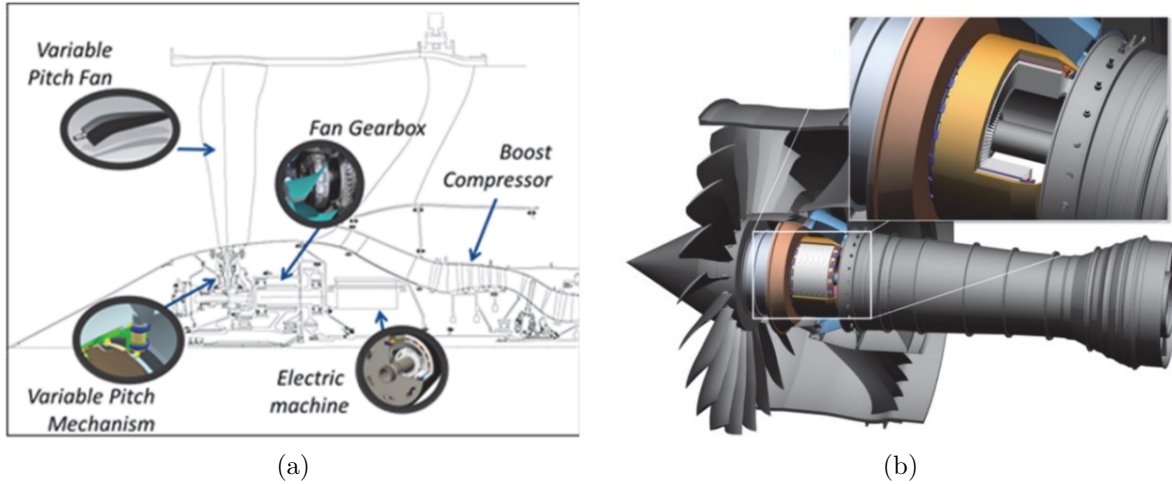
Figure 6.5: Electric Propulsion Engine with Illinois Motor/Generator Integration [68]

correlations in Chapter 2, electrical and mechanical losses could be quadratically and cubically proportional to speed. The limited cooling capabilities can reduce electric loading at high-speed operation, although higher speed results in higher specific power designs.

6.3 Overview of Thermal Integration Methods for EVE

The commercial aircraft industry is actively working towards electrification technology to improve efficiency and reduce emissions. One sizing study of a single-aisle transport with the electrically variable engine (EVE) shows the optimal motor sizing needs to be between 2500hp and 3500hp per engine. Up to 25% fuel reduction and 10% on-board energy usage can be achieved [68]. High-specific-power electrical machine is identified as a critical component in hybrid-electric propulsion engine design [69]. In the high-specific-power machine design, thermal challenges become more significant than usual, due to higher loss density and less cooling surface area [46]. Therefore, thermal management capability could directly determine machine sizing and performance. Different coolant properties, flow speed, and inlet temperature result in significant changes in electrical machine designs. Although the thermal management system (TMS) of hybrid electric propulsion has been studied [70], [71], its impacts on motor sizing and performance have not been discussed yet.

The proposed high-specific-power motor is an outer-rotor permanent-magnet machine with

the target efficiency over 96% and specific power over 13.6 kW/kg [1]. This motor is an initial demonstration of MW-level lightweight electrical machine technology for electric and hybrid-electric airplane propulsion system. An air cooling strategy is selected for the requisite no-liquid coolant pumping system and can be directly integrated into the propulsion system where a large amount of ambient air is flowing. In the Rolls Royce gas-electric hybrid engine configuration of Figure 6.5, the proposed motor is connected indirectly to the variable pitch fan through a gearbox. Some of the air pumped by the variable pitch fan flows through the motor and then the three-stage LP compressor system. The other ambient air flow path is through the structural outlet guide vane to cool power electronics and the thermal management system heat exchanger. The ambient air flowing through the electrical components can absorb the loss generated by the electro-mechanical system. The warmed up ambient air can be then compressed and sent to the combustion chamber. Therefore, the electro-mechanical system loss can be utilized for better combustion performance, and the overall propulsion system efficiency improves.

6.3.1 Stator Thermal Management

The stator cooling system is used to remove the heat generated by the electromagnetic components on the stator and maybe partial friction loss within the gap between the rotor and stator. There are three cooling methods considered for stator cooling.

Air Cooling

Air cooling machine is typically driven by an external fan where cooling air is forced to pass through. Mixed convection (forced and natural convection), conduction, and radiation occur to extract heat from machines. Although air cooling contributes negligible cooling weight to the machine, poor thermal conductivity and heat capacity of air make aggressive heat extraction of the air-cooling method more challenging compared with liquid cooling method [72], [73]. Thermal fins and ducts can be mounted on rotor and stator to increase cooling area and heat transfer effects. The gap between stator and rotor also forms a duct for air to pass through. Various shapes and dimensions of the heat sink can impact cooling

efficiency and pumping cost in fan-cooled machines. One example in aircraft applications
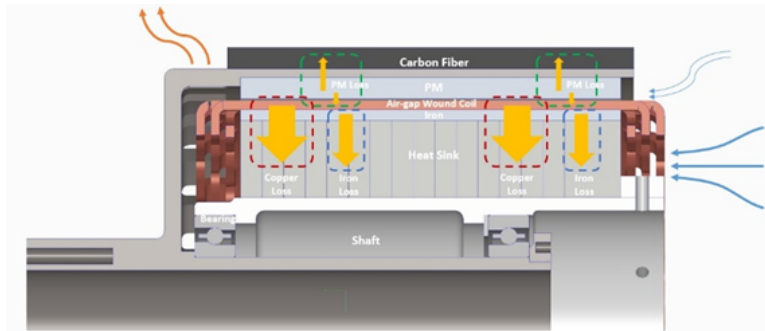
Figure 6.6: Self-Pumped Air-Cooling Method

is a self-pumped air-cooling motor design [8]. Many thermal fins are extended from stator yoke to shaft to form cooling ducts. Airflow is produced by the centrifugal fan blades on the rotor disk inside, as shown in Figure 6.6. The centrifugal fan pumps the air from the right side of the cooling ducts to outlet holes on the rotor. Another example is to utilize available ambient air flowing toward the compressor [74]. No self-pumped fan is needed for the motor in this case, which saves weight for the overall engine system. The air cooling method has advantages of minimizing thermal management weight and improving propulsion engine efficiency. The uncertainty is air flow control and particles that could damage the motor structure.

Indirect Liquid Cooling
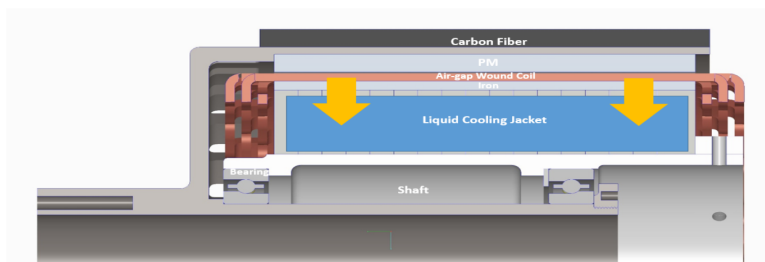
Figure 6.7: Indirect Liquid Cooling Method

More aggressive and effective thermal management is implemented via liquid jacket cooling. Coolant jackets of various design types (axial and circumferential ducts) are mounted

on stator and rotor. The coolant can also be passed down through cooling channels. Oil or water is used as a liquid coolant due to their higher thermal conductivity and heat capacity to improve convection effects. However, their viscosity is much greater than that of air and thus requires extra pumping efforts. For example, a water jacket housing is mounted on the outside of the ultra-high-speed motor in [75]. The coolant is completely sealed inside and passed through the whole stator outer surface shown in Figure 6.7. Even though water has high thermal conductivity and heat capacity, it is difficult to manage for aircraft applications. Extra heat is needed to keep water in liquid status at the high-altitude cruising and under cold weather. The liquid coolant can be replaced by lubricant oil. The lubricant oil is cooled by fuel oil in TMS. Such a method can utilize the heat generated in the motor and warm up fuel oil for the combustion process. Therefore, the overall engine system efficiency can be improved. Compared with the air-cooling method, indirect liquid cooling has advantages of more precise control of coolant temperature and mass flow rate. The disadvantages are the extra pumping cost and maintenance requirement.

Oil Spray
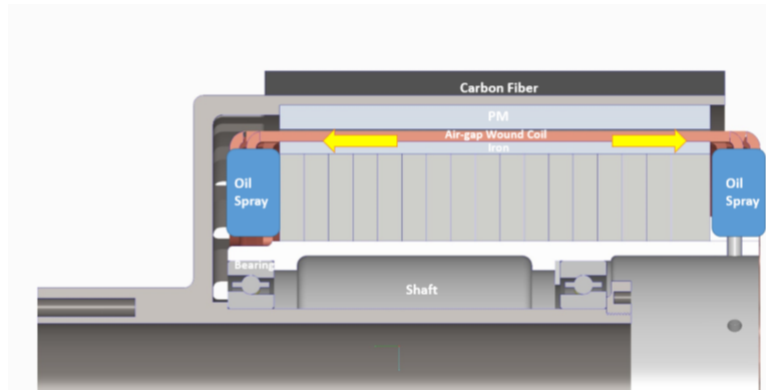
Figure 6.8: End-Winding Oil Spray Method

Another efficient cooling system is oil spray cooling. The oil is typically sprayed around the stator end-space region and splashes over the rotor ending surface with or without nozzles. Since stator winding has a high-temperature rise through radial conduction, spray cooling of end-winding is useful to extract the heat through axial direction with less thermal resistance

along the path. As indicated in Figure 6.8, the primary heat flux flows axially. The oil spray cooling is preferred for 'disk' shape electrical machines. Lower coolant flow rate is required for oil spray since it spreads out coolant droplets or drizzling flow at high speed [76]. Such a method only requires a small amount of coolant to achieve cooling performance equivalent to that of the liquid jacket cooling method. However, spray cooling has spray coolant collection challenges. There is a risk of the gap being blocked by spray coolant during high-speed rotation.

6.3.2 Rotor Thermal Management

There are fewer available rotor thermal management options because the rotor is a spinning component in ambient or coolant fluid conditions. Due to the high-speed characteristics of the proposed motor, it is impossible to allow rotor spin in any liquid environment with high viscosity. The air-cooling method seems the only solution to cool the rotor. However, the high-tip-speed rotor results in a large amount of air viscosity (windage) loss. One solution is to direct some of the ambient air used for compression through motor directly. Another solution is the self-pumping method by integrating a fan into the rotor or shaft.

6.3.3 Phase Change Material Integration

Phase change materials can store or release large amounts of heat energy employing phase change, such as melting/solidifying. The use of phase change material (PCM) is promising for short transient duty of high-specific-power electrical machines, especially in aircraft applications. High electric loading of electrical machines is required during airplane takeoff while only moderate electric loading is needed at the cruising stage where the steady-state operation is less thermally constrained.

Many of phase change materials are characterized by high heat capacity and low thermal conductivity. PCM needs to be placed close to heat sources to lower the temperature gradient. One way is to integrate PCM into stator windings [77]. Hollow conductors are used to containing PCM inside stator windings. Part of the winding space is lost in this case.

Another way is to integrate into a stator heat sink. In many power electronics applications, PCM is contained within the heat sink fins to add extra heat capacitor [78].

One type of PCM has desired physical properties for short-transient-duty electrical component applications. Liquid metal materials, including Field's metal, Ga, and In, have both high heat capacity and thermal conductivity. Although the density of liquid metal is higher than that of light metal materials, a small amount could be sufficient for electrical machine short-peak-power operation. According to [79], Field's metal is assumed to be capable of being integrated within the stator heat sink and winding region to evaluate its potential benefits during the takeoff stage for the following study.

6.4   Thermal Integration of Motor Study with EVE

The goal of this study is to find which stator cooling method can achieve the best motor performance in terms of efficiency and specific power. The motor is sized at both takeoff and cruising conditions because temperature drop of coolants and air variations along with altitude lead to significant variations in motor sizing and performance. The motor sizing requires thermal interface information from the engine thermal management system design. [70] is the primary reference for this thermal integration of motor in EVE study. It details a thermal management system performance of a hybrid electric engine under takeoff and cruising conditions. The first-order thermal integration conditions can be obtained to evaluate the following study. Table 6.1 summarizes the key thermal system assumptions used. The coolants include ram air, engine oil, and water. These material thermophysical properties are generally accessible in heat transfer textbooks. Coolant substitutions can be further decided in a detailed aircraft engine design.

During motor sizing optimization process, the stator heat sink teeth are maintained to be 25 mm for problem simplification. There are 120 heat sink teeth aligned with winding slot blocks. Larger cooling channel opening can be achieved based on the motor spacing budget. The coolant is assumed to be pumped through cooling channels in a parallel way. The mass flow rate is fixed within the stator heat sink, and the associated values of different coolants are summarized in Table 6.1. Hence, the axial flow speed of coolant within cooling

Table 6.1: Thermal System Input for Motor Sizing

	Inlet Temp Takeoff [°C]	Inlet Temp Cruising [°C]	Mass Flow Rate [kg/s]	Axial Speed Constraint [m/s]
Ram Air	(40,60)	(0,20)	1.25	60
Engine Oil	(90,110)	(50,70)	4.1	0.02
Water	(50,65)	(10,15)	2.5	0.02

channels becomes a free variable in the optimization. Reasonable flow speed constraints are imposed to guarantee motor design feasibility. The inlet temperature of three target coolants is a range with lower and higher boundaries to accommodate variations in thermal management system design. The takeoff condition is assumed to be close to sea-level. The cruising condition is supposed to be close to 20,000 ft altitude. For simplicity, the coolant temperature is assumed to drop by 40 °C from takeoff to cruising.

6.4.1 Motor Sizing at Takeoff and Cruising Conditions

Two important motor performances, efficiency and specific power, are objects of motor sizing optimization. Ram air, engine oil, and water are selected to cool the motor stator. Motor design is defined at both takeoff and cruising conditions. The mass flow rates of three coolants are fixed at maximum allowable values in Table 6.1.

Figures 6.9 and 6.10 present Pareto-fronts sized at takeoff and cruising conditions separately with various coolant inlet temperatures. It turns out that water can realize the best motor performance indicated by the grey lines in Figures 6.9 and 6.10. The second-best coolant option turns out to be ram air as purple lines in Figure 6.9 and blue lines in Figure 6.10. The highest specific power of using ram air is only 20% to 30% lower than the highest specific power record of the water-cooling method. Sufficient airflow speed and mass flow rate can achieve satisfactory motor performance. Furthermore, ram air can be accessed easily in the aircraft engine and does not contribute extra weight and pumping cost. Note that ram air needs to be filtered first before entering into the motor in case of motor damages caused by dust and metal particles. Engine oil becomes unfavorable in this initial study because of high inlet temperature. Although engine oil thermal conductivity is higher than air thermal
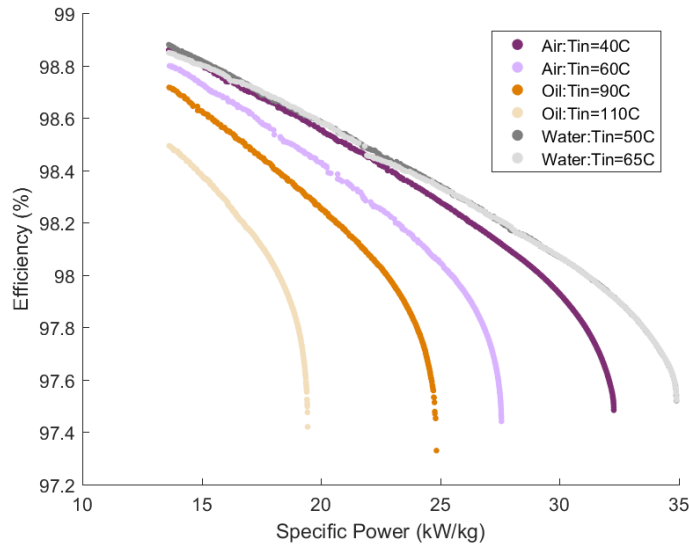
Figure 6.9: Pareto-Fronts of Motor Efficiency and Specific Power at the Takeoff Condition
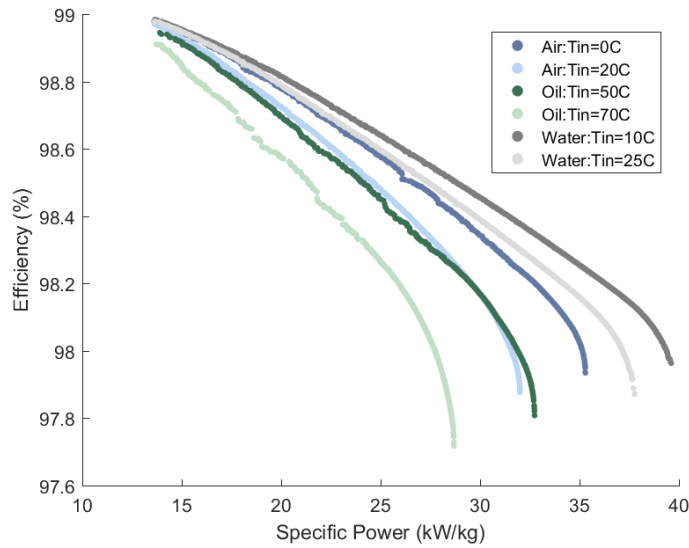
Figure 6.10: Pareto-Fronts of Motor Efficiency and Specific Power at the Cruising Condition

conductivity, its heat capacity has no advantages compared with air heat capacity. The high inlet temperature of engine oil cannot provide enough temperature gradient for the motor to conduct heat out effectively. If lower engine oil inlet temperature can be provided by TMS of the engine, the engine oil could become a better coolant choice than ram air.

If the mass flow rate of each coolant option steps down by the same percentages, motor
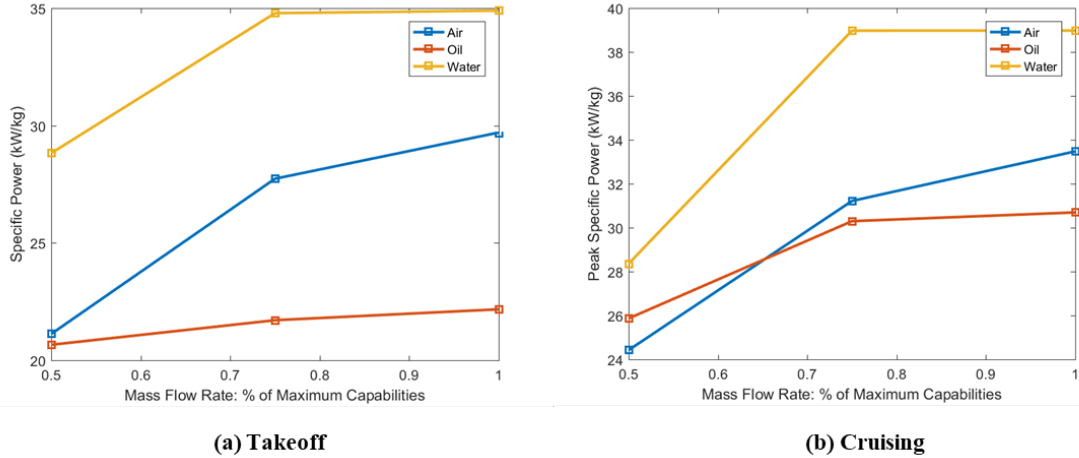
Figure 6.11: Coolant Mass Flow Rate Impacts on Motor Specific Power

performance will favor different coolants for better performance. Figure 6.11 summarizes the coolant mass flow rate influence on motor specific power. Water is still the best option in terms of achieving the lightest motor. At takeoff, ram air cooling can lead to more power-dense motor design than oil cooling. However, the achievable specific power difference between ram air and oil decreases along with lower allowable mass flow rate. Engine oil cooling could be favored in the lower allowable mass flow rate range. At cruising condition, similar trends can be observed. Although ram air seems a better option at 100% of mass flow rate maximum capabilities, ram air becomes the worst one at 50% of mass flow rate maximum capabilities. The reduction in mass flow rate leads to higher coolant outlet temperature and lower axial flow speed. And the air is more sensitive to allowable mass flow rate due to thermal conductivity. Therefore, the performance of the air-cooling method drops faster than that of the engine oil cooling method.

6.4.2 Torque Boost Study of Short-Transient-Duty Operation

This section studies maximum allowable torque during short-transient-duty operation. Especially at the takeoff stage, the motor component has a heat capacity buffer to allow more heat losses generated for a short period of time. The ideal situation is to design the motor at the cruising stage and add more heat capacitance to the motor to boost torque at the

91
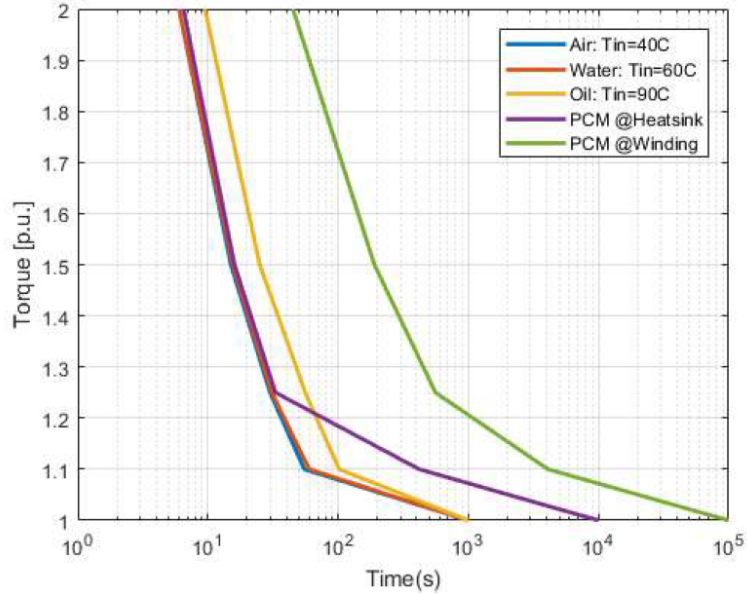
Figure 6.12: Allowable Transient Time for Boost in Torque with Various Cooling Methods

takeoff stage.

Figure 6.12 presents the first-order analysis on allowable transient time for torque boost with various cooling methods. Three design points with the same efficiency of 98.5% were taken from the previous Pareto-front study of lower coolant inlet boundary at takeoff. Note that motor sizing is different in these design points. Figure 6.12 shows that a 10% increase in rated torque can allow 1-2 minutes of transient operation. A 25% increase in rated torque results in a half minute transient operation. Boosts of 50% and 100% in rated torque can only last less than 10 seconds. The motor design with engine oil cooling has more transient operation buffer in terms of boost torque since it has more mass than the ram air- and water-cooling designs. More mass allows more heat capacity buffer to support more heat loss during transient operation.

When phase change material is integrated into the stator heat sink, a small boost in torque, such as 10% to 20%, can last for more than 5 minutes. But no benefits are indicated at the larger boost in torque. Although a large heat capacitance is added to the stator heat sink, the temperature gradient is still high from winding to the heat sink. A better solution is to add phase change material closer to winding. In this case, the winding is assumed to be immersed or mixed within phase change material. Ten percent of winding space is taken

92

by phase change material. The extra heat capacitance of PCM is inserted into each winding node point of the stator equivalent circuit. The allowable short-transient-duty operation time is extended by approximately 1000 times. The PCM integration challenges are extra losses in the winding region and manufacturing capabilities. One solution is to package PCM like a heat pipe and bounded with winding blocks. However, short-transient-duty performance could be reduced due to extra thermal resistance between winding and PCM. A further detailed study is needed to evaluate motor transient performance.

CHAPTER 7

MOTOR TRANSIENT PERFORMANCE STUDY OF PHASE CHANGE MATERIALS INTEGRATION

The transportation industry is moving towards electrification. Many emerging electric transportation applications have widely varying power requirements, depending on the drive cycle in road vehicles, and the hybrid-electric propulsion operation profile in aircraft. Electric motors tend to be intensively used during short time periods, such as the takeoff stage of aircraft. In eVTOL aircraft designs, the takeoff power can be 2-10 times the cruising power. The takeoff process might only take 1–10 min, while cruising might take 10 times that. Even in traditional fixed-wing aircraft, hybrid-electric propulsion systems demand intensive usage of electric motors during parts of the mission, and less in the rest. For example, for Raytheon Technologies project 804 with a parallel hybrid propulsion system [80], electric motors are used primarily during takeoff, the typical mission profile of the motor is shown in Figure 7.1.

High-specific-power and high-efficiency motors are one of the critical enabling technologies behind automotive and aircraft electrification. Motors are usually designed based on the peak power requirement at continuous operation. However, the typical mission profiles only require peak power operation for seconds or minutes. That means the usual motor design method could result in oversizing. One improvement approach is to increase the motor heat capacity by including phase change material. Phase change material (PCM) is regarded as a 'thermal capacitor' that can store or release a large amount of energy through a melting or solidifying process. Therefore, the utilization of PCM can increase the motor 'thermal inertia' and delay the motor temperature rise during the peak-power-operation at takeoff stage [81], [82].

In this chapter, two novel PCM integration methods of a high-specific-power motor for hybrid-electric aircraft applications are presented. Integration concepts are discussed and their impacts on the MW motor transient performances are evaluated using FEA.
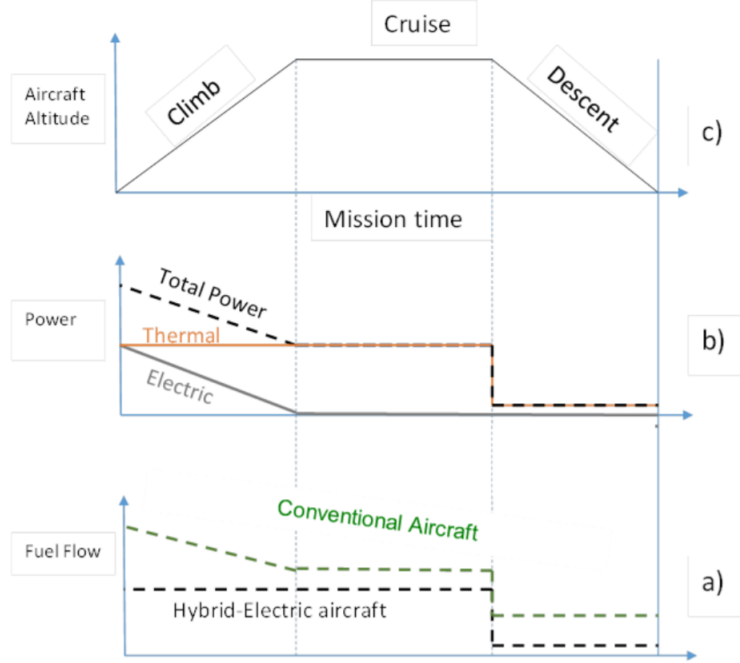
Figure 7.1: Typical Mission Profile Illustration for a Mild Hybrid Aircraft (Raytheon Technologies Project 804) [80]

Table 7.1: Summary of Phase Change Material Thermal Physical Properties [79], [83], [84]

	Melting Point [C]	ρ [g/cm3]	ks [W/mK]	LV [J/cm3]	CVp [J/cm3K]
Field's metal	60	7.88	19	315.2	2.25
Ga	29.8	6.093	33.7	488	2.44
In	156.6	7.01	40	201.2	1.79
Octadecane (paraffin wax)	54	0.88	0.25	245	2.46
H2O	0	1.09	2.2	363.6	2.18
Erythritol	120	1.30	0.326	442	3.4
KF.4H2O	18.4	1.45	0.48	357	3.76
LiNO3.3H2O	30.1	1.42	0.58	407.5	3.92
Na2SiO3·5H2O	72.2	1.45	0.11	387.2	2.38
Ba(OH)2·8H2O	78	2.18	1.255	657	1.17
Climsel C70	70	1.4	0.6	396.1	5.04
S70	70	1.68	0.57	184.8	3.53
A70	70	0.89	0.23	172.1	1.96

7.1 High-Specific-Power Motor and PCM Overview

Before discussing PCM integration methods, a brief review of PCM materials is necessary.

Although there are variety of PCM types, the vast majority fall into three major categories:

organic, inorganic and liquid metals. When selecting PCM materials, the first important property is the melting point. The melting point for electric motor applications usually is within 200 °C. The second factor is the latent heat (kJ/kg) of the fusion. The latent heat measures how much energy can be stored within a specified mass of the material during its melting or solidifying process. Organic and inorganic PCM materials usually have high latent energy and low mass density indicated by Table 7.1. Organic PCM materials are more favored than inorganic materials, since organic material chemical properties are stable. Inorganic material property uncertainties could lead to containment issues. The third selecting factor is thermal conductivity of PCM materials. Although liquid metals have lower latent energy compared with organic and inorganic materials, the thermal conductivity of liquid metals can be 10-100 times that of organic and inorganic materials, as shown in Table 7.1. In some PCM integration methods, such as packaging within heat sink, liquid metals have advantages to reduce thermal resistance within heat conduction path. However, liquid metals have containment challenges, such as corrosion and high mass density, which are not favored in aircraft applications. Overall, organic materials, such as paraffin and erythritol, are the main materials studied in the following two sections, since they have excellent latent energy capability and low mass density.

There are several ways to integrate a PCM package. The most common one is embedding PCM into the heat sink, which is widely used in electronics cooling. But it is not favored here because the large thermal impedance between the hotspot located at the winding region and the heat sink. Reducing the thermal resistance between the most power-dense component, winding, and PCM component, is a more effective approach to increase motor peak-power-transient capability. To bring the PCM package closer to the winding, both end-winding and winding active region can be utilized. The end-winding region seems the best choice overall because it does not hurt electric loading and magnetic loading. Nevertheless, the packaging and manufacturing could be challenging. Therefore, we propose two reasonable ways to integrate PCM in the following two sections.
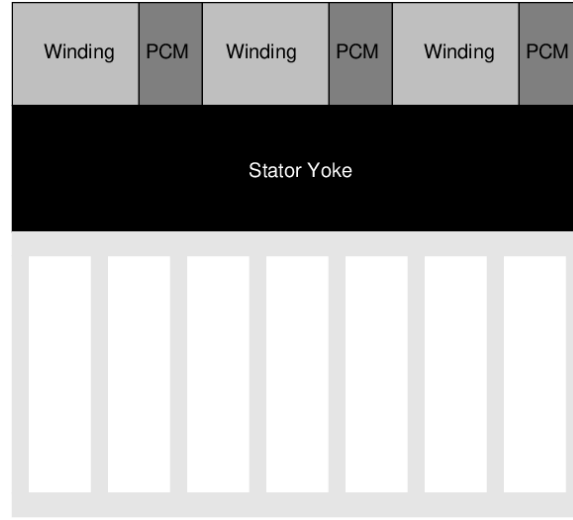
(a)
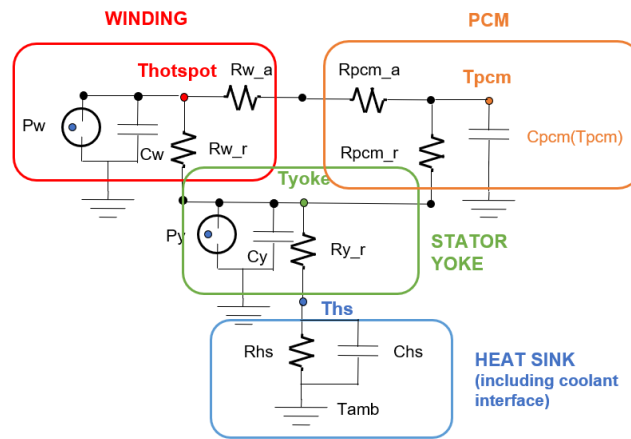
(b)

Figure 7.2: Direct Integration within Slotless Winding Region (a) Geometry Illustration (b) Thermal Equivalent Circuit Model

7.2 Direct Integration within Slotless Winding Region

7.2.1 Concept Overview

The first approach is the direct integration within the slotless winding region. Pipes containing PCM are inserted among the slotless windings. The PCM pipe shell material needs to have good thermal conductivity and high resistivity to reduce induced current losses at high-frequency operation. Ceramic or high resistivity metals, such as titanium, could be suitable

options to contain PCM. Although the PCM package is directly contacting the winding, the low thermal conductivity of PCM, like paraffin, and the limited allowable space could reduce the extension of motor temperature rise time. The following section will discuss further how the PCM thermal conductivity and heat capacity affect motor transient performance.

7.2.2   Modeling Methods

Two modeling methods are used to predict motor thermal transient performance with the PCM integration. One method is to use a thermal lumped equivalent circuit, as shown in Figure 7.2b. There are four main components in the proposed analytical thermal circuit, including the winding, PCM packaging, yoke and heat sink. Correspondingly, only four temperature nodes are evaluated to predict motor stator temperature distribution. The node temperature vector established in Figure 7.2b is given as:

$$T = \begin{bmatrix} T_{hotspot} & T_{yoke} & T_{PCM} & T_{hs} \end{bmatrix}^T \tag{7.1}$$

Winding loss, including copper conduction and eddy-current losses, and iron loss are the two heat sources in the stator. The ambient temperature at the heat sink region is also treated as a heat source fed into the thermal circuit. All the heat sources are treated as current sources. The heat source vector can be summarized as:

$$Q = \begin{bmatrix} P_w & P_y & 0 & \frac{T_{amb}}{R_{hs}} \end{bmatrix}^T \tag{7.2}$$

Given thermal resistor connections in the thermal equivalent circuit in Figure 7.2b, the admittance matrix can be structured as a 4 by 4 matrix, given as:

$$G = \begin{bmatrix} \frac{1}{R_{w\_r}} + \frac{1}{R_{w\_a}+R_{pcm\_a}} & -\frac{1}{R_{w\_r}} & -\frac{1}{R_{w\_a}+R_{pcm\_a}} & 0 \\ -\frac{1}{R_{w\_r}} & \frac{1}{R_{w\_r}} + \frac{1}{R_{y\_r}} + \frac{1}{R_{pcm\_r}} & -\frac{1}{R_{pcm\_r}} & -\frac{1}{R_{y\_r}} \\ -\frac{1}{R_{w\_a}+R_{pcm\_a}} & -\frac{1}{R_{pcm\_r}} & \frac{1}{R_{w\_a}+R_{pcm\_a}} + \frac{1}{R_{pcm\_r}} & 0 \\ 0 & 0 & -\frac{1}{R_{y\_r}} & \frac{1}{R_{y\_r}} + \frac{1}{R_{hs\_r}} \end{bmatrix} \tag{7.3}$$

In order to have transient performance prediction, the capacitance matrix is also needed. Its diagonal cells are filled with capacitance at each node. The corresponding capacitance matrix is shown as:

$$C = diag \begin{pmatrix} C_w & C_y & C_{pcm} & C_{hs} \end{pmatrix}$$

(7.4)

Equations (7.1)–(7.4) establish the key elements needed in the thermal governing equation, as shown in:

$$C\frac{dT}{dt} = Q - G \cdot T$$

(7.5)

The node temperatures can be solved using numerical methods of differential equations, such as Euler method.

The other modeling method uses FEA-based simulation tools. The transient analysis completed in this chapter is implemented in a 2D FEA thermal simulation of FLUX. Half-pole size of stator is modeled to save computational time because of motor symmetry characterization. Small time step size, less than 0.5 second, is required to ensure correct convergence of thermal transient analysis under complicated phase change material properties. Both modeling methods use the exact same motor dimensions, heat loads, material properties, and boundary conditions detailed in [8]. The outer stator boundary has a thermal insulator boundary condition where no heat flux is flowing outward or inward. The heat sink surfaces have the only heat exchange boundary conditions where heat transfer coefficient is assumed as 100 W/m^{2}K, and outlet ambient temperature including total stator heat loads. Once meshing, material properties, boundary conditions and computational settings are assigned, motor transient performance can be obtained.

The advantage of the proposed thermal equivalent circuit is extremely fast computational performance compared with the FEA method. However, the equivalent circuit is a simple 4-node circuit where prediction accuracy is unsatisfactory with an error range of 10%–30%. For the quick first-order analysis, the proposed equivalent circuit method is recommended because of computational time and flexibility to be coupled into any system study. For more rigorous analysis, the FEA method should be adopted at the cost of hours to days of computational time and divergence issues.

In the following sensitivity study, only winding loss density, PCM thermal conductivity
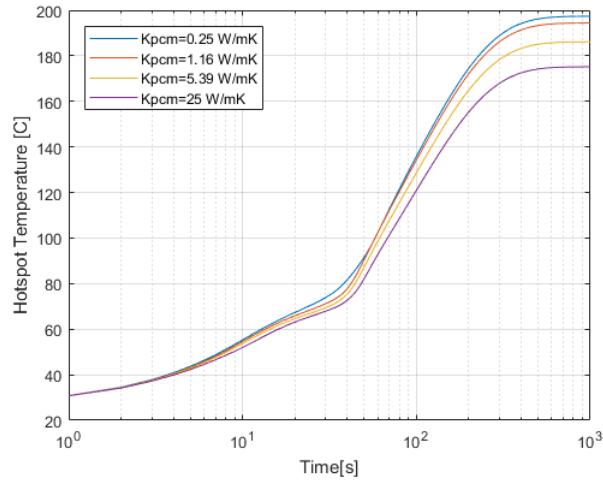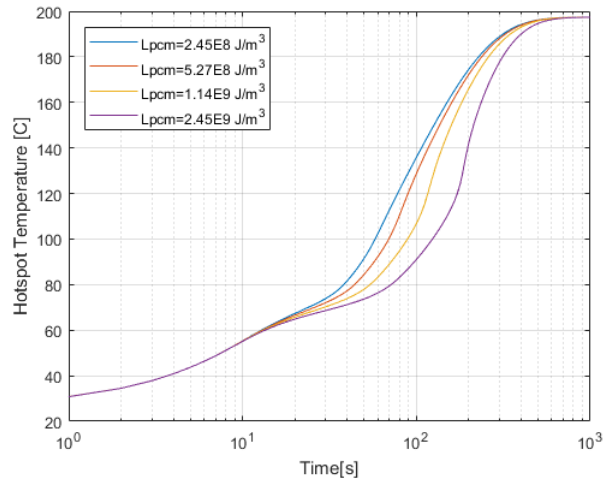
Figure 7.3: Temperature vs. Time with Motor Power Rating at 1 p.u. (using paraffin properties as a reference: K_{pcm}=0.25 W/mK L_{pcm}=2.45E8 J/m³) (a) PCM Thermal Conductivity (b) PCM Latent Energy

(Kpcm) and PCM heat capacity (Lpcm) are defined as the input variables to investigate motor overload transient performances. Since FEA method has satisfactory prediction accuracy, all the results were collected from the FLUX 2-D FEA thermal transient simulations.
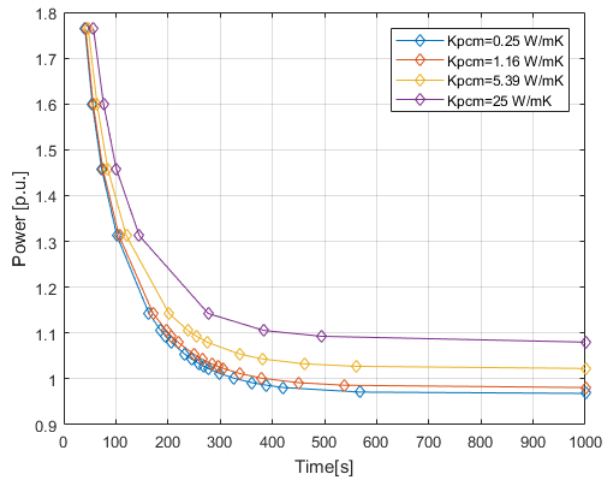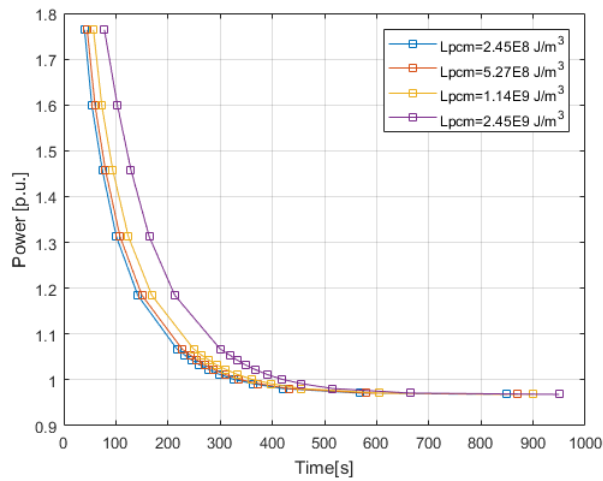
Figure 7.4: Peak Power vs. Transient Capable Time within Class H Temperature Limit (using paraffin properties as a reference: K_{pcm}=0.25 W/mK L_{pcm}=2.45E8 J/m^3) (a) PCM Thermal Conductivity (b) PCM Latent Energy

7.2.3 Results and Discussion

The preliminary simulation results of varying phase change material thermal conductivity and heat capacity are presented in Figures 7.3a and 7.3b. Note that the sensitivity study uses the paraffin thermal-physical properties as the starting baseline point and investigates a range 10 times that of the paraffin thermal-physical values. The motivation of this study is to learn the preliminary benefits and potential possibilities as we improve phase change

material properties. Figures 7.3a and 7.4a indicate that increasing PCM thermal conductivity can lower the hotspot temperature overall. Thus, the allowable peak-torque-operation curve mainly shifts upwards as higher electric loading is enabled with the lower steady-state hotspot temperature. Essentially, higher PCM material thermal conductivity assists the heat dissipation of windings toward the heat sink according to Figure 7.2b. The lower steady-state hotspot temperature is only helpful for the lower-peak-power designs. Figure 7.3b shows that the thermal response time can be extended by increasing the PCM latent energy. This explains why the allowable peak-torque-operation curve shifts horizontally to the right side with the higher latent energy. Higher latent energy means higher heat capacity of the PCM or more motor 'thermal inertia'. The overall motor peak-power-operation performance can be improved by increasing PCM thermal conductivity and latent energy density.

However, direct PCM integration is not a good option to maximize the transient performance of the proposed motor. The main drawback is that the PCM volume has to occupy the precious winding volume. The latent energy of paraffin wax is insufficient to extend motor peak power capability as current density has to increase to reach the same electric-loading level, which causes quadratic increase in copper loss.

7.3 Heat Pipe Insertion between the Winding and PCM Region

7.3.1 Concept Overview

Instead of shortening the physical distance between winding and PCM, the heat pipe can be used to minimize the thermal resistance and assist with conducting motor heat loss out. For applications that can accommodate the thermal time constant of heat pipes, integrate heat pipes with windings and channel heat to phase change material that is away from the active region, e.g., in the ends, radially inwards, etc. Select the optimal heat-pipe design for the temperature range of interest—i.e., just below max allowable temperature—to minimize δT and time lag during overload. This method can decouple the phase change material volume constraint from the space for the winding and the effective electrical loading of the machine.
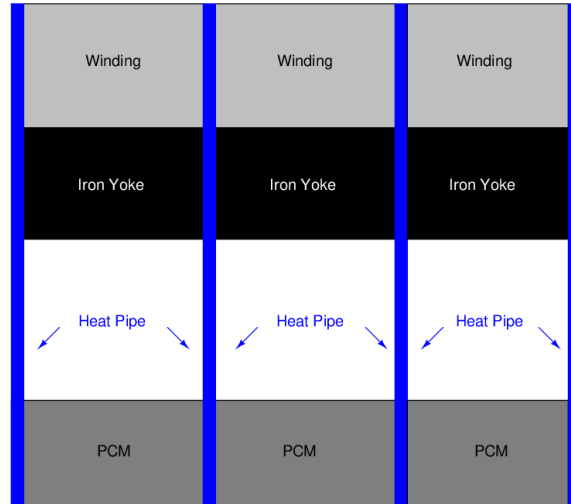
(a)
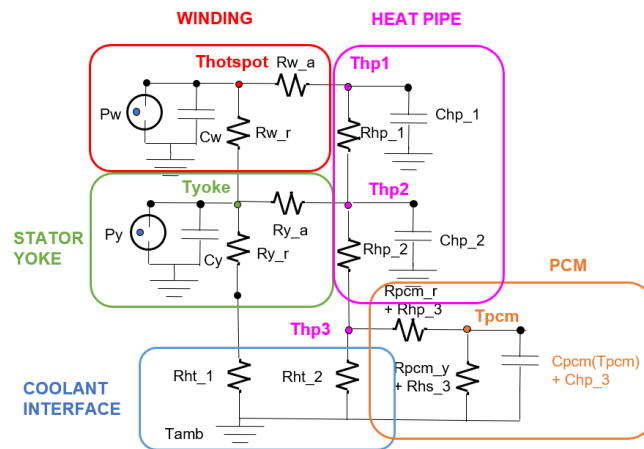
(b)

Figure 7.5: Heat Pipe Integration Method (a) Geometry Illustration (b) Thermal Equivalent Circuit Model

More space can be created to contain the PCM in the heat sink region or some other space away from the active region.

Additionally, with this arrangement, the package containing the PCM does not experience the high magnetic fields prevalent near the windings. High conductivity metals can be employed, and more substantial features can be incorporated. For example, the heat pipe could be designed with ends with a significantly higher surface area that is embedded within the PCM, thereby reducing the delta-T and improving the frequency response of the thermal system. The other end of the heat pipes that attach to the windings can also incorporate

features to increase surface area and reduce the contact resistance, without incurring large eddy losses and degrading the dielectric integrity of the windings. Ceramic materials can be utilized; however, there could be some manufacturing and mechanical challenges with a more complex structure shown below. A metal structure can minimize these challenges, but needs to have features to minimize heating from induced currents and risk of dielectric breakdown. A compromise may be metal heat spreaders that are striated, to impede eddy current loops, and covered with a thin ceramic coating for good electrical insulation without substantially increasing the thermal resistance.

7.3.2   Modeling Method

Similar modeling processes are developed in the second PCM integration method. First, a thermal equivalent circuit of the heat pipe and PCM integration method is proposed in Figure 7.5b. It is a 6-node lumped thermal equivalent circuit, including winding, yoke, heat pipe, and PCM temperatures. The temperature vector is given as:

$$T = \begin{bmatrix} T_{hotspot} & T_{yoke} & T_{hp\_1} & T_{hp\_2} & T_{hp\_3} & T_{PCM} \end{bmatrix}^T \tag{7.6}$$

Also, winding and iron losses should be included in heat load vector Q:

$$Q = \begin{bmatrix} P_w & P_y + \frac{T_{amb}}{R_{ht1}+R_{y\_r}} & 0 & 0 & \frac{T_{amb}}{R_{ht2}} & \frac{T_{amb}}{R_{ht3}+R_{pcm\_r}} \end{bmatrix}^T \tag{7.7}$$

The overall admittance matrix can be established based on the thermal resistor connections in Figure 7.5b as follows:

$$
G = \begin{bmatrix}
\frac{1}{R_{w\_r}} + \frac{1}{R_{w\_a}} & -\frac{1}{R_{w\_r}} & -\frac{1}{R_{w\_a}} & 0 & 0 & 0 \\[6pt]
-\frac{1}{R_{w\_r}} & \frac{1}{R_{w\_r}} + \frac{1}{R_{y\_a}} + \frac{1}{R_{y\_r}+R_{ht\_1}} & 0 & -\frac{1}{R_{y\_a}} & 0 & 0 \\[6pt]
-\frac{1}{R_{w\_a}} & 0 & \frac{1}{R_{y\_a}} + \frac{1}{R_{hp\_1}} & -\frac{1}{R_{hp\_1}} & 0 & 0 \\[6pt]
0 & -\frac{1}{R_{y\_a}} & -\frac{1}{R_{hp\_1}} & \frac{1}{R_{y\_a}} + \frac{1}{R_{hp\_1}} + \frac{1}{R_{hp\_2}} & -\frac{1}{R_{hp\_2}} & 0 \\[6pt]
0 & 0 & 0 & -\frac{1}{R_{hp\_2}} & \frac{1}{R_{hp\_2}} + \frac{1}{R_{ht\_2}} + \frac{1}{R_{hp\_3}+R_{pcm\_a}} & -\frac{1}{R_{hp\_3}+R_{pcm\_a}} \\[6pt]
0 & 0 & 0 & 0 & -\frac{1}{R_{hp\_3}+R_{pcm\_a}} & \frac{1}{R_{hp\_3}+R_{pcm\_a}} + \frac{1}{R_{ht\_3}+R_{pcm\_r}}
\end{bmatrix}
\tag{7.8}
$$

The corresponding capacitance matrix in Figure 7.5b is:

$$
C = diag \begin{pmatrix} C_w & C_y & C_{hp\_1} & C_{hp\_2} & C_{hp\_3} & C_{pcm} \end{pmatrix}
\tag{7.9}
$$

With the given heat load vector, and admittance and capacitance matrix, the temperature vector T can then be evaluated using the transient thermal governing Equation (7.5).

For more accurate motor performance prediction, the 2-D FLUX FEA model is also developed for the following sensitivity study. The overload transient performance will be evaluated by varying PCM thermal conductivity, volume and material types.

7.3.3 Results and Discussion

A similar PCM properties sensitivity study is analyzed here. Figure 7.6a indicates there is no time response extension improvement while increasing the PCM thermal conductivity. Because the PCM does not contribute significantly to winding heat dissipation, the heat pipes and stator yoke create the two main heat dissipation paths to conduct the winding
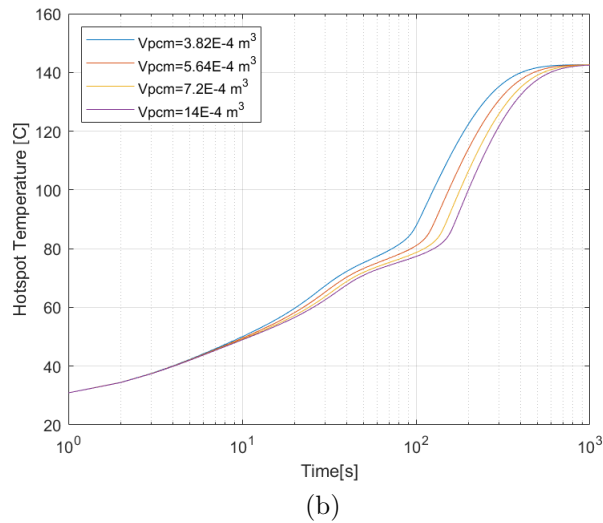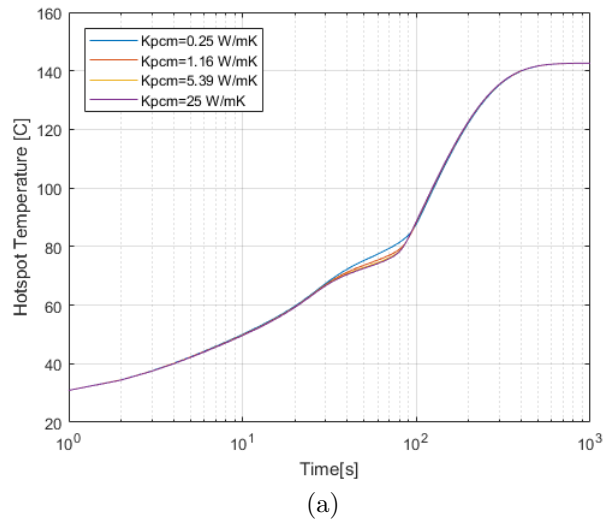
Figure 7.6: Temperature vs. Time with Motor Power Rating at 1 p.u. within Class H (a) PCM Thermal Conductivity (b) PCM Volume

heat to the ambient air. Another thing to note is that a heat pipe creates a direct cooling path for windings. The heat sink is eliminated and replaced with heat pipes. The heat pipes conduct winding heat directly toward the the cooling air and PCM package. Thus, they reduce the motor steady state temperature compared with the initial motor baseline design (without heat pipe or PCM package). Figure 7.6b shows that more PCM heat capacity can delay the motor hotspot temperature rise. Both increasing PCM volume and latent energy property can effectively improve the motor peak-power-operation time. Thus, the
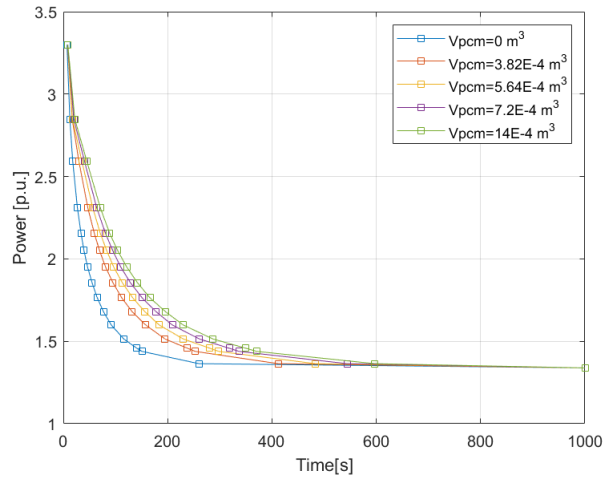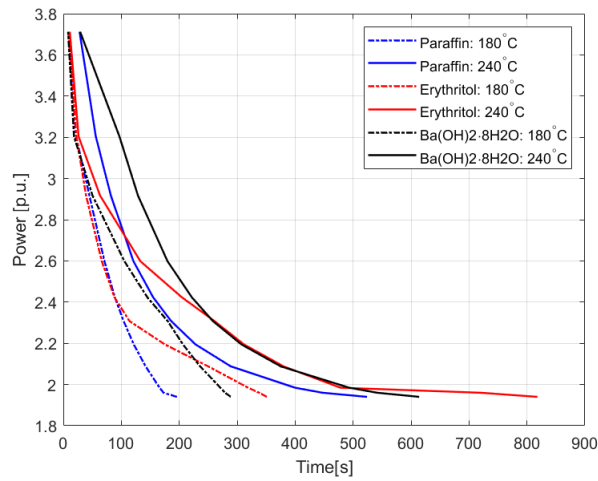
Figure 7.7: Peak Power vs. Transient Capable Time (a) Paraffin - Varying PCM Volume (Vpcm) within Class H (b) Varying PCM Material Types, including Paraffin Wax, Erythritol, and Ba(OH)2·8H2O with Class H and S

peak-power-operation curve is shifted toward the right side of Figure 7.7a.

Figure 7.7b presents the motor overload transient performance using paraffin wax, erythritol, and Ba(OH)2·8H2O under Class H (up to 180 °C) and Class S (up to 240 °C). According to the property summary of various PCM materials in Table 7.1, Ba(OH)2·8H2O has the highest latent energy density value, which is approximately 3 times that of paraffin wax and 1.5 times that of erythritol. So Ba(OH)2·8H2O achieves the best overload transient performance, as shown in Figure 7.7b, both Class H and S cases. At the lower peak-power

range of 1.8–2.4 p.u., erythritol can extend the allowable time curve slightly beyond that of Ba(OH)2·8H2O because erythritol has higher heat capacity and melting point. Improving motor insulation temperature limit from Class H to S enables the peak-power allowable time to grow by around 50% to 100%.

Table 7.2: Summary of Motor Weight and Peak Power Comparisons (including with or without PCM materials)

Peak Power	p.u.	1.89	1.94	1.98	2.09
Weight (peak power)	kg	145.34	149.19	152.26	160.72
Weight (nominal power) - Paraffin	kg	78.10	78.10	78.10	78.10
Class-H Time	sec	230	196	166	142
Class-S Time	sec	1200	524	400	289
Weight (nominal power) - Erythritol	kg	78.67	78.67	78.67	78.67
Class-H Time	sec	383	351	319	250
Class-S Time	sec	1700	818	478	380
Weight (nominal power) - Ba(OH)2·8H2O	kg	79.90	79.90	79.90	79.90
Class-H Time	sec	311	289	271	236
Class-S Time	sec	1350	614	493	375

Suppose the takeoff power is twice of the cruising power in the hybrid-electric propulsion system of Figure 7.1. Table 7.2 summarizes the motor weight sized at the peak power at takeoff condition and the nominal power at cruising condition with paraffin wax, erythritol, and Ba(OH)2·8H2O PCM materials at both Class H and S. Take peak-power at 1.98 p.u. as an example. The motor weight applied with the heat-pipe PCM integration method can be reduced by roughly 80–90% compared with the baseline motor design in [1]. The PCM weight is only 1-3% of the motor total weight, since the PCM density is only 33%–50% that of aluminum. Increasing PCM package volume further does not increase machine weight much. Using Class H and S insulation can allow up to 6 and 14 minutes, respectively. If the takeoff period has to last 20 minutes, motor volume can be enlarged by another 5-10%, e.g. at 1.89 peak power, according to Table 7.2.

CHAPTER 8

CONCLUSIONS AND FUTURE WORK

8.1 Conclusions

In this dissertation, advances are made in the electro-thermal modeling of high-specific-power, high-frequency, slotless machines, and component-level validation to reduce design uncertainties and to calibrate the proposed model.

In Chapter 1, a MW high-specific-power motor has been presented for aircraft electrification. The high specific power was achieved by novel lightweight motor topology and higher copper current density than state-of-the-art machines while maintaining high magnetic loading and tip speed. Although the high frequency and tip speed lead to large amounts of eddy-current and windage losses, the copper current density of the proposed motor is 50% more than that of conventional low-frequency air-cooled machines.

In Chapter 2, a high-fidelity and computationally efficient electro-thermal model has been developed to investigate the interactions among motor design variables. The true multiphysics module is implemented by the directly coupling EM model to predict electrical performance and losses, and thermal model to predict temperature distribution while having a quick mechanical constraint evaluation. This analytical motor design module can be fed into a genetic optimization algorithm for the hybrid-electric engine system integration in Chapter 6.

In Chapter 3, thermal management design and validation are carried out to establish confidence in the proposed losses and thermal analytical models. The fan performance and windage loss were validated in a flow test in which a dummy rotor spun at up to 10,000 rpm, which is around 66% of the rated speed. And full-size stator thermal tests were conducted to verify both analytical and simulation prediction results.

In Chapter 4, the litz wire heat dissipation capability including transposition effects was studied in detail, because improving litz wire effective thermal conductivity is important for enabling high copper current density in high-frequency motors. An analytical model of predicting litz wire thermal conductivity including transverse heat dissipation path within transposition arrangement is developed. This model shows good agreement with both simulations and experiments.

In Chapter 5, to accommodate the critical requirements of litz wire design for high-specific-power motors, a refined electro-thermal analytical model and optimization scheme has been established. Both induced-current loss and hotspot temperature models for slotless litz-wire windings are presented and discussed. The wire design parameters, such as bundle transposition angle, turn number and strand size, are optimized.

In Chapter 6, the developed motor design optimization toolbox in Chapter 3 was applied to various electric propulsion studies. One study is for thermal management integration with the hybrid-electric engine system developed by Rolls Royce.

In Chapter 7, another use case of the developed multi-physics model, including motor transient performance-motor peak-power-operation with PCM integration, is presented for Raytheon Technologies hybrid-electric engine system. Two novel PCM integration methods are proposed and discussed. The related sensitivities of PCM thermal-physical properties indicate effective ways to improve motor transient capabilities, using MW motor as an example tailored to hybrid-electric aircraft mission profile.

8.2 Future Work

Although the proposed motor topology and developed electro-thermal design modules can increase motor specific power by a factor of 2-4 times that of the conventional motor, there are several improvements that can be made to further advance motor specific power for aircraft electrification.

One improvement is to adopt new thermal management techniques to allow higher copper current density. Exploring ways to minimize the thermal resistance between winding and heat sink region can effectively lower motor hotspot temperature. Also, fan design can be

optimized further to allow more mass flow rate with minimum pumping cost. Overall, the thermal management design of the proposed motor should be improved to advance motor specific power further.

The other improvement is to design the motor based on the mission profile accounting for transient capability, instead of at the peak power only considering steady-state performance. This approach can avoid oversizing the motor at the peak-power operation and reduce motor weight further. The initial ideas and first-iteration analysis of using PCM to boost motor transient capabilities are presented in Chapter 7. More rigorous studies are needed to investigate the PCM integration methods and extend the work to motor design optimization customized to industrial hybrid-electric engine systems.

REFERENCES

[1] A. Yoon, X. Yi, J. Martin, Y. Chen, and K. Haran, "A high-speed, high-frequency, air-core PM machine for aircraft application," in *Power and Energy Conference at Illinois (PECI)*, 2016.

[2] W. Tong, *Mechanical Design of Electric Motors*. CRC Press, 2016.

[3] J. Gieras, *Advancements in Electric Machines*. Springer, 2008.

[4] A. Borisavljevic, *Limits, Modeling, and Design of High-Speed Permanent Magnets*. Springer, 2012.

[5] X. Yi, A. Yoon, and K. S. Haran, "Multi-physics optimization for high-frequency air-core permanent-magnet motor of aircraft application," in *2017 IEEE International Electric Machines and Drives Conference (IEMDC)*. IEEE, 2017, pp. 1–8.

[6] X. Yi, A. Yoon, C. Lentz, and K. Haran, "Multi-physics optimization for high-frequency air-core permanent-magnet motor of aircraft application," *IEEE Transactions on Transportation Electrification*, (under review).

[7] X. Yi, A. Yoon, A. D. Anderson, T. Balachandran, S. Srimmana, and K. Haran, "Analysis and validation of stator thermal performance and losses for a high-speed high-specific-power motor," *IEEE Transactions on Energy Conversions*, (under review).

[8] X. Yi, R. Sanchez, K. Haran, J. Veres, A. Perry, and P. J. Ansell, "Self-pumped air-cooling design for a high-speed high-specific-power motor," in *IEEE Transportation Electrification Conference and Expo*, 2018.

[9] N. J. Renner, J. D. Lenz, X. Yi, and K. S. Haran, "Development of form-wound air-core armature windings for high-frequency electric machines," in *2017 IEEE International Electric Machines and Drives Conference (IEMDC)*. IEEE, 2017, pp. 1–8.

[10] J. Lentz, N. Renner, X. Yi, and K. Haran, "Insulation considerations in form-wound armature windings for high-frequency electric machines," in *IEEE Power & Energy Society General Meeting (PESGM)*, 2018.

[11] X. Yi, X. Qiao, T. Yang, K. Haran, and N. Miljkovic, "Equivalent thermal conductivity prediction of form-wound windings with litz wire considering transposition effect," in *IEEE International Electric Machines and Drives Conference (IEMDC)*, 2019.

[12] X. Yi, T. Yang, J. Xiao, N. Miljkovic, W. King, and K. Haran, "Equivalent thermal conductivity prediction of form-wound windings with litz wire including transposition effects," *IEEE Transactions on Industry Applications*, (under review).

[13] X. Yi and K. Haran, "Electro-thermal analysis and optimization design of slotless litz-wire windings for high-frequency high-specific-power motors," *IET Electric Power Applications*, (under review).

[14] Y. Wang, X. Yi, X. Zhang, Y. Yin, H. Tao, and K. Haran, "Partial-discharge-free insulation design of air-core permanent magnet synchronous machine for aircraft ropulsion," *IEEE Transactions on Transportation Electrification*, pp. 1–10, 2020.

[15] X. Yi and K. Haran, "Thermal integration of a high-frequency high-specific-power motor within electrically variable engine," in *AIAA/IEEE Electric Aircraft Technologies Symposium(EATS)*, 2019.

[16] X. Yi and K. Haran, "Transient performance study of high-specific-power motor integrated with phase change material for transportation electrification," in *IEEE Transportation Electrification Conference and Expo*, 2020, pp. 1–8.

[17] P. H. Mellor and R. Wrobel, "Optimization of a multipolar permanent-magnet rotor comprising two arc segments per pole," *IEEE Transactions on Industry Applications*, vol. 43, no. 4, pp. 942–951, 2007.

[18] M. Markovic and Y. Perriard, "Optimization dsign of a segmented halbach permanent-magnet motor using an analytical model," *IEEE Transactions on Magnetics*, vol. 45, no. 7, pp. 2955–2960, 2009.

[19] Z. Zhu, W. Chu, and Y. Shen, "Analytical optimisation of external rotor permanent magnet machines," *IET Electrical Systems in Transportation*, vol. 3, no. 2, pp. 41–49, 2013.

[20] G. Y. Sizov, P. Zhang, D. M. Ionel, N. A. O. Demerdash, and M. Rosu, "Automated multi-objective design optimization of PM AC machines using computationally efficient FEA and differential evolution," *IEEE Transactions on Industry Applications*, vol. 49, no. 5, pp. 2086–2096, 2013.

[21] S. T. Vun and M. D. McCulloch, "Optimal design method for large-scale YASA machines," *IEEE Transactions on Energy Conversion*, vol. 30, no. 3, pp. 900–907, 2015.

[22] D. Lee, A. Jin, B.-H. Min, L. Zheng, and K. Haran, "Optimisation method to maximise torque density of high-speed slotless permanent magnet synchronous machine in aerospace applications," *IET Electric Power Applications*, vol. 12, no. 8, pp. 1075–1081, 2018.

[23] W. Jiang and T. M. Jahns, "Coupled electromagnetic–thermal analysis of electric machines including transient operation based on finite-element Techniques," *IEEE Transactions on Industry Applications*, vol. 51, no. 2, pp. 1880–1889, 2015.

[24] Lei, C. Barth, S. Qin, W. Liu, I. Moon, A. Stillwell, D. Chou, T. Foulkes, Z. Ye, Z. Liao, and R. C. N. Pilawa-Podgurski, "A 2 kW, single-phase, 7-level flying capacitor multilevel inverter with an active energy buffer," *IEEE Transactions on Power Electronics*, vol. 32(11), pp. 8570–8581, 2017.

[25] Z. Xia, Z. Zhu, and D. Howe, "Analytical magnetic field analysis of halbach magnetized permanent magnet machine," *IEEE Transactions on Magnetics*, vol. 40, no. 4, pp. 1864–1872, 2004.

[26] Y. Yamada, "Resistance of a flow through an annulus with an inner rotating cylinder," *JSME*, vol. 5, no. 18, pp. 302–310, 1961.

[27] B. Petukhov, "Heat transfer and friction in turbulent pipe flow with variable physical properties," *Advances in Heat Transfer*, vol. 6, pp. 503–564, 1970.

[28] V. Gnielinski, "New equations for heat and mass transfer in turbulent pipe and channel flow," *Int. Chemical Engineering*, vol. 16, pp. 359–368, 1976.

[29] Y. Chen, R. Sanchez, A. Yoon, and K. S. Haran, "Mechanical design considerations of an "ironless," high-specific-power electric machine," *IEEE Transactions on Transportation Electrification*, vol. 3, no. 4, pp. 855–863, 2017.

[30] A. El-Refaie and M. Osama, "High specific power electrical machines: A system perspective," in *2017 20th International Conference on Electrical Machines and Systems (ICEMS)*, 2017, pp. 1–6.

[31] C. Cristian and M. Osama, "High specific power electrical machines: A system perspective," in *Electric and Hybrid Aerospace Technologies Symposium*, 2015, pp. 1–6.

[32] E. Bilgen and R. Boulos, "Functional dependence of torque coefficient of coaxial cylinders on gap width and reynolds numbers," *Journal of Fluids Engineering*, vol. 95, no. 1, p. 122, 1973.

[33] P. R. N. Childs, *Rotating Flow*. Elsevier, 2011.

[34] E. T. E. Graf and S. Kolesar, "Segregation of windage and core losses for high speed/frequency, permanent magnet machines," *Electric Machines Technology Symposium (EMTS)*, 2008.

[35] J. Vrancik, "Prediction of windage power loss in alternators," *NASA Technical Note*, 1968.

[36] J. P. Veres, "Axial and centrifugal compressor mean line flow analysis method," *47th AIAA Aerospace Sciences Meeting including The New Horizons Forum and Aerospace Exposition*, 2009.

[37] D. Dropkin and A. Carmi, "Natural convection heat transfer from a horizontal cylinder rotating in air," *Trans. ASME*, vol. 79, pp. 741–749, 1957.

[38] K. M. Becker, "Measurement of convective heat transfer from a horizontal cylinder in a tank of water," *Int. J. Heat Mass Trans*, vol. 6, pp. 1053–1062, 1963.

[39] G. Etemad, "Free convection heat transfer from a rotating cylinder in ambient air with interferometric study of flow," *Trans. ASME*, vol. 77, pp. 1283 –1289, 1955.

[40] F. Tachibana and S. Fukui, "Convective heat transfer of the rotational and axial flow between two concentric cylinders," *JSME*, vol. 7, no. 26, pp. 385–391, 1964.

[41] Y. Yamada, "Resistance of a flow through an annulus with an inner rotating cylinder," *Bulletin of JSME*, vol. 5, no. 18, pp. 302–310, 1962.

[42] K. Becker and J. Kaye, "Measurements of diabetic flow in an annulus with an inner rotating cylinder," *Int. J. Heat Mass Trans*, vol. 84, pp. 97–105, 1962.

[43] E. Cobb and O. Saunders, "Heat transfer from a rotating disc," *Proc. Soc. London*, vol. 236, pp. 343–351, 1956.

[44] D. Edwards, V. Denny, and A. F. Mills, *Transfer Processes*. 2nd ed. Hemisphere, 1979.

[45] J. Saari, "Thermal analysis of high-speed induction machines," *Acta Polytechnica Scandinavica Electrical Engineering Series*, vol. 90, 1998.

[46] X. Zhang, C. L. Bowman, T. C. O'Connell, and K. S. Haran, "Large electric machines for aircraft electric propulsion," *IET Electric Power Applications*, vol. 12, no. 6, pp. 767–779, 2018.

[47] A. A. Woodworth, R. Jansen, K. Duffy, P. Naghipour, and E. Shin, "Creating a multifunctional composite stator slot material system to enable high power density electric machines for electrified aircraft applications," in *2018 AIAA/IEEE Electric Aircraft Technologies Symposium (EATS)*, 2018, pp. 1–8.

[48] J. Martin, A. Yoon, A. Jin, and K. S. Haran, "High-frequency litz "air-gap" windings for high-power density electrical machines," *Electric Power Components and Systems*, vol. 45, no. 7, pp. 798–805, 2017.

[49] C. R. Sullivan and R. Y. Zhang, "Simplified design method for litz wire," in *2014 IEEE Applied Power Electronics Conference and Exposition - APEC 2014*. IEEE, 2014, pp. 2667–2674.

[50] H. Liu and J. Hahne, "High-speed compulsator stator thermal management," *IEEE Transactions on Magnetics*, vol. 39, no. 1, pp. 357–361, 2003.

[51] X. Huang, Q. Tan, L. Li, J. Li, and Z. Qian, "Winding temperature field model considering void ratio and temperature rise of a permanent magnet synchronous motor with high current density," *IEEE Transactions on Industrial Electronics*, 2016.

[52] A. Boglietti, M. Cossale, S. Vaschetto, and T. Dutra, "Thermal conductivity evaluation of fractional-slot concentrated-winding machines," *IEEE Transactions on Industry Applications*, vol. 53, no. 3, pp. 2059–2065, 2017.

[53] R. Wrobel, S. Ayat, and J. L. Baker, "Analytical methods for estimating equivalent thermal conductivity in impregnated electrical windings formed using litz wire," *2017 IEEE International Electric Machines and Drives Conference, IEMDC 2017*, 2017.

[54] N. Simpson, R. Wrobel, and P. H. Mellor, "Estimation of equivalent thermal parameters of impregnated electrical windings," *IEEE Transactions on Industry Applications*, vol. 49, no. 6, pp. 2505–2515, 2013.

[55] "Thermal homogenization of electrical machine windings applying the multiple-scales method," *Journal of Heat Transfer*, vol. 139, no. 1, p. 012101, 2016.

[56] M. Jaritz, A. Hillers, and J. Biela, "General analytical model for the thermal resistance of windings made of solid or litz wire," *IEEE Transactions on Power Electronics*, 2018.

[57] *Thermal Properties of Plastic Materials.* Professional Plastics online datasheet.

[58] T. Yang, B. Kwon, P. B. Weisensee, J. G. Kang, X. Li, P. Braun, N. Miljkovic, and W. P. King, "Millimeter-scale liquid metal droplet thermal switch," *Applied Physics Letters*, vol. 112, no. 6, 2018.

[59] W. Zhao, X. Wang, S. Wu, S. Cui, X. Gerada, and H. Yan, "Eddy current losses anaysis and optimization design of litz-wire windings for air-core compulsators," *IEEE Transactions on Plasma Science*, vol. 47, no. 5, pp. 2532–2538, 2019.

[60] F. Tourkhani and P. Viarouge, "Accurate analytical model of winding losses in round litz wire windings," *IEEE Transactions on Magnetics*, vol. 37, no. 1, pp. 538–543, 2001.

[61] C. R. Sullivan, "Optimal choice for number of strands in a litz-wire transformer winding," *IEEE Transactions on Power Electronics*, vol. 14, no. 2, pp. 538–543, 1999.

[62] X. Tang and C. Sullivan, "Stranded wire with uninsulated strands as a low-cost alternative to litz wire," in *Power Electronics Specialists Conference*, 2004, pp. 854–860.

[63] M. Popescu and D. Dorrell, "Proximity losses in the windings of high speed brushless permanent magnet AC motors with single tooth windings and parallel path," *IEEE Transactions on Magnetics*, vol. 49, no. 7, pp. 3913–3916, 2013.

[64] H. Hamalainen, J. Pyrhonen, J. Nerg, and J. Taivitie, "AC resistance factor of litz-wire windings used in low-voltage high-power generators," *IEEE Transactions on Industrial Electronics*, vol. 61, no. 2, pp. 693–700, 2014.

[65] X. Yi, J. Xiao, T. Yang, N. Miljkov, and K. S. Haran, "Equivalent thermal conductivity prediction of form-wound windings with litz wire considering transposition effect," in *2019 IEEE International Electric Machines and Drives Conference (IEMDC)*, 2019, pp. 2048–2055.

[66] Xu Tang and C. Sullivan, "Stranded wire with uninsulated strands as a low-cost alternative to litz wire," in *IEEE 34th Annual Conference on Power Electronics Specialist, 2003. PESC '03.*, vol. 1. IEEE, pp. 289–295.

[67] S. Sudhoff, *Power Magnetic Devices: A Multi-Objective Design Approach.* Hoboken, New Jersey: Wiley, 2014.

[68] C. Perullo, D. Trawick, M. Armstrong, and J. Tai, "Cycle selection and sizing of a single-aisle transport with the electrically variable engine (EVE) for fleet level fuel optimization," in *55th AIAA Aerospace Sciences Meeting*, 2017.

[69] National Academies of Sciences, Engineering, and Medicine, *Commercial Aircraft Propulsion and Energy Systems Research: Reducing Global Carbon Emissions.* National Academies Press, 2016.

[70] J. Rheaume and C. E. Lents, "Design and simulation of a commercial hybrid electric aircraft thermal management system," in *55th AIAA Aerospace Sciences Meeting*, 2018.

[71] D. Trawick, C. Perullo, M. Armstrong, D. Snyder, J. C. Tai, and D. N. Mavris, "Development and application of gt-heat for the electrically variable engine (EVE) design," in *55th AIAA Aerospace Sciences Meeting*, 2017.

[72] M. Popescu, D. Staton, A. Boglietti, A. Cavagnino, D. Hawkins, and J. Goss, "Modern heat extraction systems for power traction machines – a review," *IEEE Transactions on Industry Applications*, vol. 52, p. 2167–2175, 2016.

[73] Y. Yang, D. Staton, B. Bilgin, M. Kasprzak, S. Nalakath, H. Sadek, M. Preindl, J. Cotton, N. Schofield, and A. Emadi, "Thermal management of electric machines," *IET Electrical Systems in Transportation*, vol. 7, no. 2, pp. 104–116, 2017.

[74] M. Tosetti, P. Maggiore, A. Cavagnino, and S. Vashetto, "Conjugate heat transfer analysis of integrated brushless generators for more electric engines," *IEEE Transactions on Industry Applications*, vol. 50, no. 4, pp. 2467– 2475, 2014.

[75] A. Tuysuz, F. Meyer, M. Steichen, C. Zwyssig, and J. W. Kolar, "Advanced cooling methods for high-speed electrical machines," *IEEE Transactions on Industry Applications*, vol. 53(3), p. 2077–2087, 2017.

[76] T. Davin, P. Jullien, H. Souad, and Y. Robert, "Experimental study of oil cooling systems for electric motors," *Applied Thermal Engineering*, vol. 75, pp. 1–13, 2015.

[77] S. Ayat, C. Serghine, T. Klonowsk, S. Yon, A. Mutabazi, and S. McDaniel, "The use of phase change material for the cooling of electric machine windings formed with hollow conductors," in *IEEE International Electric Machines and Drives Conference (IEMDC)*, 2019.

[78] S. Krishnan, S. V. Garimell, and S. S. Kang, "A novel hybrid heat sink using phase change materials for transient thermal management of electronics," *IEEE Transactions on Components and Packaging Technologies*, vol. 28(2), pp. 281–289, 2015.

[79] T. Yang, J. Kang, P. Weisensee, P. Braun, N. Miljkovic, and W. P. King, "A novel hybrid heat sink using phase change materials for transient thermal management of electronics," *Applied Physics Letters*, (under review).

[80] P. Spierling and C. E. Lentz, "Parallel hybrid propulsion system for a regional turbo-prop: conceptual design and benefits analysis," in *AIAA Propulsion and Energy 2019 Forum*, 2019, pp. 1–7.

[81] V. T. Buyukdegirmenci and P. T. Krein, "Machine characterization for short-term or instantaneous torque capabilities: an approach based on transient thermal response," in *2013 International Electric Machines Drives Conference*, 2013, pp. 1–8.

[82] X. Yi and K. S. Haran, "Thermal integration of a high-frequency high-specific-power motor within electrically variable engine," in *AIAA Propulsion and Energy 2019 Forum*, 2019, pp. 1–8.

[83] A. S. Fleischer, "Thermal energy storage using phase change materials fundamentals and applications," in *Springer Briefs in Thermal Engineering and Applied Science*, 2015, pp. 1–8.

[84] N. R. Jankowski and F. P. McCluskey, "A review of phase change materials for vehicle component thermal buffering," *Applied Energy*, vol. 113, pp. 1525–1561, 2014.